TECHNISCHE UNIVERSITÄT MÜNCHEN
Lehrstuhl für Technische Chemie II

Promotion of cracking and dimerization of hydrocarbons on zeolite Brønsted acid sites by proximity to extra-framework aluminum

Yang Zhang

Vollständiger Abdruck der von der Fakultät für Chemie der Technischen Universität München zur Erlangung des akademischen Grades eines

Doktors der Naturwissenschaften (Dr. rer. nat.)

genehmigten Dissertation.

Vorsitzender: Prof. Dr.- Ing. Kai-Olaf Hinrichsen

Prüfer der Dissertation:

1. Prof. Dr. Johannes A. Lercher
2. Prof. Dr. Klaus Köhler

Die Dissertation wurde am 06.12.2018 bei der Technischen Universität München eingereicht und durch die Fakultät für Chemie am 13.12.2018 angenommen.

For my family

“Living without an aim is like sailing without a compass.”

John Ruskin (1819-1900)

Acknowledgements

This PhD dissertation is completed from October 2014 to November 2018 at the chair of Technical chemistry II of the Department of Chemistry at the Technical University of Munich (TUM). There are a great many people I want to express my deepest gratitude from the first day I begin to do my PhD study.

First and foremost, I would like to express my sincerest gratitude to my supervisor **Prof. Dr. Johannes A. Lercher** to give me the hard-won opportunity to work in this distinguished group. I appreciate you for your trust in me to study in the acid-base catalysis subject, one of your important research fields. I am really grateful for your patience, careful inspiration and endless guidance for my PhD study, especially in the first two years of the hardest time of my study. You teaches me not only the systematic training in scientific research, rigorous attitude of scholarship, but also unremitting exploration spirit, which is extreme valuable asset for my future academic research. I am also thanks for your financial support so that I can finish my thesis on time.

Secondly, I am hugely appreciative to my supervisor **Dr. Yue Liu.** Thanks for your guidance without reservation through my four years of doctoral study. You supervised me in each step of my study and corrected every research reports, even every punctuation and erratum. You shared me with your lab experience and provided me some constructive suggestions whenever my studies were stack with the problems. Without your elaborative guidance, I could not finish my thesis successfully. Except academic guidance, you also give me unselfish help in the life like a friend and elder brother. I will never forget all your help and wish you all the best for the future.

Then I would like to give great gratitude to my another supervisor, **Dr. Ricardo Bermejo de Val**. Thank you to help me to figure out the problems I met during my work and give me a great many productive discussions and instructions through my PhD study. Thanks for your standing encouragement, support and suggestion.

I also want to give countless gratitude to my supervisor, **Dr. Maricruz Sanchez-Sanchez**. Thanks for her to choose me to join in the zeolite group and give me so many valuable instructions, especially at the beginning of my study. I also give my thanks to my research partner Prof. Gary L. Haller (Yale University) and Ruixue Zhao to correct my first paper and give me many constructive suggestions, so that our research is more fluency and understandable. I also thank Jianzhi Hu (PNNL) and Meng Wang (PNNL) for their NMR measurements. I appreciate the supervisions from our group senior scientists: Prof. Dr. Andreas Jentys, Dr. Hui Shi, Dr. Eszter Baráth, Dr. Erika E. Ember and Dr. Oliver Y. They can always point out some uncontemplated findings during my reports in the Monday seminar. I also express my thanks for the scientific discussions with Prof. Enrique Iglesia (University of California at Berkeley), Prof. Joachim Sauer (Humboldt University) and Prof. Aditya Bhan (Minnesota University) and Prof. Cathy Chin (Toronto University), which broaden my research from various perspectives and provide some valuable suggestions. Thanks for the help of all of you, so that my research are always in the right direction and my PhD study become easier.

I also thank our technical staff. Franz-Xaver Hecht, very important people in our group, many thanks to you to maintenance my setup and solve the technical problems. I also thank Martin Neukamm for AAS measurement, Andreas Marx for my computer reparation and for the secretaries of Bettina Federmann, Ulrike Sanwald, Stefanie Seibold, Kateryna Kryvko for their support with all the tedious administrative matters.

I give my special gratitude to Dr. Yuanshuai Liu for the useful scientific instructions and discussions over the many years. I am particularly grateful to Manuel Wagenhofer for his selfless assistance in the operation of cracking setup and supervision of the experiments. I would like to thanks for the members in the zeolite group, Andreas Ehrmaier, Daniel Melzer, Takaaki Ikuno, Felix M. Kirchberger, Martin Baumgärtl, Verena Höpfl, Teresa Schachtl, Lingli Ni, Insu Lee, Martina Aigner, Laura Lobbert, Lei Tao, Dr. Larisha Yanira Cisneros Reves for the useful discussions and laboratory help over my whole PhD study. I am also very grateful for the help from Dr. Navneet

Kumar Gupta, Dr. Peter Hintermeier, Edith Berger, Dr. Sebastian Foraita and Dr. Moritz Schreiber, Christoph Denk, Dr. Sebastian Müller, Dr. Sebastian Grundner and Dr. Sebastian Eckestein.

My sincere thanks have to be given to my former and current colleagues in TCII: Dr. Jiayue He, Dr.Yuchun Zhi, Dr.Wenji Song, Dr. Bo Peng, Dr. Yang Song, Dr. Yu Lou, Dr. Marco Peroni, Dr. Guoju Yang, Dr. Lei Zhong, Dr. Wenhao Luo, Wanqiu Luo, Guanhua Chen, Xi Chen, Dr. Shujiao Jiang, Dr. Mingwu Tan, Dr. Qiang Liu and Fuli Deng, Dr. Udishnu Sanyal, Ferdinand Vogelgsang, Dr. Stanislav Kasakov, Martin Baumgärtl, Sylvia Albersberger, Matthias Steib, Dr. Rachit Khare, Manuel Weber-Stockbauer, Lara Milakovic, Niklas Pfriem, Dr. Kai Sanwald and other colleagues and friends whose name are not mentioned here for their friendship and support during I study in Munich. Many thanks for Pro. Dr. Gang Li, Pro. Dr. Anjie Wang and Pro. Dr. Xinwen Guo for their encouragements and supports during the past couple of years.

The last but not the least, I would like to thanks to my family for their endless love and to my relatives and friends for their support and help.

Many thanks to all of you, Yang Zhang

November, 2018

Abbreviations

PBUs	Primary building units
MR	Member ring
SBUs	Secondary building units
BAS	Brønsted acid site
SBAS	Strong Brønsted acid site
FAl	Framework aluminum
EFAl	Extra framework aluminum oxide
EFAl-SBAS	Strong Brønsted acid site with extra framework aluminum oxide in close proximity
I-SBAS	Isolated strong Brønsted acid site
LAS	Lewis acid site
DPE	Deprotonation energy
DFT	Density functional theory
TS	Transition state
TST	Transition state theory
IR	Infrared spectra
AHFS	Ammonia hexafluorosilicate
XRD	X-ray diffraction
NMR	Nuclear magnetic resonance
TPD	Temperature programmed desorption
K°	Standard state adsorption equilibrium constant

ΔH°_{ads}	Standard adsorption enthalpy
ΔS°_{ads}	Standard adsorption entropy
A	Pre-exponential factor
E_a	Activation energy
$\Delta H^{\ddagger}$	Activation enthalpy
$\Delta S^{\ddagger}$	Activation entropy
$\Delta G^{\ddagger}$	Gibbs free energy
XANES	X-ray absorption near-edge structure
EXAFS	Extended X-ray absorption fine structure
DQ	Double quantum
SQ	Single quantum
IMEC	Integrated molar extinction coefficient
R	Radius
m	Weight
eV	Electronvolt
MOR	Mordenite(Zeolite)
FAU	Faujasite(Zeolite)
TOF	Turnover frequency
TGA	Thermogravimetric analysis
DSC	Differential scanning calorimetry
TOS	Time on stream

κ	Transmission coefficient
$k^{\ddagger}$	Transition state rate constant
k_B	Boltzmann's constant

Abstract

Extra framework aluminum in proximity to Brønsted acid sites of H-MFI zeolite was created by controlled steaming. Such site pairs have a higher activity for protolytic cracking and dehydrogenation of pentane than single Brønsted acid sites via entropically stabilizing carbocationic transition states. The rate of ethene dimerization on such site pairs is also enhanced by promoting the rate of ethoxide formation.

Zusammenfassung

Extra-Gitter Aluminium in der Nähe der Brønsted-sauren Zentren von Zeolith H-MFI wurde durch kontrollierte Dampfbehandlung hergestellt. So hergestellte Paare von Zentren haben eine höhere Aktivität für das protolytische Cracken und die Dehydrierung von Pentan als einzelne Brønsted-saure-Zentren. Die höheren Raten werden durch die entropische Stabilisierung carbokationischer Übergangszustände erreicht. Auch die Rate der Dimerisierung von Ethen an solchen Zentren-Paaren wird durch eine erleichterte Ethoxidbildung erhöht.

Table of contents

Acknowledgements i

Abbreviations iv

Abstract vii

Table of contents viii

Chapter 1

1.Introduction 1

1.1. Basic introduction of Zeolite 2

1.2. ZSM-5. 2

1.3. Acid sites of zeolite. 4

1.3.1. Nature of acid sites 4

1.3.2. Acid strength 5

1.3.3. Acid density 6

1.4. Dealumination 6

1.4.1. Reaction pathways of dealumination 7

1.4.2. Dealumination mechanisms of zeolite 7

1.5. Heterogeneous catalytic reaction 9

1.5.1. The stages of heterogeneous catalysis 9

1.5.2. Physisorption and chemisorption 9

1.5.3. Langmuir adsorption model 10

1.5.4. Surface reactions 12

1.6. Effect of EFAl on the catalytic activity of BAS of zeolite 13

1.7. Motivation and scope of the thesis 14

1.8. Associated content 15

1.9. References 15

Chapter 2

2.Spatial proximity of extra-framework aluminum oxide to strong Brønsted acid sites21

2.1. Introduction 22

2.2. Experimental 23

2.2.1. Removal of EFAl 23

2.2.2. Steaming 23

2.2.3.Na^+ exchange 23

2.3. Catalyst characterization 24

2.3.1. IR spectroscopy of adsorption of pyridine 24

2.3.2. ^{27}Al MAS NMR 25

2.3.3. Nitrogen physisorption 26

2.3.4. Al K-Edge XANES and EXAF Measurements 26

2.3.5. X-ray diffraction patterns 27

2.4. Identification and quantification of I-SBAS and EFAl-SBAS in H-MFI-15 samples 27

2.5.Evidence that EFAl drcrease the BAS strength 37

2.6. Conclusions 38

2.7. Contributions 38

2.8. References 38

Chapter 3

3.Promotion of protolytic pentane conversion on H-MFI zeolite by proximity of extra-framework aluminum oxide and Brønsted acid sites 44

3.1. Introduction 45

3.2. Experimental 47

3.2.1. IR spectroscopy of adsorption of pentane 47

3.2.2. Adsorption heat of pentane 48

3.2.3. Kinetic measurements 48
3.3. Results 48
3.3.1. Adsorption properties of pentane on I-SBAS and EFAl-SBAS in H-MFI-15 48
3.3.2. Reaction of pentane on I-SBAS and EFAl-SBAS in H-MFI-15..... 53
3.3.3. Elementary steps for pentane cracking on zeolite 61
3.3.4. Impact of EFAl on the activity of SBAS in pentane cracking 66
3.4. Conclusions 67
3.5. Contributions 68
3.6. References 68

Chapter 4

4. Improvement of ethene dimerization on H-MFI zeolite by proximity of extra-framework aluminum oxide and Brønsted acid sites 83
4.1. Introduction 84
4.2. Experimental 87
4.2.1. IR spectroscopy of adsorbed ethene 87
4.2.2. Catalyst test 87
4.3. Results and discussions 88
4.3.1 Adsorption properties of ethene on BAS of H-MFI..... 88
4.3.2 Catalytic performance of ethene dimerization on I-SBAS and EFAl-SBAS of H-MFI 92
4.3.3. Elementary steps for ethene conversion in C_4H_8 pathway on H-MFI..... 95
4.3.4. Impact of EFAl on the deactivation of catalyst 97
4.4. Conclusions 99
4.5. Contributions 100
4.6. References 100

Chapter 5

5. Summary and conclusions 109

List of publications 112

Chapter 1

Introduction

1. General introduction

1.1 Basic introduction of zeolite

Zeolites are porous materials, which were first found in nature as result of volcanic activities [1, 2] and they have been widely used in the petrochemical and fine chemical industries as adsorbents [3], ion exchangers [4], molecular sieves [5] and catalysts [6-9]. The word of zeolite comes from two Greek words "zeo" = boil and "lithos" = stone with the meaning of boiling stones [10]. Zeolites are consisted of an aluminosilicate framework structure, composing of $[SiO_4]^{4-}$ and $[AlO_4]^{5-}$ tetrahedral arrangement through oxygen bridges, which are considered as primary building units (PBUs). In this tetrahedral structure, each oxygen in Si-O or Al-O bonds are shared by Si or Al cation and the Si or Al cation is surrounded by four oxygen atoms. The PBUs can form four, five, six, eight and twelve member rings (MR) by sharing the oxygen with other tetrahedra, which are called secondary building units (SBUs). The unique channels and cavities are formed by the link of the SBUs (Figure 1.1) [6, 11].

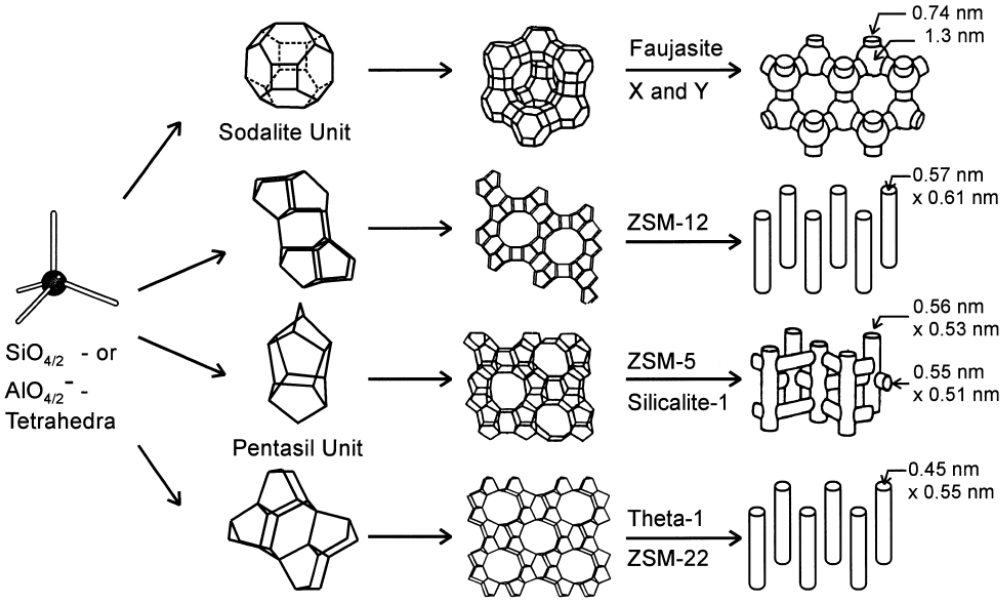

Figure 1.1. Evolution of zeolite structure from PBUs to channels and cavities (Take from reference [6, 11]).

Depending on the zeolite pore diameters, the zeolite pores can be classified into three types by IUPAC:

the pore diameter ≤ 2.0 nm (micropores);

2.0 nm < the pore diameter ≤ 50.0 nm (mesopores);

50.0 nm < the pore diameter (macropores).

The pore diameters in zeolite framework are typically less than 2.0 nm and they are considered as micropore materials.

1.2 ZSM-5

ZSM-5 is one of the aluminosilicate zeolite with MFI type framework and it is considered as one of the most popular heterogeneous catalysts and widely used in the petroleum industry, such as catalytic cracking, methane oxidation, alkene oligomerization and methanol conversion to hydrocarbons. ZSM-5 has a three dimensional framework containing 3-dimensional straight and sinusoidal 10 MR channel (Figure 1.2) [12]. The cavities of ZSM-5 are approximately 0.55 nm. ZSM-5 has 12 distinct Al T-sites and the location of these T sites determines the acid site strength in the zeolites, which thus affect the catalytic activity of the active sites in the ZSM-5. The Al, Si and O are homogenously distributed in the ZSM-5[13].

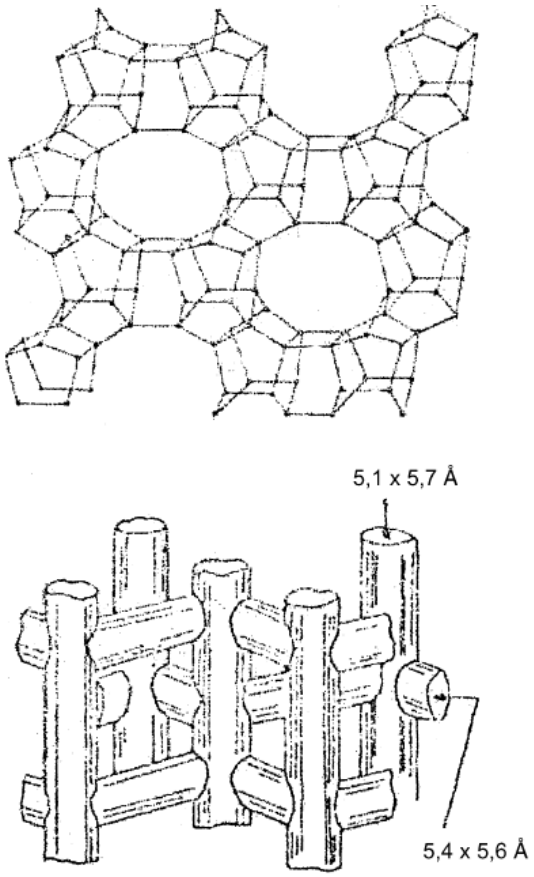

Figure 1.2. The framework structure and sinusoidal (zigzag) and straight channel of ZSM-5 (Take from reference [12]).

1.3 Acid sites of zeolite

1.3.1 Nature of acid sites

Brønsted acid site (BAS) is usually considered as the active center for many heterogeneous catalysis [14-16]. BAS is defined as proton donor. Si atom in neutral silicalite-1 is substituted by the trivalent Al atom, leading to the creation of proton at the bridging O atom (Si–OH–Al) and this proton works as BAS (Figure 1.3) [17]. Na form zeolite was ion exchanged with the ammonium salts, following by calcination of the ammonium form zeolite in synthetic air and the proton form zeolite was attained. The protons can also be substituted by various metal cations, such as Na^+, K^+ or Ca^{2+} via ion-exchange [17]. The zeolites with different metal cations can be used as oxidation and hydrogenation catalysts depending on the nature of the metal cations [18-22].

However, in some cases, the zeolites with less BAS density show higher catalytic activity than the samples with more BAS density. It is because that the former samples have higher amount of extra framework aluminum oxide (EFAl), which sometimes is considered as Lewis acid sites (LAS) [23]. So LAS is also very important for the zeolite catalytic activities. LAS is the specie to accept electron pair. One method to produce the LAS in the zeolite is the introduction of metal ions into zeolite [22]. Upon steaming treatment of the zeolite at high temperatures, the aluminum in the framework is extracted, leading to the formation of extra framework aluminum (hydr)oxide spieces (EFAl), such as AlO^+, $Al(OH)^+$, and $AlOH^{2+}$. During this process, the BAS is reduced and LAS is also formed (Figure 1.3) [24-26].

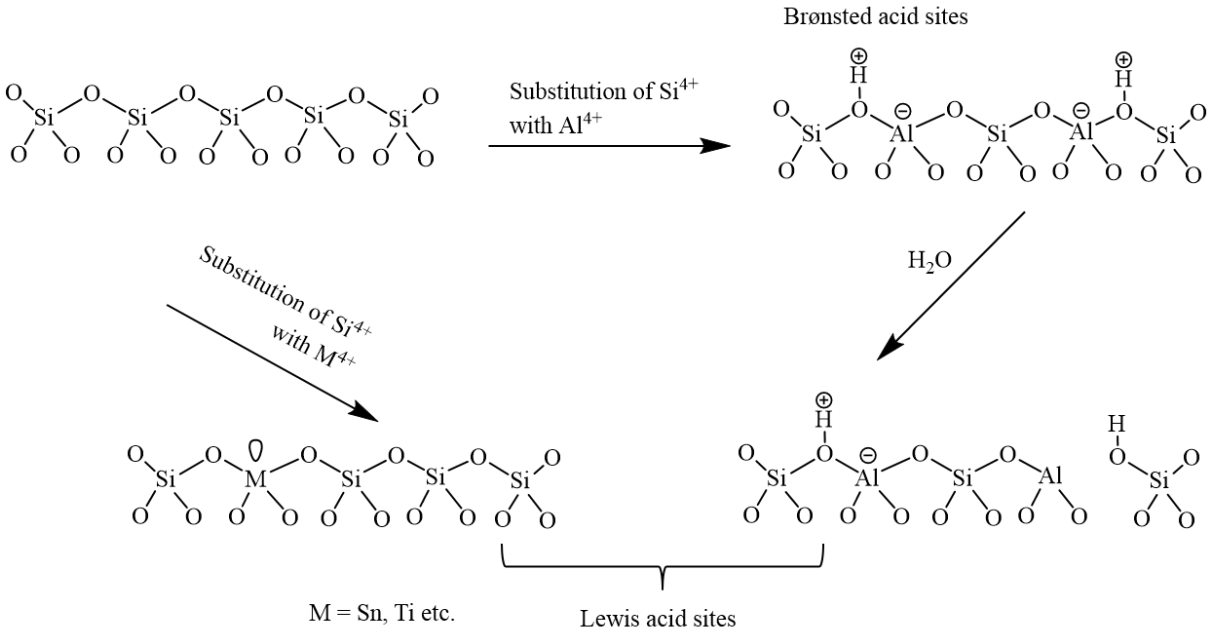

Figure 1.3. Formation process of Brønsted and Lewis acid sites within the zeolite framework.

1.3.2 Acid strength

Deprotonation energy (DPE) is the energy needed to separate a proton in the zeolite from conjugate anion to noninteracting distances, which can be used to describe the BAS strength quantitively [27].

The calculation of DPE can be employed by the following equation:

$$\mathrm{DPE} = E_{Z^-} + E_{H^+} - E_{ZH} \quad (1)$$

In which, E_{Z^-} is the energy of the zeolite anion after deprotonation, E_{H^+} is the energy of the gaseous proton and E_{ZH} is the energy of the neutral H form zeolite.

Density functional theory (DFT) can be used to estimate the DPE values. The proton may locate at different locations when its charge balances the oxygen anion that connected one Al atom in the zeolite. Therefore, the DPE under conditions that the equilibration of protons among four possible locations at each Al location (‹HZ›) is called ensemble-averaged DPE (‹DPE›) and the ‹DPE› is usually used to describe the BAS strength (Figure 1.4) [27].

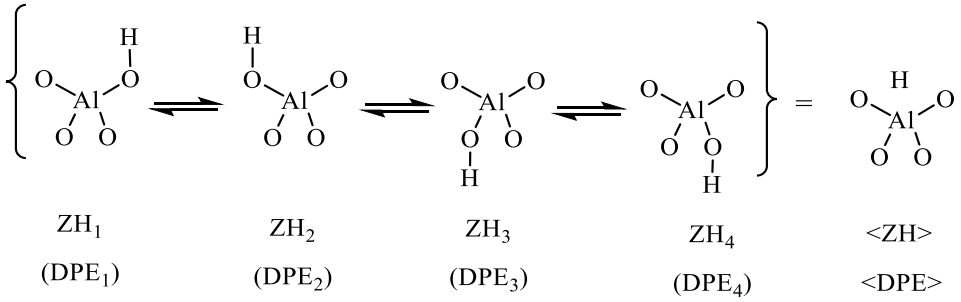

Figure 1.4. Deprotonation energies for the proton at different locations as well as the ensemble averaged structure energy.

1.3.3 Acid density

The density of BAS increases with the decrease of Si/Al ratio in the zeolite, as the ion exchange degree of silicon relies on the aluminum content in the zeolite. The acid density of BAS and LAS can be derived from the IR spectra of adsorption of pyridine or ammonia (Figure 1.5). In addition, the acid strength can also be evaluated by chemisorption and desorption of pyridine or ammonia at different temperatures [16].

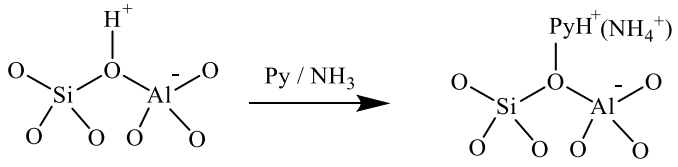

Figure 1.5. Interaction of pyridine with BAS.

1.4 Dealumination

Dealumination is one of the most common methods to modify zeolite to form more active and stable catalyst. Some studies evidenced that the EFAl can increase the rate of hydrocarbon transformations on BAS [23, 28]. Dealumination can also change the Si/Al ratio and generate mesopores in the micropore zeolite [29]. The process of dealumination of zeolite can be simply summarized into two steps: Firstly, water is used to extract Al from the framework (hydrolysis process) to form EFAl and secondly the formed EFAl is condensed in the pore or the surface of the zeolite [30]. The structure of the zeolite is still maintained during this process [31](Figure 1.6).

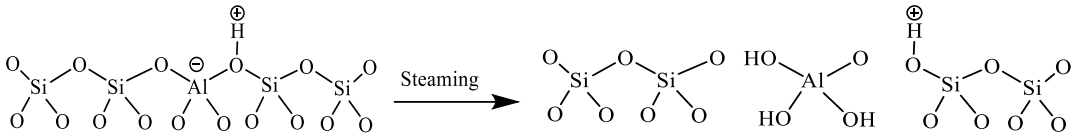

Figure 1.6. Steaming process of MFI zeolite.

1.4.1 Reaction pathways of dealumination

During the dealumination process of zeolite, four Al-O are released from the framework and an EFAl $Al(OH)_3(H_2O)$ is formed accordingly. For sequential dissociation of one Al-O bond of zeolite, four type of states are included in the pathway and the hydrolysis process of the first Al-O bond of zeolite is displayed in the Figure 1.7 [30]:

(1) Water adsorption: Before hydrolysis, water is bound directly to the Al in a Lewis acid-base-type interaction. Water molecule is adsorbed on the lowest energy site.

(2) Initiation state: Initiation of hydrolysis of the framework Al (FAl).

(3) Transition state.

(4) Final state.

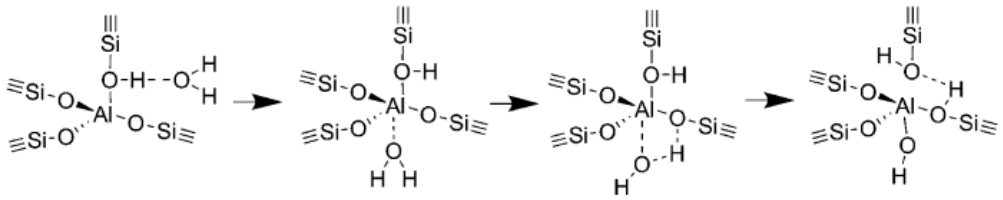

Water adsorption Initiation state Transition state Final state

Figure 1.7. The first mechanism of the cleavage of the first Al-O(H) in the zeolite (Take from reference [30, 32]).

1.4.2 Dealumination mechanisms of zeolite

Two mechanisms of dealumination of zeolites were studied. In the first mechanism (Figure 1.7), one water molecule is adsorbed on the BAS of the zeolite and then located at reverse side of the Al-O(H) bond connected with the BAS at initiation state. As the adsorbed water molecule in the initiation state is at opposite position of the Al-O(H) bond, thus this mechanism is called back adsorption. In the transition state, one of H in the adsorbed water coordinated with the O in the nearest Al-O-Si bond in the framework. The remained OH in the adsorbed water is still bound to the Al and the Al-O(H) bond connected with the BAS is cleaved [30, 32]. The O in the cleaved Al-O(H) bond also coordinated with the H, which is connected with the nearest Al-O-Si bond at the final state.

In the second dealumination mechanism (Figure 1.8), water is adsorbed at the same direction as the Al in the Al-O(H) bond in the initiation state. Thereafter, the H in the adsorbed water is donated to the O in the nearest Al-O-Si bond in the transition state. This mechanism is named as front adsorption [30, 32].

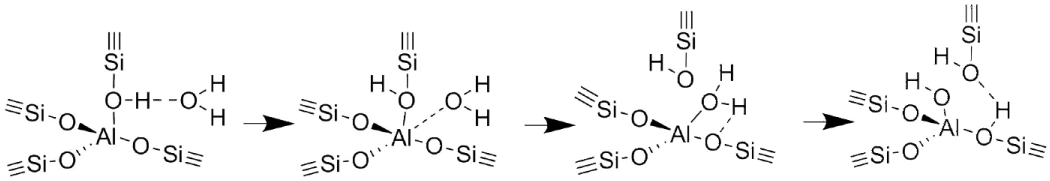

Figure 1.8. The second mechanism of the cleavage of the first Al-O(H) bond in the zeolite (Take from reference).

The distance of the Al-O(H) bond in the MFI zeolite and the energy barrier at each state for the first dealumination mechanism is illustrated in the Figure 1.9. After the water is adsorbed on the Al, the specie I0 is formed in the initiation state with the energy barrier of −70 kJ mol^{-1} and the Al−O(H) distance increases from 1.90 to 2.28 Å. In the first transition state (TS1), the energy barrier is 86 kJ mol^{-1}. After the transition state, an intermediate is formed and the Al−O(H) increases from 3.09 Å to 3.14 Å, even though the activation energy is 0. After passing by the second transition state, the more stable product is formed with -44 kJ mol^{-1} energy barrier [32].

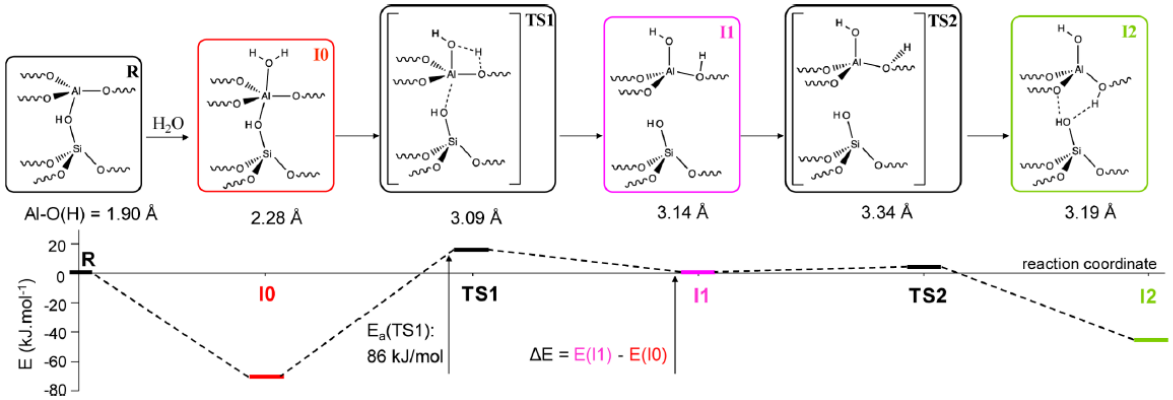

Figure 1.9. The Al-O(H) bond distance at T_3O_4 in MFI and the energy barrier for each state in the first dealumination mechanism. The I0 stands for the adsorption of water in the opposite position to the Al-O-H bond in the initial state, the TS1 stands for the proton donated to the O in the nearest Al-O-Si bond in the transition state, TS2 stands for the rotation of a proton and I2 is named as the most stable product (Take from reference [32]).

1.5 Heterogeneous catalytic reaction

1.5.1 The stages of heterogeneous catalysis

In heterogeneous catalysis, the catalysts and reactants are in different phases. Usually the catalysts are in solid phase and the reactants are in the gas phase. Heterogeneous catalysis has five stages depend on surface adsorption theory: diffusion of reactants to the catalysts surface, adsorption of the reactants, reaction, desorption of the products and the diffusion of products out of the catalysts surface.

1.5.2 Physisorption and chemisorption

Adsorption of reactants on the active sites of the catalysts includes physisorption and chemisorption [33-35].

Physisorption: The reactant is adsorbed in the channel of the catalyst via van der Waal force without new chemical bond form and old chemical bond cleavage. The physisorptoin is always exothermal and usually the physisorption heat is small (10 kJ mol^{-1}). Physisorption rate is fast, which is not influenced by temperatures. The adsorbed reactant is not stable and can be desorbed completely. The physisorption molecule layers can be formed from monolayer to multilayer.

Chemisorption: The chemisorption is that the reactant molecule is adsorbed on the active site of catalyst via chemical bond. The chemisorption heat is larger than physisorption heat and it is similar with the reaction heat (40-800 kJ mol^{-1}). The chemisorption rate is slow and increases

with temperature, which needs activation energy. The chemisorption usually is monolayer adsorption. The chemisorbed specie is quite stable and its desorption usually is accompanied with chemical reaction.

1.5.3 Langmuir adsorption model

Langmuir adsorption model is widely used in the heterogeneous catalysis nowdays [36-40], which was firstly proposed by Langmuir in 1916 [41], as it can be used in both physisorption and chemisorption. Some assumptions are applied to describe the Langmuir adsorption model:

(1) Adsorption sites are existed in the surface of the adsorbent and each adsorption site is able to adsorb one molecule.
(2) Adsorption sites are homogeneous thermodynamically and kinetically.
(3) Adsorbate molecules cannot interact with each other.
(4) The adsorbed molecule is in adsorption and desorption equilibrium.

A typical Langmuir adsorption isotherm is illustrated in Figure 1.10 based on the equation (2).

$$\theta = \frac{K^{\circ}_{\mathrm{ads}} p}{1+K^{\circ}_{\mathrm{ads}} p} \qquad (2)$$

Where θ is coverage of adsorbate on the adsorption sites of catalyst, K°_{ads} is the standard state adsorption equilibrium constant and p is the gas pressure normalized to 1 bar.

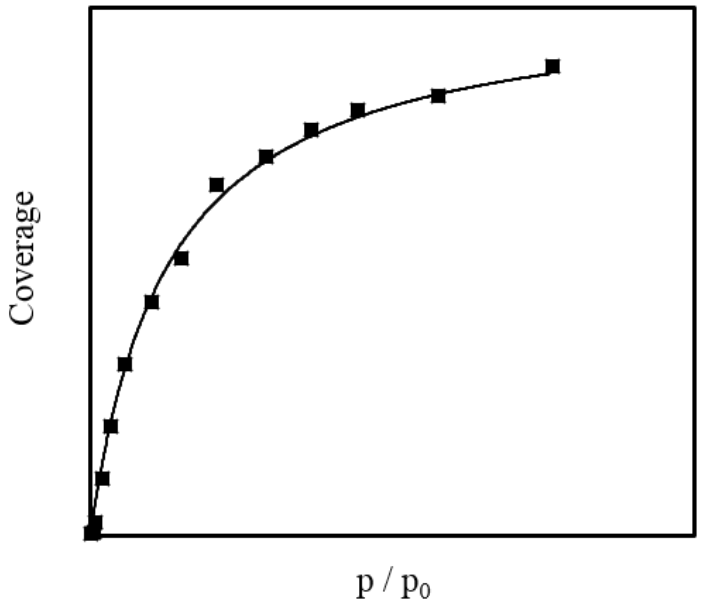

Figure 1.10. Langmuir adsorption isotherm of pentane on H-MFI zeolite at 343 K between 0.002 and 0.85 mbar.

The standard state adsorption equilibrium constant K°_{ads} can be attained by fitting of the Langmuir adsorption isotherm. The K°_{ads} is also related to Gibbs free energy by using equation (3).

$$K^{\circ}_{ads} = exp(\frac{-\Delta G^{\circ}_{ads}}{RT}) \quad (3)$$

The Gibbs free energy can be derived from adsorption enthalpy and entropy in equation (4).

$$\Delta G^{\circ}_{ads} = \Delta H^{\circ}_{\mathrm{ads}} - \mathrm{T}\Delta S^{\circ}_{\mathrm{ads}} \quad (4)$$

Combing equation 3 and 4, the adsorption entropy and adsorption enthalpy can be obtained by using the linear form of van't Hoff equation (5).

$$\ln K^{\circ}_{\mathrm{ads}} = -\frac{\Delta H^{\circ}_{\mathrm{ads}}}{RT} + \frac{\Delta S^{\circ}_{\mathrm{ads}}}{R} \quad (5)$$

In which, $\Delta H^{\circ}_{\mathrm{ads}}$, $\Delta S^{\circ}_{\mathrm{ads}}$ and $\Delta G^{\circ}_{\mathrm{ads}}$ are the standard adsorption enthalpy, entropy and Gibbs free energy.

The $\Delta H^{\circ}_{\mathrm{ads}}$ and $\Delta S^{\circ}_{\mathrm{ads}}$ almost do not change when temperature range is small, so the straight line of ln K°_{ads} vesus 1/T can be used to calculate the $\Delta H^{\circ}_{\mathrm{ads}}$ and $\Delta S^{\circ}_{\mathrm{ads}}$.

1.5.4 Surface reactions

Surface reactions are at the heart of catalytic reactors that are used to produce a large fraction of industrial chemicals and they are extremely important for the heterogeneous catalysis reaction. Surface reactions, by definition, are reactions that at least one of the steps are the adsorption of one or more reactants in the reaction mechanism. The reaction mechanisms for the bimolecular reaction can be divided into three classes as shown in scheme 1.1: interaction between two species adsorbed simultaneously on the surface (Langmuir-Hinshelwood mechanism), and interaction between an adsorbed molecule and second molecule in the gas phase (Eley-Rideal mechanism) or in mobile precursor state (Precursor mechanism).

(1) **Langmuir-Hinshelwood mechanism:**

Both molecule (A) and (B) adsorb on the surface and then they diffuse and react until a new molecule A-B is formed which is desorbed from the surface finally [42].

(2) **Eley-Rideal mechanism:**

One molecule (A) adsorbs on the surface and second molecule (B) does not adsorb on the surface but it interacts with the already adsorbed A, so that the A-B molecule is formed and then it is desorbed from the surface [42].

(3) **Precursor mechanism:**

One molecule (A) adsorbs on the surface. Second molecule (B) collides with the surface and a mobile precursor state (B) is formed. The molecule (B) collides with molecule (A) on the surface and then they react to from a new A-B molecule [43, 44].

(1) Langmuir-Hinshelwood mechanism

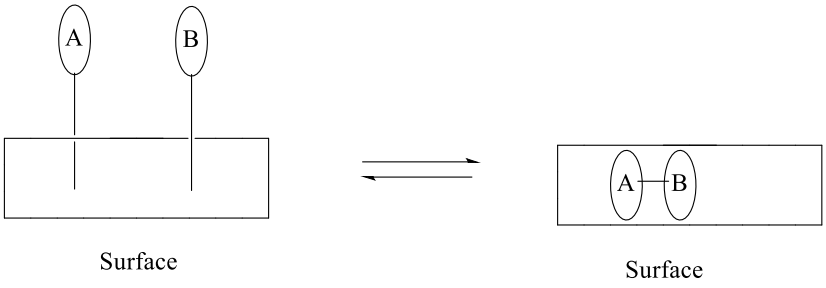

(2) Eley-Rideal mechanism

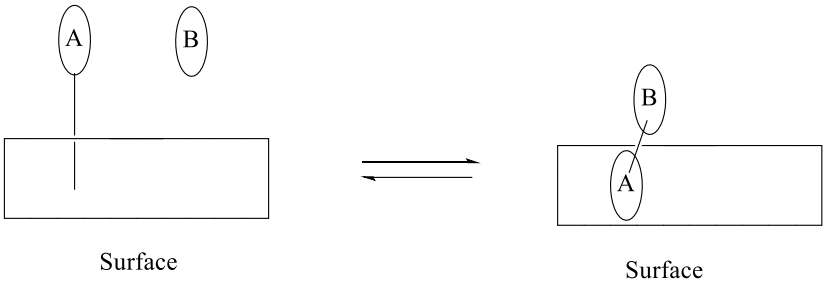

(3) Precursor mechanism

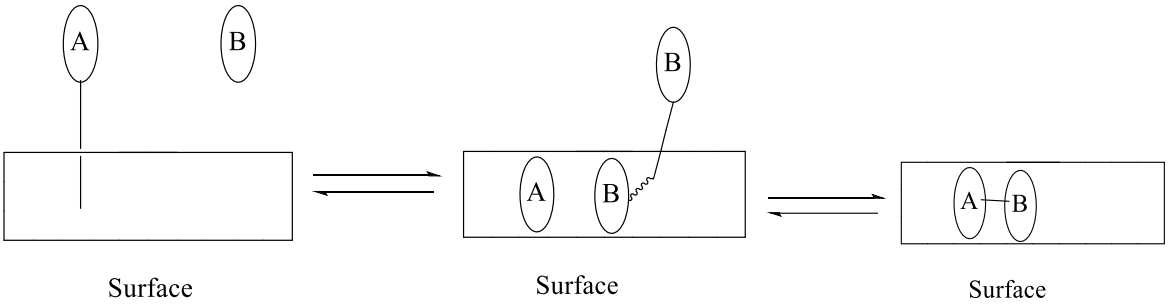

Scheme 1.1. Schematic illustration of mechanism of bimolecular surface reaction on the heterogeneous catalyst.

1.6 Effect of EFAl on the catalytic activity of BAS of zeolite

The presence of EFAl after short steaming periods has been reported to have a positive impact on the rate of hydrocarbon transformations on the BAS of zeolites [28, 31, 45-50]. Contradicting explanations have been proposed for the promotional effect of EFAl on cracking of alkanes [31, 51-54]. In general, the models focus on synergistic effects between BAS and adjacent EFAl sites, increasing the acid strength of the former [26, 31, 52, 55]. Haag et al. [56] proposed that partially hydrolyzed framework Al coordinates to the bridging OH group, increasing its acid strength by the additional interactions with oxygen. Masuda et al. [31]

confirmed these findings noting that the catalytic activity of MFI for n-hexane cracking first increased and later decreased with steaming time. These changes were related to partially distorted octahedral aluminum atoms in MFI. Li et al. [26] gave evidence for the spatial proximity of Brønsted and Lewis acid sites in dealuminated HY zeolite using ^{1}H DQ MAS solid-state NMR. Density function theory (DFT) calculations [26, 55] showed that EFAl, such as $Al(OH)_3$ and $AlOH_2^+$, coordinating to one or two lattice oxygen sites increased the acid strength of a neighboring bridging OH group. In a different approach, Bokhoven et al. [53] argued that the higher adsorption heat of propane in steamed H-MOR is responsible for the increase in catalytic cracking activity. In contrast, Gounder et al. [57] explained the high activity for cracking and dehydrogenation of isobutane on steamed FAU zeolites with a better stabilization of the transition states by the narrower space in the pores containing EFAl oxide clusters.

1.7 Motivation and scope of the thesis

Even though some theoretical and experimental explanations for the influence of EFAl on the BAS in the activity of hydrocarbon transformations have been developed [26, 31, 56], their intrinsic kinetic data on the BAS with EFAl in close proximity is still not fully attained. In this doctoral thesis, the kinetic of pentane cracking and ethene dimerization has been systematically investigated. In addition, effect of the EFAl on the adsorption state and carbenium ion like transition state of pentane cracking and ethene dimerization on the BAS of H-MFI zeolite has been explored.

Some studies evidenced the space proximity between EFAl-OH and BAS-OH using the NMR methods [23, 26, 58]. However, the proximity of the EFAl on the SBAS is few evidenced. In addition, quantification of the SBAS with EFAl in close proximity (EFAl-SBAS) is also needed. In chapter 2, H-MFI zeolites with different percentage of EFAl-SBAS were synthesized by steaming treatment at different steaming conditions. In comparison, the SBAS without EFAl in close proximity (I-SBAS) was attained by ammonia hexafluorosilicate (AHFS) treatment. In order to evidence the space proximity of EFAl to SBAS, IR spectra of adsorbed pyridine on the H-MFI sample with the highest content of EFAl-SBAS and the H-MFI sample with only I-SBAS have been done at 723 K. Once evidence such space proximity, the percentage and concentration of the EFAl-SBAS and I-SBAS in H-MFI zeolite was attained.

After quantifying the content of EFAl-SBAS and I-SBAS in H-MFI zeolite, it is important to investigate how the EFAl-SBAS influences the properties of alkene-derived intermediates or carbenium ion like transition state in the C-C bond cleavage and formation reactions, such as alkane cracking and alkene dimerization. In chapter 3, adsorption of pentane on BAS-OH and EFAl-OH and adsorption thermodynamics of pentane on EFAl-SBAS and I-SBAS has been explored. In addition, the effect of the EFAl on the SBAS in each pentane cracking and dehydrogenation pathways activity and also their intrinsic properties has been probed.

The adsorption of alkene on zeolite is more complex than alkane adsorption, as alkene can easily dimerize at very low temperature. In comparison with the C-C cleavage on the I-SBAS and EFAl-SBAS, the ethene dimerization on the two sites is studied in chapter 4. In addition, the reaction mechanism of ethene dimerization and the rate determining step on the SBAS is explored. The role of EFAl on the transition state enthalpy and entropy of ethene dimerization has also been investigated. The EFAl is reported to promote the deactivation of a zeolite in alkane cracking [59] and whether EFAl increase the deactivation of a catalyst in ethene dimerization has also been explored.

1.8 Associated content

Figure 1.1 reprinted with permission from (J. Weitkamp, *Solid State Ionics*, 131 (**2000**) 175–188.). License number: 4472411275359.

Figure 1.2 reprinted with permission from (M. Marques, S. Moreira, *Journal of Molecular Catalysis A: Chemical*, 192(**2003**) 93-101.). License number: 4472440171591.

Figure 1.7, Figure 1.8 and Figure 1.9 reprinted with permission from (M. Silaghi, C. Chizallet, E. Petracovschi, T. Kerber, J. Sauer, P. Raybaud, *ACS Catalysis*, 5(**2015**) 11-15.) Copyright (2015) American Chemical Society.

1.9 References

[1] B.M. Weckhuysen, J. Yu, Recent advances in zeolite chemistry and catalysis, *Chemical Society Reviews*, 44 (**2015**) 7022-7024.

[2] C.J. Rhodes, Zeolites: physical aspects and environmental applications, Annual Reports Section "C" (*Physical Chemistry*), 103 (**2007**) 287-325.

[3] S. Wang, Y. Peng, Natural zeolites as effective adsorbents in water and wastewater treatment, *Chemical Engineering Journal*, 156 (**2010**) 11-24.

[4] R.P. Townsend, E.N. Coker, Chapter 11 Ion exchange in zeolites, in: H. van Bekkum, E.M. Flanigen, P.A. Jacobs, J.C. Jansen (Eds.) *Studies in Surface Science and Catalysis*, Elsevier, **2001**, pp. 467-524.

[5] J.L. Casci, Zeolite molecular sieves: preparation and scale-up, *MICROPOR MESOPOR MAT*, 82 (**2005**) 217-226.

[6] J. Weitkamp, Zeolites and catalysis, *Solid State Ionics*, 131 (**2000**) 175-188.

[7] J. Bandiera, M. Dufaux, Y.B. Taârit, Effect of the brønsted acid site strength on the cracking and dehydrogenating properties in propane conversion evidence for the soft-soft/hard-hard acid-base interaction concept, *Applied Catalysis A:general*, 148 (**1997**) 283-300.

[8] A. Corma, Inorganic Solid Acids and Their Use in Acid-Catalyzed Hydrocarbon Reactions, *Chemical Reviews*, 95 (**1995**) 559-614.

[9] F. Eder, M. Stockenhuber, J.A. Lercher, Brønsted Acid Site and Pore Controlled Siting of Alkane Sorption in Acidic Molecular Sieves, *The Journal of Physical Chemistry B*, 101 (**1997**) 5414-5419.

[10] Recommended nomenclature for zeolite minerals; report of the Subcommittee on Zeolites of the International Mineralogical Association, Commission on New Minerals and Mineral Names, *The Canadian Mineralogist*, 35 (**1997**) 1571-1606.

[11] M. Daramola, E. Aransiola, T. Ojumu, Potential Applications of Zeolite Membranes in Reaction Coupling Separation Processes, *Materials*, 5 (**2012**) 2101.

[12] M.d.F.V. Marques, S.C. Moreira, ZSM-5 acid zeolite supported metallocene catalysts for ethylene polymerization, *Journal of Molecular Catalysis A: Chemical*, 192 (**2003**) 93-101.

[13] D.E. Perea, I. Arslan, J. Liu, Z. Ristanović, L. Kovarik, B.W. Arey, J.A. Lercher, S.R. Bare, B.M. Weckhuysen, Determining the location and nearest neighbours of aluminium in zeolites with atom probe tomography, *Nature Communications*, 6 (**2015**) 7589.

[14] G.T. Kokotailo, S.L. Lawton, D.H. Olson, W.M. Meier, Structure of synthetic zeolite ZSM-5, *Nature*, 272 (**1978**) 437.

[15] W.O. Haag, R.M. Dessau, R.M. Lago, Kinetics and Mechanism of Paraffin Cracking with Zeolite Catalysts, in: T. lnui, S. Namba, T. Tatsumi (Eds.) *Studies in Surface Science and Catalysis*, Elsevier, **1991**, pp. 255-265.

[16] G.L. Woolery, G.H. Kuehl, H.C. Timken, A.W. Chester, J.C. Vartuli, On the nature of framework Brønsted and Lewis acid sites in ZSM-5, *Zeolites*, 19 (**1997**) 288-296.

[17] M. Hara, K. Nakajima, K. Kamata, Recent progress in the development of solid catalysts for biomass conversion into high value-added chemicals, *Science and Technology of Advanced Materials*, 16 (**2015**) 034903.

[18] R.A. van Santen, G.J. Kramer, Reactivity Theory of Zeolitic Broensted Acidic Sites, *Chemical Reviews*, 95 (**1995**) 637-660.

[19] A. Corma, From Microporous to Mesoporous Molecular Sieve Materials and Their Use in Catalysis, *Chemical Reviews*, 97 (**1997**) 2373-2420.

[20] P. Demontis, G.B. Suffritti, Structure and Dynamics of Zeolites Investigated by Molecular Dynamics, *Chemical Reviews*, 97 (**1997**) 2845-2878.

[21] R. Fricke, H. Kosslick, G. Lischke, M. Richter, Incorporation of Gallium into Zeolites: Syntheses, Properties and Catalytic Application, *Chemical Reviews*, 100 (**2000**) 2303-2406.

[22] I. Kiricsi, H. Förster, G. Tasi, J.B. Nagy, Generation, Characterization, and Transformations of Unsaturated Carbenium Ions in Zeolites, *Chemical Reviews*, 99 (**1999**) 2085-2114.

[23] N. Xue, A. Vjunov, S. Schallmoser, J.L. Fulton, M. Sanchez-Sanchez, J.Z. Hu, D. Mei, J.A. Lercher, Hydrolysis of zeolite framework aluminum and its impact on acid catalyzed alkane reactions, *Journal of Catalysis*, 365 (**2018**) 359-366.

[24] S.M.T. Almutairi, B. Mezari, G.A. Filonenko, P.C.M.M. Magusin, M.S. Rigutto, E.A. Pidko, E.J.M. Hensen, Influence of Extraframework Aluminum on the Brønsted Acidity and Catalytic Reactivity of Faujasite Zeolite, *ChemCatChem*, 5 (**2013**) 452-466.

[25] D.C. Koningsberger, J.T. Miller, The development of strong acidity by non-framework aluminum in H-USY determined by Al XAFS spectroscopy, *Studies in Surface Science and Catalysis*, 101 (**1996**) 841-850.

[26] S. Li, A. Zheng, Y. Su, H. Zhang, L. Chen, J. Yang, C. Ye, F. Deng, Brønsted/Lewis Acid Synergy in Dealuminated HY Zeolite: A Combined Solid-State NMR and Theoretical Calculation Study, *Journal of the American Chemical Society*, 129 (**2007**) 11161-11171.

[27] A.J. Jones, E. Iglesia, The Strength of Brønsted Acid Sites in Microporous Aluminosilicates, *ACS Catalysis*, 5 (**2015**) 5741-5755.

[28] S. Schallmoser, T. Ikuno, M.F. Wagenhofer, R. Kolvenbach, G.L. Haller, M. Sanchez-Sanchez, J.A. Lercher, Impact of the local environment of Brønsted acid sites in ZSM-5 on the catalytic activity in n-pentane cracking, *Journal of Catalysis*, 316 (**2014**) 93-102.

[29] J.C. Groen, W. Zhu, S. Brouwer, S.J. Huynink, F. Kapteijn, J.A. Moulijn, J. Pérez-Ramírez, Direct Demonstration of Enhanced Diffusion in Mesoporous ZSM-5 Zeolite Obtained via Controlled Desilication, *Journal of the American Chemical Society*, 129 (**2007**) 355-360.

[30] M. Nielsen, R.Y. Brogaard, H. Falsig, P. Beato, O. Swang, S. Svelle, Kinetics of Zeolite Dealumination: Insights from H-SSZ-13, *ACS Catalysis*, 5 (**2015**) 7131-7139.

[31] T. Masuda, Y. Fujikata, S.R. Mukai, K. Hashimoto, Changes in catalytic activity of MFI-type zeolites caused by dealumination in a steam atmosphere, *Applied Catalysis A:general*, 172 (**1998**) 73-83.

[32] M.-C. Silaghi, C. Chizallet, E. Petracovschi, T. Kerber, J. Sauer, P. Raybaud, Regioselectivity of Al–O Bond Hydrolysis during Zeolites Dealumination Unified by Brønsted–Evans–Polanyi Relationship, *ACS Catalysis*, 5 (**2015**) 11-15.

[33] C.M. Nguyen, B.A. De Moor, M.-F. Reyniers, G.B. Marin, Physisorption and Chemisorption of Linear Alkenes in Zeolites: A Combined QM-Pot(MP2//B3LYP:GULP)–Statistical Thermodynamics Study, *The Journal of Physical Chemistry C*, 115 (**2011**) 23831-23847.

[34] M. Thommes, K. Kaneko, A.V. Neimark, J.P. Olivier, F. Rodriguez-Reinoso, J. Rouquerol, K.S. Sing, Physisorption of gases, with special reference to the evaluation of surface area and pore size distribution (IUPAC Technical Report), *Pure and Applied Chemistry*, 87 (**2015**) 1051-1069.

[35] K.S. Sing, Reporting physisorption data for gas/solid systems with special reference to the determination of surface area and porosity (Recommendations 1984), *Pure and applied chemistry*, 57 (**1985**) 603-619.

[36] G.C. Laredo, J. Castillo, J.O. Marroquin, Dual-site Langmuir modeling of the liquid phase adsorption of linear and branched paraffins onto a PVDC carbon molecular sieve, *Fuel*, 102 (**2012**) 404-413.

[37] C. Nguyen, D.D. Do, Dual Langmuir Kinetic Model for Adsorption in Carbon Molecular Sieve Materials, *Langmuir*, 16 (**2000**) 1868-1873.

[38] R.E. Richards, L.V.C. Rees, Sorption and packing of n-alkane molecules in ZSM-5, *Langmuir*, 3 (1987) 335-340.

[39] C. Chmelik, J. Kärger, M. Wiebcke, J. Caro, J.M. van Baten, R. Krishna, Adsorption and diffusion of alkanes in CuBTC crystals investigated using infra-red microscopy and molecular simulations, *MICROPOR MESOPOR MAT*, 117 (**2009**) 22-32.

[40] B. Chen, C. Liang, J. Yang, D.S. Contreras, Y.L. Clancy, E.B. Lobkovsky, O.M. Yaghi, S. Dai, A Microporous Metal–Organic Framework for Gas-Chromatographic Separation of Alkanes, *Angewandte Chemie International Edition*, 45 (**2006**) 1390-1393.

[41] I. Langmuir, THE CONSTITUTION AND FUNDAMENTAL PROPERTIES OF SOLIDS AND LIQUIDS. PART I. SOLIDS, *Journal of the American Chemical Society*, 38 (**1916**) 2221-2295.

[42] R. Liang, A. Hu, M. Hatat-Fraile, N. Zhou, Fundamentals on Adsorption, Membrane Filtration, and Advanced Oxidation Processes for Water Treatment, in: A. Hu, A. Apblett (Eds.) Nanotechnology for Water Treatment and Purification, Springer International Publishing, Cham, 2014, pp. 1-45.

[43] B. Fluckiger, M.J. Rossi, Common Precursor Mechanism for the Heterogeneous Reaction of D2O, HCl, HBr, and HOBr with Water Ice in the Range 170−230 K: Mass Accommodation Coefficients on Ice, *The Journal of Physical Chemistry A*, 107 (**2003**) 4103-4115.

[44] J. Harris, B. Kasemo, On precursor mechanisms for surface reactions, *Surface Science Letters*, 105 (**1981**) L281-L287.

[45] S.M. Babitz, B.A. Williams, J.T. Miller, R.Q. Snurr, W.O. Haag, H.H. Kung, Monomolecular cracking of n-hexane on Y, MOR, and ZSM-5 zeolites, *Applied Catalysis A:general*, 179 (**1999**) 71-86.

[46] D.P. Ivanov, L.V. Pirutko, G.I. Panov, Effect of steaming on the catalytic performance of ZSM-5 zeolite in the selective oxidation of phenol by nitrous oxide, *Journal of Catalysis*, 311 (**2014**) 424-432.

[47] E. Loeffler, U. Lohse, C. Peuker, G. Oehlmann, L.M. Kustov, V.L. Zholobenko, V.B. Kazansky, Study of different states of nonframework aluminum in hydrothermally dealuminated HZSM-5 zeolites using diffuse reflectance i.r. spectroscopy, *Zeolites*, 10 (**1990**) 266-271.

[48] M. Maache, A. Janin, J.C. Lavalley, J.F. Joly, E. Benazzi, Acidity of zeolites Beta dealuminated by acid leaching: An FTi.r. study using different probe molecules (pyridine, carbon monoxide), *Zeolites*, 13 (**1993**) 419-426.

[49] J.P. Marques, I. Gener, P. Ayrault, J.C. Bordado, J.M. Lopes, F. Ramôa Ribeiro, M. Guisnet, Infrared spectroscopic study of the acid properties of dealuminated BEA zeolites, *MICROPOR MESOPOR MAT*, 60 (**2003**) 251-262.

[50] H. Krannila, W.O. Haag, B.C. Gates, Monomolecular and bimolecular mechanisms of paraffin cracking: n-butane cracking catalyzed by HZSM-5, *Journal of Catalysis*, 135 (**1992**) 115-124.

[51] Z. Yu, S. Li, Q. Wang, A. Zheng, X. Jun, L. Chen, F. Deng, Brønsted/Lewis Acid Synergy in H–ZSM-5 and H–MOR Zeolites Studied by 1H and 27Al DQ-MAS Solid-State NMR Spectroscopy, *The Journal of Physical Chemistry C*, 115 (**2011**) 22320-22327.

[52] R.M. Lago, W.O. Haag, R.J. Mikovsky, D.H. Olson, S.D. Hellring, K.D. Schmitt, G.T. Kerr, The Nature of the Catalytic Sites in HZSM-5- Activity Enhancement, *Studies in Surface Science and Catalysis*, 28 (**1986**) 677-684.

[53] J.A. van Bokhoven, M. Tromp, D.C. Koningsberger, J.T. Miller, J.A.Z. Pieterse, J.A. Lercher, B.A. Williams, H.H. Kung, An Explanation for the Enhanced Activity for Light Alkane Conversion in Mildly Steam Dealuminated Mordenite: The Dominant Role of Adsorption, *Journal of Catalysis*, 202 (**2001**) 129-140.

[54] J.A. van Bokhoven, B.A. Williams, W. Ji, D.C. Koningsberger, H.H. Kung, J.T. Miller, Observation of a compensation relation for monomolecular alkane cracking by zeolites: the dominant role of reactant sorption, *Journal of Catalysis*, 224 (**2004**) 50-59.

[55] S. Li, S.-J. Huang, W. Shen, H. Zhang, H. Fang, A. Zheng, S.-B. Liu, F. Deng, Probing the Spatial Proximities among Acid Sites in Dealuminated H-Y Zeolite by Solid-State NMR Spectroscopy, *The Journal of Physical Chemistry C*, 112 (**2008**) 14486-14494.

[56] W.O. Haag, Catalysis by Zeolites – Science and Technology, in: J. Weitkamp, H.G. Karge, H. Pfeifer, W. Hölderich (Eds.) *Studies in Surface Science and Catalysis*, Elsevier, **1994**, pp. 1375-1394.

[57] R. Gounder, A.J. Jones, R.T. Carr, E. Iglesia, Solvation and acid strength effects on catalysis by faujasite zeolites, *Journal of Catalysis*, 286 (**2012**) 214-223.

[58] C. Martineau-Corcos, J. Dědeček, F. Taulelle, 27Al-27Al double-quantum single-quantum MAS NMR: Applications to the structural characterization of microporous materials, *Solid State Nuclear Magnetic Resonance*, 84 (**2017**) 65-72.

[59] Q.L. Wang, G. Giannetto, M. Guisnet, Dealumination of zeolites III. Effect of extra-framework aluminum species on the activity, selectivity, and stability of Y zeolites in n-heptane cracking, *Journal of Catalysis*, 130 (**1991**) 471-482.

Chapter 2

Spatial proximity of extra-framework aluminum oxide to strong Brønsted acid sites

This chapter is based on:

Yang Zhang, Ruixue Zhao, Maricruz Sanchez-Sanchez, Gary L. Haller, Jianzhi Hu, Ricardo Bermejo-Deval*, Yue Liu* and Johannes A. Lercher*, "Promotion of protolytic pentane conversion on H-MFI zeolite by proximity of extra-framework aluminum oxide and Brønsted acid sites" accepted by J. Catal. 2018.

ABSTRACT: A series of H-MFI-15 samples with different percentage of EFAl-SBAS (Strong Brønsted acid sites with extra-framework aluminum oxide in close proximity) were synthesized by changing steaming temperatures, duration and partial pressures. Mild steaming is helpful to create high percentage of EFAl-SBAS and severe steaming reduces the EFAl-SBAS amount in H-MFI-15 samples. After steaming treatment, the Al is removed from the framework to form EFAl in H-MFI samples, which can be evidenced by NMR, IR, XANES and EXAFS techniques. However, the micropore volume and structure of the zeolites keep constant after dealumination. The steric proximity of SBAS and EFAl is deduced from the perturbation of OH groups on extra-framework aluminum oxide by pyridine adsorbed on Brønsted acid sites manifested in the IR spectra. The percentage and concentration of EFAl-SBAS in H-MFI-15 samples are quantified based on the perturbation of EFAl-OH by SBAS at 723 K.

2.1. Introduction

Strong Brønsted acid sites (SBAS) are usually considered as the active sites for the hydrocarbon transformation, such as cracking, methane oxidation and methanol to olefin [1-4]. Extra framework aluminum (hydr)oxide species (EFAl) such as AlO^+, $Al(OH)^{2+}$, $AlOH^{2+}$ and some neutral species such as AlOOH and $Al(OH)_3$, can be extracted from the framework Al of zeolites by steaming treatment, thus the Brønsted acid sites (BAS), SBAS and Lewis acid sites (LAS) concentration will be changed [5, 6]. The BAS strength and the EFAl concentration in the zeolites can be tuned by the steaming conditions such as temperatures, water pressures and time [7-10]. The spatial proximity of EFAl to BAS has been evidenced to increase the hydrocarbon transformation activity on BAS [11-16].

In the past few years, some efforts have been done to evidence the spatial proximity of EFAl to BAS [6, 12, 17, 18]. Li et al. [6] firstly used the ^{1}H double quantum (DQ) MAS NMR to explore the spatial proximities among various acid sites in the dealuminated HY. The presence of pairs of off-diagonal peaks at (1.0, 6.0) and (5.0, 6.0) ppm is related to correlation between EFAl-OH and bridging hydroxyl group of BAS in HY zeolite [6]. Based on the same method, Xue et al. [18] found the off-diagonal peak pairs at (3.8, 6.0) and (2.2, 6.0) ppm using ^{1}H DQ MAS NMR on the steamed H-MFI zeolite, verifying the spatial proximity between EFAl-OH and the OH groups of BAS in the H-MFI zeolite. In addition, Charlotte et al. [17] evidenced that EFAl are close to the framework Al (FAl) in the hydrated HY zeolite by the cross-correlation peaks in the ^{27}Al-^{27}Al DQ-single quantum (SQ) MAS NMR.

These agree well with our previous findings [12], less fraction of EFAl species were found to interact with ammonia compared with pyridine at 723 K, but in fact, the ammonia is more basic than pyridine (pyridine pK_B~9 and NH_3 pK_B~5). They speculated that the interaction of more fraction of EFAl species with pyridine was not due to the acidity of EFAl, but the EFAl interacting with the aromatic ring of pyridine which has already been adsorbed on the SBAS. Therefore, the EFAl can be evidenced to be in close proximity to SBAS. However, this method is not direct and conclusive. In addition, the SBAS are considered as the active sites of some hydrocarbon transformation. The NMR techniques are not able to evidence the space proximity between the EFAl and SBAS.

Therefore, more precise method to evidence the spatial proximity of EFAl and SBAS is imperative. Here, we synthesize a series of zeolites with different percentage of EFAl-SBAS.

The steric proximity of SBAS and EFAl is determined from the perturbation of OH groups on extra-framework aluminum oxide by pyridine adsorbed on Brønsted acid sites in the IR spectra.

2.2 Experimental

Zeolite modification

2.2.1 *Removal of EFAl*

NH_4-MFI-40 (CBV8014, Si/Al = 40) and NH_4-MFI-15(CBV3024, Si/Al = 15) were commercially available from Zeolyst International company. In order to attain H-MFI, NH_4-MFI was calcined in the synthetic air (100 ml min^{-1}) at 823 K for 5 h (10 K min^{-1} heating rate). For purpose of removing of EFAl, NH_4-MFI-15 and NH_4-MFI-40 were treated with $(NH_4)_2SiF_6$ (ammonia hexafluorosilicate, AHFS). Specific steps are following: after deionized water (80 ml) in the flask (250 ml) reached 353 K, AHFS (1.42 g) was dissolved in the deionized water. NH_4-MFI-15/40 (1.92 g) was added into the solution and then stirred for 5 h at the 353 K. The catalyst was separated from the liquid by centrifuge and then washed with hot deionized water (373 K). This procedure was repeated for 10 times and then dried at 373 K overnight. The as formed sample was calcined at 823 K for 5 h in synthetic air (100 ml min^{-1}) with 2 K min^{-1} heating rate. The AHFS treated sample is labeled as H-MFI-15/40(0%).

2.2.2 *Steaming*

The following procedures were used to steam H-MFI-15: H-MFI-15 (2 g) was heated to the target temperature in a rotary quartz tube under N_2 flow (250 ml min^{-1}). After the desired temperature was achieved, deionized water was injected by a Gilson 307 HPLC pump with N_2 flow. Steaming vapor pressure, temperature and duration were changed to get the sample with different percentage of EFAl-SBAS. The steamed MFI samples are designated as H-MFI(x %) and x % is the percentage of EFAl-SBAS in all the SBAS in H-MFI. H-MFI-15(5%) was steamed from H-MFI-15(0%) at 723 K, 10 kPa for 1 h.

H-MFI-40(0%) was also steamed as the procedures above: the sample was steamed for 1 h at 723 K and 100 kPa and H-MFI-40(1%) was attained.

2.2.3 *Na^+ exchange*

Na-MFI-15(43%) was attained by exchange of H-MFI-15(43%) with $NaNO_3$ following the procedures in the literature [19]. H-MFI-15(43%) sample (3 g) was added into $NaNO_3$ aqueous solution (250 ml) with 8.5 M concentration and refluxed at 353K for 15 h. The solid was separated from the liquid by filtration and washed with deionized water (1 L), and then the ion exchanged sample was dried at 373 K overnight. At last the sample was calcined following the same procedure in the AHFS treatment.

2.3 Catalyst characterization

2.3.1 *IR spectroscopy of adsorption of pyridine*

BAS, SBAS and LAS concentration of zeolites were measured by IR spectra of adsorbed pyridine, which were collected on a Nicolet 5700 FT-IR spectrometer with a resolution of 4 cm^{-1}. All spectra were collected from 4000 and 800 cm^{-1} at 423 K. The catalyst wafers were put into the IR cell and activated in vacuum (1×10^{-6} mbar) at 723 K for 1 h with 10 K min^{-1} heating rate. After that, pyridine was dosed into the catalyst at 423 K. After the bridged OH group (3610 cm^{-1}) and EFAl-OH group (3660 cm^{-1}) were fully covered, the samples were evacuated for 1 h and weakly bound pyridine was removed. The areas of the bands at 1570-1510 and 1470-1435 cm^{-1} were integrated to calculate the total BAS and LAS concentration. The integrated molar extinction coefficient (IMEC) of bands at 1570-1510 and 1470-1435 cm^{-1} of pyridine adsorbed on BAS and LAS are 0.73 and 0.96 cm μmol^{-1} respectively [5, 20]. The samples were evacuated for 0.5 h at 723 K with 15 K min^{-1} heating rate to measure SBAS and strong LAS (SLAS) concentration. The BAS and SBAS concentration can be calculated using equation (1). The LAS and SLAS concentration can be calculated by equation (2).

$$C_{BAS} = \frac{IA(1570-1540\ cm^{-1})\pi R^2}{IMEC(1570-1540\ cm^{-1})m} = 4.3R^2\frac{IA(1570-1540\ cm^{-1})}{m} \quad (1)$$

$$C_{LAS} = \frac{IA(1470-1435\ cm^{-1})\pi R^2}{IMEC(1470-1435\ cm^{-1})m} = 3.3R^2\frac{IA(1470-1435\ cm^{-1})}{m} \quad (2)$$

In which, C_{BAS} and C_{LAS} are the concentration of BAS and LAS respectively [$\mu mol\ g^{-1}$], IA is the integrate peak area [cm^{-1}], R is the radius of the wafer [cm^{-1}], m is the catalyst weight [g], which is getting from the calibration line of the catalyst weight and the overtones of framework vibration between 2100-1740 cm^{-1} in the IR spectra of H-MFI (as shown in Figure 2.1).

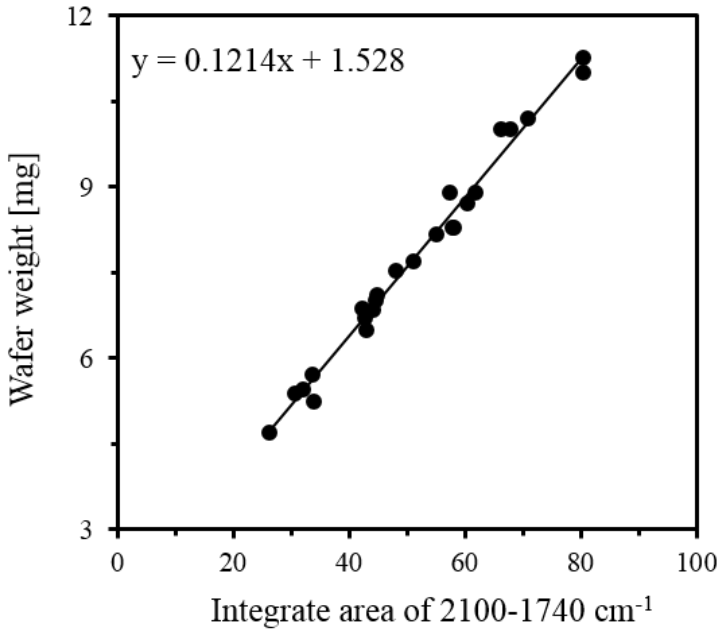

Figure 2.1. Wafer weight as function of integrated area of overtones vibration of framework at 2100-1740 cm^{-1} in the IR of H-MFI zeolite.

2.3.2 *^{27}Al MAS NMR*

^{27}Al single pulse MAS NMR experiments were measured on a Varian-Agilent Inova 63 mm wide-bore 850 MHz NMR spectrometer, which was performed at a main magnetic field of 19.97 T with the corresponding Larmor frequencies of 221.4 MHz. A 3.2 mm pencil type MAS probe was used in the experiment. In a typical experiment, about 15 mg sample powder were loaded in the rotor and measured at ambient temperature. The H-MFI samples were stored under ambient humidity leading to a hydrated state that is expected to contain Al tetrahedra that have minimal distortions and that have the maximum ^{27}Al MAS NMR spectral resolution [21]. A single pulse sequence with a pulse length of 2.0 μs, corresponding to a pulse angle of 45°, was selected for acquiring each ^{27}Al MAS NMR spectrum with a recycle time of 1 s and total accumulation of 5000 scans. The spectra were acquired at a sample spinning rate of 20 kHz ± 2 Hz and were referenced to 1.0 M $Al(NO_3)_3$ in H_2O (0 ppm) using the center of the octahedral peak of solid γ-Al_2O_3 (at 13.8 ppm) as a secondary reference. For quantitative measurements, the weights of samples loaded into the MAS rotor were recorded. The matching and tuning conditions of the RF circuit of the NMR probe were set using a network analyzer. All other experimental conditions were kept identical for all analyzed samples. In this way, the absolute

peak areas normalized to the spectrometer standard were proportional to the Al in the sample. The spectra were analyzed using the MestreNova 8.1 software package. The intensity was normalized to the mass of the sample.

2.3.3 *Nitrogen physisorption*

Zeolite pore volume was measured by N_2 adsorption isotherms at liquid nitrogen temperature on an automated PMI Sorptomatic 1990 instrument. T-plot method was used for calculating the micropore volume. The samples were activated in vacuum at 523 K for 2 h before N_2 adsorption.

2.3.4 *Al K-Edge XANES and EXAFS Measurements*

The Al K–edge XANES and EXAFS measurements were carried out at the Phoenix I, elliptical undulator beamline at the Swiss Light Source (SLS) at the Paul Scherrer Institute. Energy calibration was attained by setting the inflection point of an Al foil spectrum to 1559.6 eV. The double-crystal monochromator utilized a set of $KTiOPO_4$ (011) crystals to provide an energy resolution of about 0.6 eV over a scan range from 1500 to 2100 eV for the Al K-edge, just below the P K-edge. Two Ni-coated mirrors were set at an angle of 1.45° to provide cutoff of higher harmonics. An unfocused 1.0 × 1.0 mm beam having a flux of ∼109 photons/s was used. The sample chamber pressure was held at $\sim 2.5 \times 10^{-4}$ mbar and the sample was dehydrated at 723 K. Measurements were typically performed in fluorescence mode, although several transmission measurements for individual samples were obtained to ascertain the magnitude of the self-absorption corrections. I_0 was measured as total electron yield signal taken from a 0.5 μm thin polyester foil, which was coated with 50 nm of Ni. This I_0 detector was held in a miniaturized vacuum chamber (2.9×10^{-6} mbar), which was separated by a thin Kapton foil from the measurement chamber itself. The X-ray fluorescence was detected using a 4-element Vortex Si-drift diode detector.

For transmission measurement, a Si diode was used. In order to apply self-absorption correction of the XANES and EXAFS spectra of the concentrated standard compounds, a THENA [21-23] software was used to remove the $\chi(k)$ oscillations from the background and, in certain instances. A Fourier filter cutoff distance, Rbkg, of 1.0 Å was used and the atomic background function, $\mu_0(E)$, containing a strong multielectron absorption edge at k = 5.3 $Å^{-1}$ due to the KLII, III

transition was found [24]. The EXAFS data were weighted by k^2 and truncated using a Hanning window with dk = 1.0 $Å^{-1}$ in the range of $1.5 < k < 8.0$ $Å^{-1}$.

2.3.5 *X-ray diffraction patterns*

X-ray powder diffraction (XRD) with a Philips X'Pert Pro system was used to analyze the crystal structures of the zeolites. The Philips X'Pert Pro diffractometer equipped with an X'celerator module using Cu-K radiation operating at 40 kV / 45 mA was applied. The samples were measured in the range from 5 to 70° (2θ) with a scanning rate of 0.017° s^{-1}.

2.4 Identification and quantification of I-SBAS and EFAl-SBAS in H-MFI-15 samples

The percentage of EFAl-SBAS in all the SBAS can be tuned with the steaming water vapor pressure, temperature and duration, as displayed in Figure 2.2-2.4 and Table 2.1. EFAl-SBAS content increases concurrently with the steaming water vapor pressure, reaching a maximum at 10 kPa (43% EFAl-SBAS) and consecutively reducing with incremental pressure (Figure 2.2). Similarly, the number of EFAl-SBAS is relatively high at low steaming temperature (maximum occurs at 723 K), decreasing dramatically in the severe temperature (Figure 2.3 and supplementary Figure 2.1). While, the sample was steamed for 4 h and highest EFAl-SBAS content can be attained, reducing slightly with prolonged steaming duration (Figure 2.4). Therefore, mild steaming is beneficial to produce high percentage of EFAl-SBAS and severe steaming diminish or destroy the EFAl-SBAS sites.

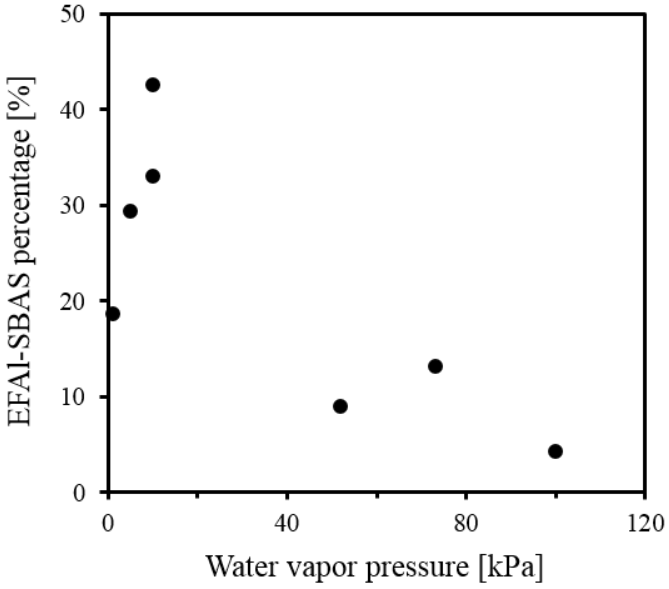

Figure 2.2. Percentage of EFAl-SBAS in H-MFI-15 steamed samples as function of steaming water vapor pressure (Steam at 723 K and 4 h).

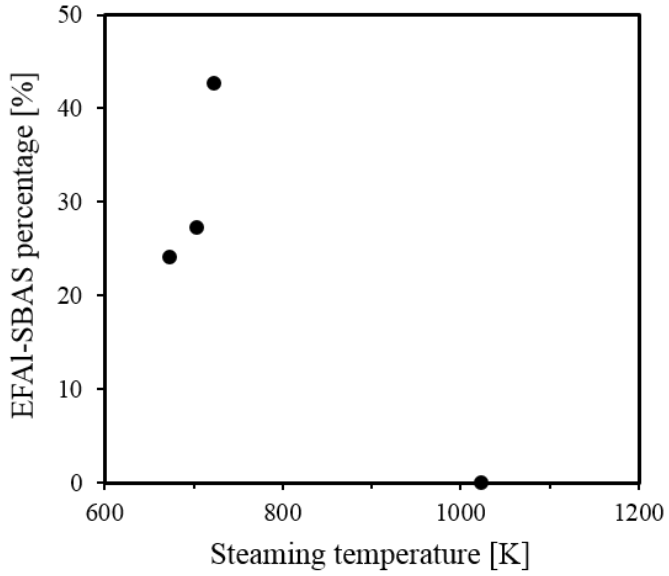

Figure 2.3. Percentage of EFAl-SBAS in H-MFI-15 steamed samples as function of steaming temperature (Steam at 10 kPa and 4 h).

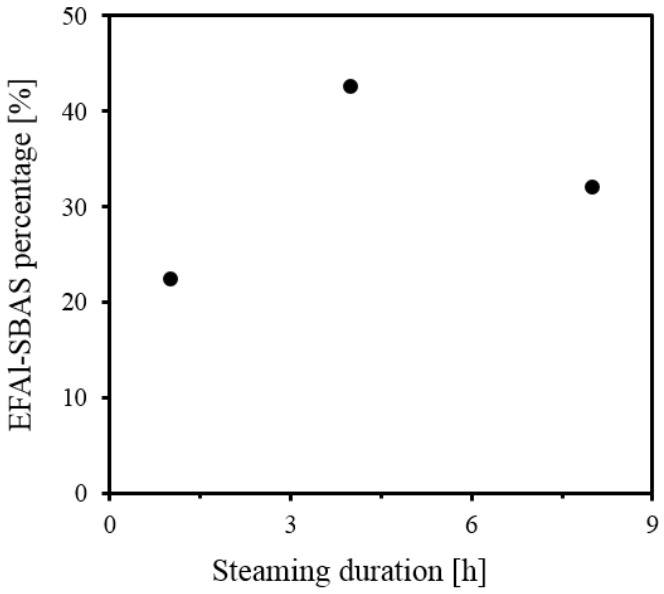

Figure 2.4. Percentage of EFAl-SBAS in H-MFI-15 steamed samples as function of steaming duration (Steam at 10 kPa and 723 K).

Table 2.1. Steaming conditions and percentage of EFAl-SBAS in the H-MFI-15 samples.

Samples	Steaming conditions			EFAl-SBAS Percentage[%]
	Pressure[kPa]	Temperature[K]	Duration[h]	
1	1	723	4	19
2	5	723	4	29
3	10	723	4	33
4[a]	10	723	4	43
5	52	723	4	9
6	73	723	4	13
7	100	723	4	4
8	10	673	4	24
9	10	703	4	27
10	10	1023	4	0
11	10	723	1	23
12	10	723	8	32
13	20	623	4	30

[a]Sample 4 was steamed twice at 723 K, 10 kPa for 4 h.

The ^{27}Al MAS NMR spectra for the H-MFI-15 series are presented in Figure 2.5. On the H-MFI-15 sample, two peaks were identified at 56.4 and 55.1 ppm, which are attributed to tetrahedrally-coordinated FAl [25]. A small peak is shown at 0 ppm, which is associated with hexa-coordinated EFAl [26, 27]. While, the peaks of tetrahedrally-coordinated FAl slightly decreased and the peak of hexa-coordinated EFAl disappeared on H-MFI-15(0%), as the EFAl

and part of FAl were removed after AHFS treatment. For the steamed samples, an additional broad band appeared at about 30 ppm, which is associated with the EFAl in A1OOH tetrahedrally-coordinated with two framework oxygens in close proximity [26, 28] or penta-coordinated EFAl [29-31]. With the percentage of EFAl-SBAS increasing in the steamed samples, the peak intensity of the FAl decreased gradually and the amount of extra-framework Al at 0 and 30 ppm increased correspondingly. As EFAl was extracted from the framework after steaming. Besides, the tetrahedral FAl band became broad and moved to lower chemical shift, which indicates increasing degree of structural distortion of FAl or Al T site was selected removed after steaming [21].

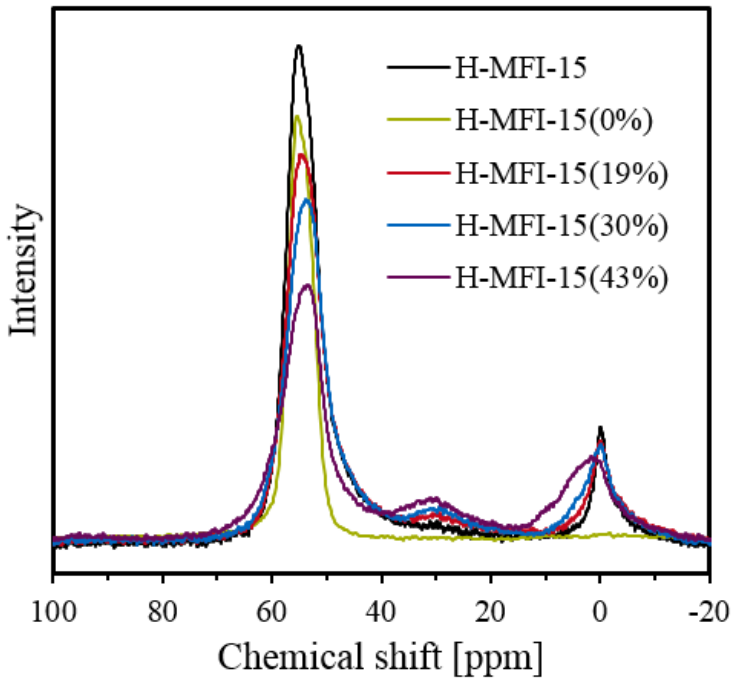

Figure 2.5.[27]Al MAS NMR spectra for the H-MFI-15 samples.

Al X-ray absorption near-edge structure (XANES) and extended X-ray absorption fine structure (EXAFS) of H-MFI-15(0%) and H-MFI-15(43%) were used to explore FAl and EFAl structural and electronic information. Figure 2.6 shows the normalized XANES of H-MFI-15(0%) and H-MFI-15(43%). A whiteline (intensive peak) at position 1564 eV belongs to tetrahedral Al and absorption edge at 1582 eV is attributed to tetrahedral Al with an Al-O bond length of around 1.65-1.75 Å [18, 32]. While, on H-MFI-15(43%) sample, the intensity of the whitelines at 1564 and 1582 eV become lower and a whiteline at position 1569 eV attributing to extra-framework octahedral Al is obviously found, which indicates that tetrahedral Al is extracted from framework to form octaheral Al during steaming process [32].

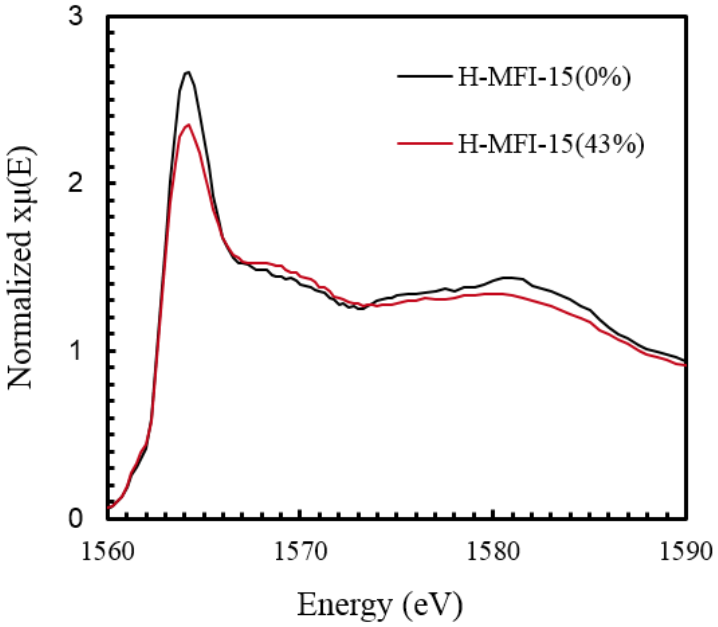

Figure 2.6. XANES of H-MFI-15(0%) and H-MFI-15(43%).

Figure 2.7 shows the EXAFS lmg[χ(R)] and K^2 χ(k) spectra for the H-MFI-15(0%) and H-MFI-15(43%) samples. The H-MFI-15(0%) sample shows an average Al-O bond distance of ~ 1.73 Å [18]. The structure of H-MFI-15(43%) is largely different from that of H-MFI-15(0%) sample. A large percentage of longer Al-O bond is observed in the H-MFI-15(43%) sample. The difference value of Al-O bond distance in H-MFI-15(0%) and H-MFI-15(43%) is about 0.03 Å. This is primarily due to mixture of framework tetrahedral Al and distorted extra-framework Al species in the H-MFI-15(43%) sample, which is agreement with the NMR data.

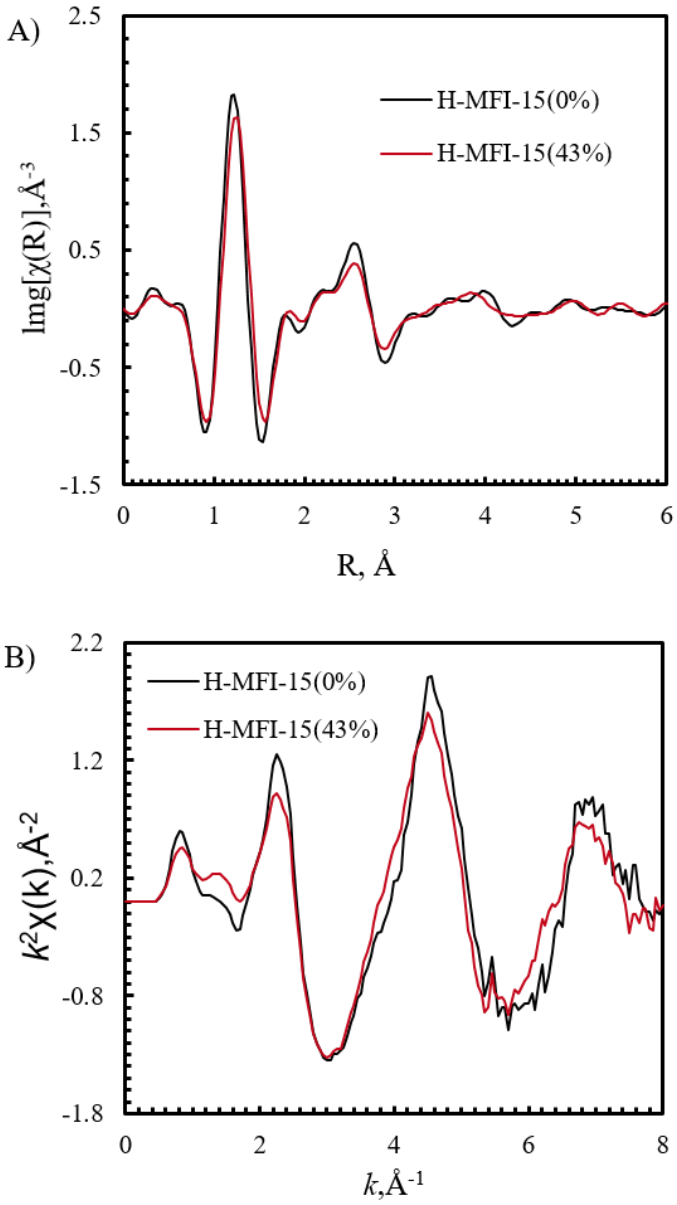

Figure 2.7. The EXAFS of lmg[χ(R)] A) and K^2-weighted χ(k) B) spectra of the H-MFI-15(0%) and H-MFI-15(43%) samples.

This change in Al structure/distribution caused, consequently, a change in BAS, SBAS and LAS concentration in H-MFI-15 (Table 2.2). The BAS and SBAS concentrations for H-MFI-15(0%) were 511 and 422 µmol g^{-1}, respectively. After steaming, concentrations of both acid sites were reduced, especially for the H-MFI-15(43%) with BAS and SBAS concentrations of 209 and 67 µmol g^{-1}, respectively. Correspondingly, the LAS concentration of H-MFI-15(0%) was 27 µmol g^{-1}. It increased for all steamed samples, reaching 193 µmol g^{-1} for the H-MFI-15(43%). In contrast, despite the changes in Al structure/distribution and the variation of BAS and LAS concentrations, the micropore volume was hardly affected. All H-MFI have a

micropore volume of approximately 0.14 $cm^3\ g^{-1}$, except H-MFI-15 (0%) which has a slightly higher micropore volume of 0.16 $cm^3\ g^{-1}$.

The X-ray diffraction patterns (XRD) of the H-MFI-15(0%) and the steamed samples are presented in Figure 2.8. Almost all the diffraction peaks of steamed samples are the same as those of unsteamed material, except a slight decrease of intensity in certain peaks, which confirms that dealumination did not significantly damage the structure of the zeolites.

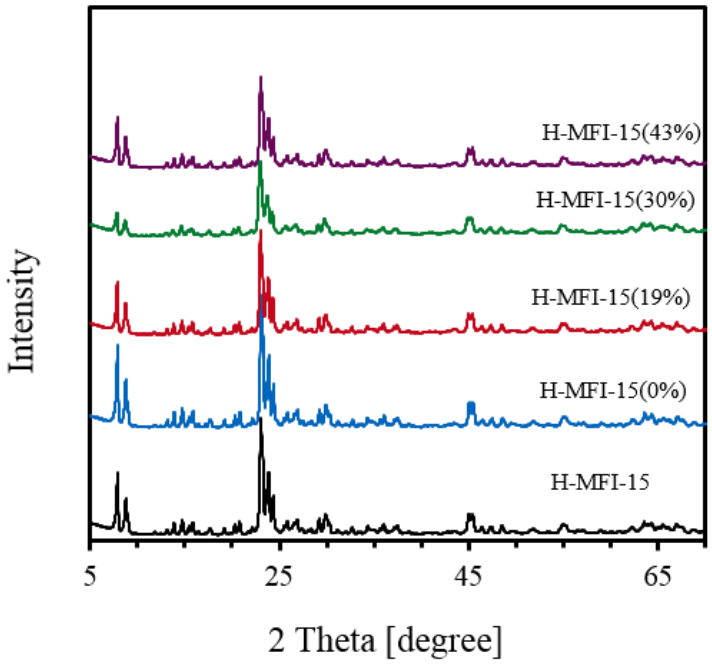

Figure 2.8. X-ray diffraction patterns of H-MFI-15, H-MFI-15(0%) and steamed samples.

Table 2.2 Physiochemical properties of H-MFI-15 with different percentage of EFAl-SBAS.

Sample	Acid site concentration [µmol g^{-1}]					EFAl-SBAS/SBAS	V_{micro}[a]
	BAS[b]	SBAS[b]	LAS[b]	EFAl-SBAS	I-SBAS	[%]	[cm^3 g^{-1}]
H-MFI-15(0%)[c]	511	442	27	0	442	0	0.16
H-MFI-15(4%)[d]	172	120	89	5	115	4	0.14
H-MFI-15(5%)[d]	298	245	54	11	234	5	0.14
H-MFI-15(9%)	188	103	142	9	93	9	0.15
H-MFI-15(19%)	457	308	195	57	251	19	0.14
H-MFI-15(30%)	254	104	210	31	73	30	0.15
H-MFI-15(33%)	221	95	195	31	64	33	0.14
H-MFI-15(43%)	209	67	193	29	38	43	0.14
H-MFI-40(0%)[c]	333	304	13	0	304	0	0.16
H-MFI-40(1%)[e]	142	105	36	1	104	1	0.16

[a]The micropore volume of samples were measured twice and the standard errors are ± 0.005 cm^3 g^{-1}. [b]Determined by IR spectroscopy of adsorbed pyridine; after equilibration 423 K, desorption at 423 K for BAS and LAS and desorption at 723 K for SBAS. [c]H-MFI-15(0%) and H-MFI-40(0%) were attained by AHFS treatment from the parent zeolite. [d]H-MFI-15(5%) was attained by steaming of H-MFI-15(0%) at 723 K and 100 kPa for 1 h. H-MFI-15 (4, 9-43%) were obtained by steaming of parent H-MFI-15(Figure 2.2-2.4 and Table 2.1). [e]H-MFI-40 (1%) was obtained by steaming of H-MFI-40(0%) at 723 K and 100 kPa for 1 h.

The IR spectra from 3900 to 3400 cm^{-1} for H-MFI-15(0%) and H-MFI-15(43%) are shown in Figure 2.9. The band at 3610 cm^{-1} is attributed to bridging hydroxyl groups of BAS [2, 27]. The band at 3740 cm^{-1} is attributed to the stretching vibration of the terminal silanol groups. The band at 3780 cm^{-1} is attributed to OH groups of octahedrally coordinated EFAl [13, 33]. The OH band at 3660 cm^{-1} is also attributed to EFAl species [12, 13, 15]. The absence of the bands at 3660 and 3780 cm^{-1} in H-MFI-15(0%) (Supplementary Figure 2.2) allows to conclude that EFAl was removed by AHFS treatment. For the steamed sample H-MFI-15(43%), the band at 3610 cm^{-1} was reduced drastically compared to H-MFI-15(0%), while the bands at 3660 and 3780 cm^{-1} had a significantly higher intensity.

Upon pyridine adsorption, the band at 3610 cm^{-1} in H-MFI-15(0%) disappeared completely, indicating that all BAS-OH groups interacted with pyridine (Figure 2.9). For H-MFI-15(43%), the band at 3610 cm^{-1} also decreased, but about 20% remained, indicating that either weak Brønsted acid sites have been formed that were unable to retain pyridine at 723 K or that dealumination sterically destabilized pyridine adsorption. Remarkably, also the EFAl-OH band at 3660 cm^{-1} decreased upon pyridine adsorption. Based on a detailed previous assignment [12],

we attribute it to be caused by hydrogen bonding with the aromatic ring of pyridine adsorbed at a SBAS (forming pyridinium ion) in close vicinity. In order to support this, we explored whether the EFAl-OH group itself (without SBAS in close proximity) interacts with pyridine. Thus, pyridine was adsorbed on Na-MFI-15(43%), as the Na^+ cations are known not to be able to stabilize adsorbed pyridine after outgassing at 723 K.

As SBAS in H-MFI-15(43%) were replaced by Na^+, the band corresponding to SBAS (3610 cm^{-1}) was absent (Figure 2.10A), while the EFAl-OH group band at 3660 cm^{-1} remained. The disappearance of the band at 3780 cm^{-1} is due to the replacement of the OH group in EFAl with a Na^+ [5, 34, 35]. Upon pyridine adsorption, no change was observed for the band at 3660 cm^{-1}, indicating that pyridine is not adsorbed on EFAl-OH (3660 cm^{-1}) in the sample without SBAS after outgassing at 723 K (see also the IR difference spectra recorded after pyridine adsorption with respect to that prior to pyridine adsorption in Figure 2.10B). In contrast, the IR difference spectra recorded with H-MFI-15(43%) distinctly showed that the EFAl-OH interacted with pyridine in the presence of SBAS with H-MFI-15(43%).

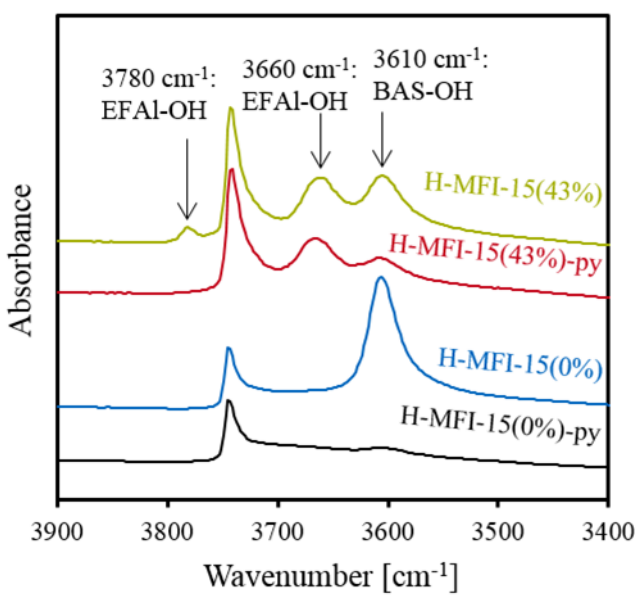

Figure 2.9. IR spectra of OH stretching vibration region of 3900 to 3400 cm^{-1} for H-MFI-15(0%) and H-MFI-15(43%) samples at 423K. H-MFI-15(0%)-py and H-MFI-15(43%)-py are the samples adsorbed with pyridine and later outgased at 723 K.

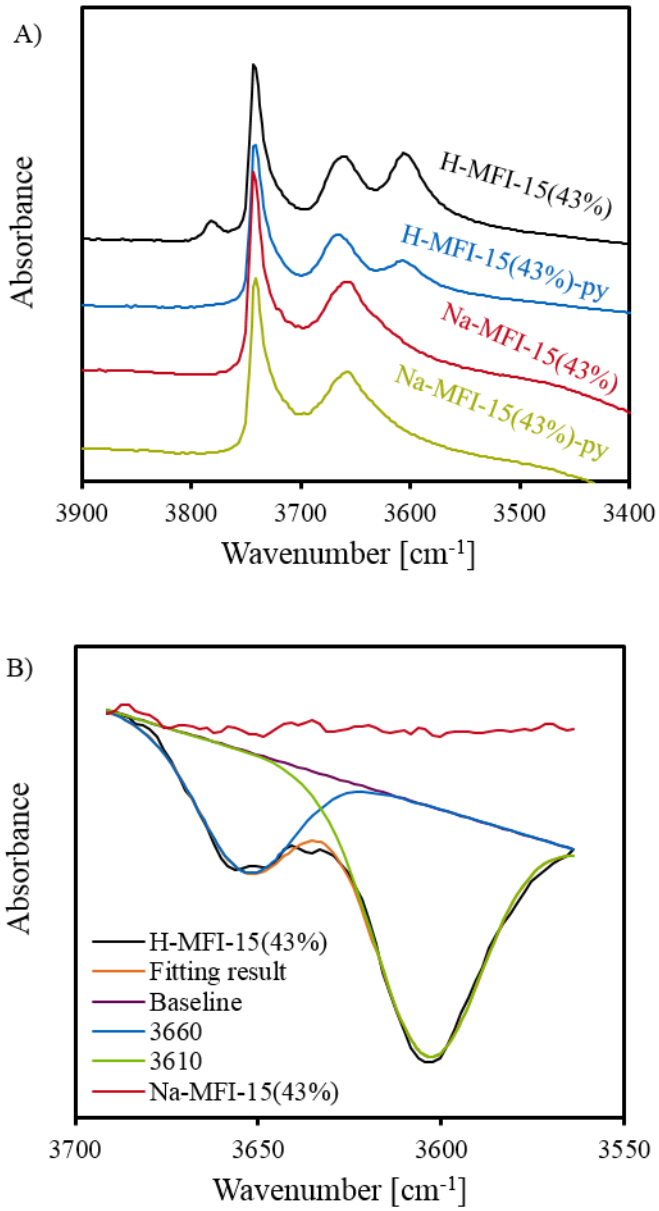

Figure 2.10. A) IR spectra of OH stretching vibration region of 3900 to 3400 cm^{-1} for H-MFI-15(43%) and Na-MFI-15(43%) samples at 423K. H-MFI-15(43%)-py and Na-MFI-15(43%)-py are the H-MFI-15(43%) and Na-MFI -15(43%) adsorbed with pyridine and later outgased at 723 K. B) IR difference spectra of OH stretching vibration region of 3700 to 3550 cm^{-1} for H-MFI(43%) and Na-MFI(43%) adsorbed with pyridine and later outgased at 723 K. The difference spectra were obtained by subtracting the spectra with adsorbed pyridine with the spectra prior to pyridine adsorption.

The observed changes in the IR bands upon pyridine adsorption allow quantification of the concentration of SBAS with adjacent EFAl (EFAl-SBAS) and isolated SBAS (I-SBAS) in H-MFI-15. When the sample adsorbs pyridine, only the pyridine adsorbed on EFAl-SBAS contributes to the negative band at 3660 cm^{-1} in Figure 2.10B. Therefore, the percentage of EFAl-SBAS in the total SBAS can be obtained by the following equation:

$$X_{\mathrm{EFAl-SBAS}} = \frac{Area_{3660}}{Area_{3610}} \times 100\% \quad (3)$$

in which $X_{\mathrm{EFAl\text{-}SBAS}}$ is the percentage of EFAl-SBAS in all the SBAS. $Area_{3660}$ *and* $Area_{3610}$ correspond to the decrease of the bands at 3660 and 3610 cm^{-1} of H-MFI-15 after exposure to pyridine and desorption at 723 K. It is noted in passing that two assumptions were used in this quantification: the stoichiometric ratio of EFAl to SBAS in EFAl-SBAS site is one to one and the molar extinction coefficient of hydroxyl group of EFAl at 3660 cm^{-1} is the same as that of the bridged hydroxyl group at 3610 cm^{-1}. The percentage and concentration of the EFAl-SBAS and I-SBAS in the H-MFI-15 samples are compiled in Table 2.1 and Table 2.2.

2.5. Evidence the EFAl decrease the SBAS strength

The acidity of EFAl-SBAS and I-SBAS is measured by temperature-programmed-desorption (TPD) of pyridine on H-MFI-15(0%) and H-MFI-15(43%) respectively, which is detected by IR spectra in Figure 2.11. Rate of pyridine desorption for 3610 cm^{-1} in H-MFI-15(0%) and 3660 cm^{-1} in H-MFI-15(43%) in IR with increasing temperatures (423-823K) is used to investigate the acid strength of I-SBAS and EFAl-SBAS respectively. Temperatures of pyridine desorption peaks are around 523-623K on EFAl-SBAS and the temperatures are approximately 623-723K on I-SBAS, which means that EFAl-SBAS has lower acidity than I-SBAS. In other words, EFAl formed from dealumination decrease the acid strength of adjacent SBAS.

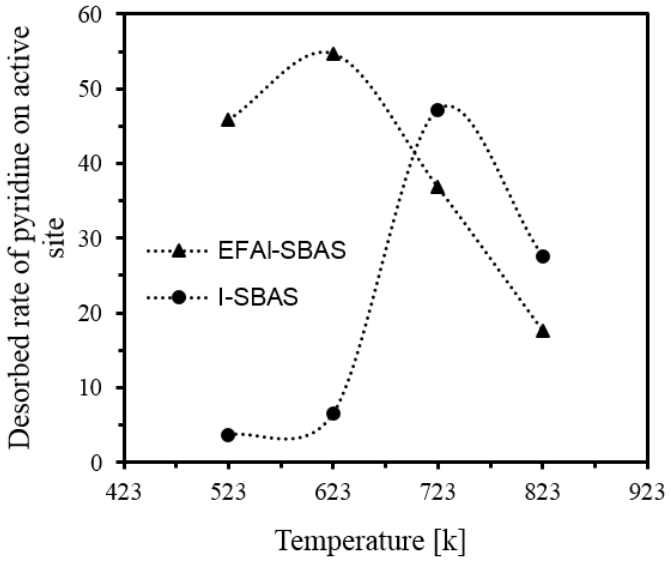

Figure 2.11. Desorbed pyridine rate on the EFAl-SBAS and I-SBAS at different temperatures of 423-823K.

2.6 Conclusions

EFAl generated in H-MFI by steaming with controlled temperature, water vapor pressure and duration forms a new active site (EFAl-SBAS), if it is in close proximity to SBAS. The NMR, IR, XANES and EXAFS techniques can evidence the creation of the EFAl species and decrease of the FAl species. However, dealumination of zeolite cannot change its micropore volume and structure. The close proximity of EFAl-SBAS were concluded unequivocally from the IR spectra of adsorbed pyridine. The percentage and concentration of EFAl-SBAS in H-MFI-15 samples can be quantified. The EFAl decreases the acid strength of the adjacent SBAS.

2.7 Contributions

The work in this chapter was under the supervision of Prof. Dr. Johannes A. Lercher, Dr. Yue Liu and Dr. Ricardo Bermejo-Deval. Yang Zhang contributed to the design of the experiments and operating setups and data analysis. Prof. Dr. Jianzhi Hu contributed with NMR measurements. Xaver Hecht contributed to nitrogen physisorption measurements. John L. Fulton contributed to the Al K–edge XANES and EXAFS measurements and related data analysis. Ruixue Zhao, Dr. Maricruz Sanchez-Sanchez and Prof. Dr. Gary L. Haller contributed for fruitful discussions.

2.8 References

[1] S.M. Babitz, B.A. Williams, J.T. Miller, R.Q. Snurr, W.O. Haag, H.H. Kung, Monomolecular cracking of n-hexane on Y, MOR, and ZSM-5 zeolites, *Applied Catalysis A:general*, 179 (**1999**) 71-86.

[2] L.H. Ong, M. Dömök, R. Olindo, A.C. van Veen, J.A. Lercher, Dealumination of HZSM-5 via steam-treatment, *MICROPOR MESOPOR MAT*, 164 (**2012**) 9-20.

[3] Y. Chu, B. Han, A. Zheng, F. Deng, Influence of Acid Strength and Confinement Effect on the Ethylene Dimerization Reaction over Solid Acid Catalysts: A Theoretical Calculation Study, *The Journal of Physical Chemistry C*, 116 (**2012**) 12687-12695.

[4] W.O. Haag, R.M. Dessau, R.M. Lago, Kinetics and Mechanism of Paraffin Cracking with Zeolite Catalysts, in: T. lnui, S. Namba, T. Tatsumi (Eds.) *Studies in Surface Science and Catalysis*, Elsevier, **1991**, pp. 255-265.

[5] S.M. Maier, A. Jentys, J.A. Lercher, Steaming of Zeolite BEA and Its Effect on Acidity: A Comparative NMR and IR Spectroscopic Study, *The Journal of Physical Chemistry C*, 115 (**2011**) 8005-8013.

[6] S. Li, A. Zheng, Y. Su, H. Zhang, L. Chen, J. Yang, C. Ye, F. Deng, Brønsted/Lewis Acid Synergy in Dealuminated HY Zeolite: A Combined Solid-State NMR and Theoretical Calculation Study, *Journal of the American Chemical Society*, 129 (**2007**) 11161-11171.

[7] Q.L. Wang, G. Giannetto, M. Guisnet, Dealumination of zeolites III. Effect of extra-framework aluminum species on the activity, selectivity, and stability of Y zeolites in n-heptane cracking, *Journal of Catalysis*, 130 (**1991**) 471-482.

[8] K.A. Tarach, J. Martinez-Triguero, F. Rey, K. Góra-Marek, Hydrothermal stability and catalytic performance of desilicated highly siliceous zeolites ZSM-5, *Journal of Catalysis*, 339 (**2016**) 256-269.

[9] T. Masuda, Y. Fujikata, S.R. Mukai, K. Hashimoto, Changes in catalytic activity of MFI-type zeolites caused by dealumination in a steam atmosphere, *Applied Catalysis A:general*, 172 (**1998**) 73-83.

[10] C.S. Triantafillidis, N.P. Evmiridis, L. Nalbandian, I.A. Vasalos, Performance of ZSM-5 as a Fluid Catalytic Cracking Catalyst Additive: Effect of the Total Number of Acid Sites and Particle Size, *Industrial & Engineering Chemistry Research*, 38 (**1999**) 916-927.

[11] D.P. Ivanov, L.V. Pirutko, G.I. Panov, Effect of steaming on the catalytic performance of ZSM-5 zeolite in the selective oxidation of phenol by nitrous oxide, *Journal of Catalysis*, 311 (**2014**) 424-432.

[12] S. Schallmoser, T. Ikuno, M.F. Wagenhofer, R. Kolvenbach, G.L. Haller, M. Sanchez-Sanchez, J.A. Lercher, Impact of the local environment of Brønsted acid sites in ZSM-5 on the catalytic activity in n-pentane cracking, *Journal of Catalysis*, 316 (**2014**) 93-102.

[13] E. Loeffler, U. Lohse, C. Peuker, G. Oehlmann, L.M. Kustov, V.L. Zholobenko, V.B. Kazansky, Study of different states of nonframework aluminum in hydrothermally dealuminated HZSM-5 zeolites using diffuse reflectance i.r. spectroscopy, *Zeolites*, 10 (**1990**) 266-271.

[14] M. Maache, A. Janin, J.C. Lavalley, J.F. Joly, E. Benazzi, Acidity of zeolites Beta dealuminated by acid leaching: An FTi.r. study using different probe molecules (pyridine, carbon monoxide), *Zeolites*, 13 (**1993**) 419-426.

[15] J.P. Marques, I. Gener, P. Ayrault, J.C. Bordado, J.M. Lopes, F. Ramôa Ribeiro, M. Guisnet, Infrared spectroscopic study of the acid properties of dealuminated BEA zeolites, *MICROPOR MESOPOR MAT*, 60 (**2003**) 251-262.

[16] H. Krannila, W.O. Haag, B.C. Gates, Monomolecular and bimolecular mechanisms of paraffin cracking: n-butane cracking catalyzed by HZSM-5, *Journal of Catalysis*, 135 (**1992**) 115-124.

[17] C. Martineau-Corcos, J. Dědeček, F. Taulelle, 27Al-27Al double-quantum single-quantum MAS NMR: Applications to the structural characterization of microporous materials, *Solid State Nuclear Magnetic Resonance*, 84 (**2017**) 65-72.

[18] N. Xue, A. Vjunov, S. Schallmoser, J.L. Fulton, M. Sanchez-Sanchez, J.Z. Hu, D. Mei, J.A. Lercher, Hydrolysis of zeolite framework aluminum and its impact on acid catalyzed alkane reactions, *Journal of Catalysis*, 365 (**2018**) 359-366.

[19] R. Gounder, E. Iglesia, Catalytic Consequences of Spatial Constraints and Acid Site Location for Monomolecular Alkane Activation on Zeolites, *Journal of the American Chemical Society*, 131 (**2009**) 1958-1971.

[20] C.A. Emeis, Determination of Integrated Molar Extinction Coefficients for Infrared Absorption Bands of Pyridine Adsorbed on Solid Acid Catalysts, *Journal of Catalysis*, 141 (**1993**) 347-354.

[21] A. Vjunov, J.L. Fulton, T. Huthwelker, S. Pin, D. Mei, G.K. Schenter, N. Govind, D.M. Camaioni, J.Z. Hu, J.A. Lercher, Quantitatively Probing the Al Distribution in Zeolites, *Journal of the American Chemical Society*, 136 (**2014**) 8296-8306.

[22] B. Ravel, M. Newville, ATHENA, ARTEMIS, HEPHAESTUS: data analysis for X-ray absorption spectroscopy using IFEFFIT, *Journal of Synchrotron Radiation*, 12 (**2005**) 537-541.

[23] M. Newville, IFEFFIT : interactive XAFS analysis and FEFF fitting, *Journal of Synchrotron Radiation*, 8 (**2001**) 322-324.

[24] J.L. Fulton, M. Balasubramanian, Structure of Hydronium (H3O+)/Chloride (Cl−) Contact Ion Pairs in Aqueous Hydrochloric Acid Solution: A Zundel-like Local Configuration, *Journal of the American Chemical Society*, 132 (**2010**) 12597-12604.

[25] X. Li, W. Zhang, K. Liu, X. Han, L. Xu, X. Bao, A high-resolution MAS NMR study on the potential catalysts Mo/HBeta for olefin metathesis: The interaction of Mo species with HBeta zeolite, **2006**.

[26] E. Brunner, H. Ernst, D. Freude, T. Frohlich, M. Hunger, H. Pfeifer, Magic-Angle-Spinning Nmr-Studies of Acid Sites in Zeolite H-Zsm-5, *Journal of Catalysis*, 127 (**1991**) 34-41.

[27] G.L. Woolery, G.H. Kuehl, H.C. Timken, A.W. Chester, J.C. Vartuli, On the nature of framework Brønsted and Lewis acid sites in ZSM-5, *Zeolites*, 19 (**1997**) 288-296.

[28] D.C. Koningsberger, J.T. Miller, The development of strong acidity by non-framework aluminum in H-USY determined by Al XAFS spectroscopy, *Studies in Surface Science and Catalysis*, 101 (**1996**) 841-850.

[29] J. Rocha, J. Klinowski, 27Al Solid-state NMR spectra of ultrastable zeolite Y with fast magic-angle spinning and 1H–27Al cross-polarization, *Journal of the Chemical Society, Chemical Communications*, (**1991**) 1121-1122.

[30] J.-P. Gilson, G.C. Edwards, A.W. Peters, K. Rajagopalan, R.F. Wormsbecher, T.G. Roberie, M.P. Shatlock, Penta-co-ordinated aluminium in zeolites and aluminosilicates, *Journal of the Chemical Society, Chemical Communications*, (**1987**) 91-92.

[31] C.W. Childs, S. Hayashi, R.H. Newman, Five-coordinate aluminum in allophane, *Clays and Clay Minerals*, 47 (**1999**) 64-69.

[32] J.A. van Bokhoven, A.M.J. van der Eerden, D.C. Koningsberger, Three-Coordinate Aluminum in Zeolites Observed with In situ X-ray Absorption Near-Edge Spectroscopy at the Al K-Edge: Flexibility of Aluminum Coordinations in Zeolites, *Journal of the American Chemical Society*, 125 (**2003**) 7435-7442.

[33] H. Knözinger, P. Ratnasamy, Catalytic Aluminas: Surface Models and Characterization of Surface Sites, *Catalysis Reviews*, 17 (**1978**) 31-70.

[34] A. Janda, A.T. Bell, Effects of Si/Al Ratio on the Distribution of Framework Al and on the Rates of Alkane Monomolecular Cracking and Dehydrogenation in H-MFI, *Journal of the American Chemical Society*, 135 (**2013**) 19193-19207.

[35] M.R. Gonzalez, S.B. Sharma, D.T. Chen, J.A. Dumesic, Thermogravimetric and microcalorimetric studies of ZSM-5 acidity, *Catalysis Letters*, 18 (**1993**) 183-192.

Supporting information

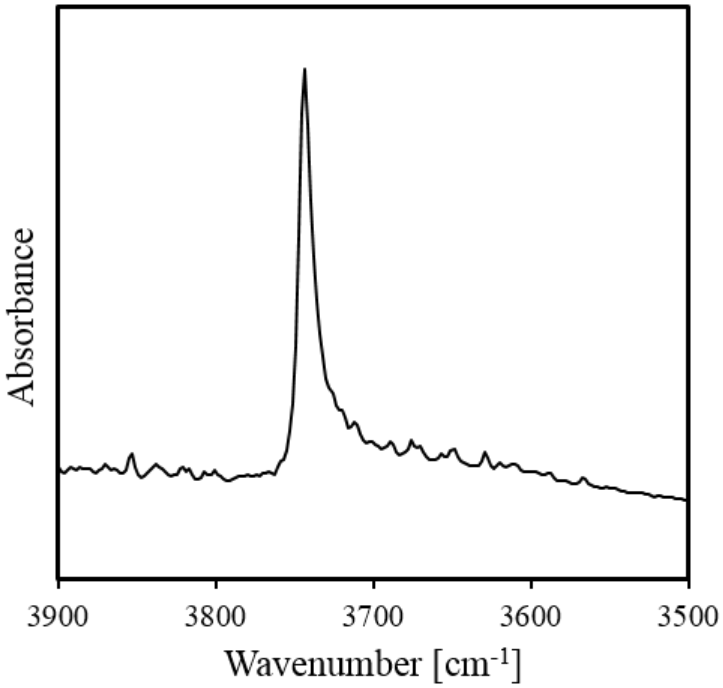

Supplementary Figure 2.1. IR spectra of OH stretching vibration region of 3900 to 3500 cm^{-1} for H-MFI-15 steam at 10 kPa and 1023 K for 4 h.

The hydroxyl group of BAS at 3610 cm^{-1} and hydroxyl groups of EFAl at 3660 and 3780 cm^{-1} were disappeared after H-MFI-15 steamed at 10 kPa and 1023 K for 4 h. It means that the Al framework structure can be completely damaged and the EFAl can be completely diffused out of the zeolite.

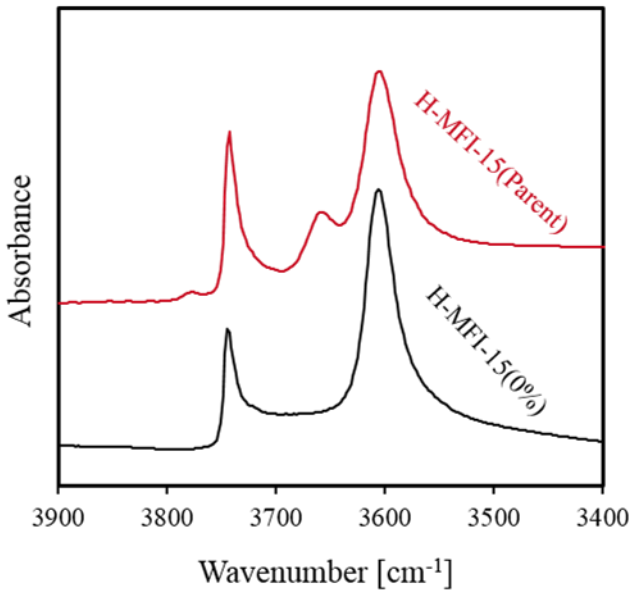

Supplementary Figure 2.2. IR spectra of OH stretching vibration region of 3900 to 3400 cm^{-1} for H-MFI-15(Parent) and H-MFI-15(0%) samples.

Chapter 3

Promotion of protolytic pentane conversion on H-MFI zeolite by proximity of extra-framework aluminum oxide and Brønsted acid sites

This chapter is based on:

Yang Zhang, Ruixue Zhao, Maricruz Sanchez-Sanchez, Gary L. Haller, Jianzhi Hu, Ricardo Bermejo-Deval*, Yue Liu* and Johannes A. Lercher*, "Promotion of protolytic pentane conversion on H-MFI zeolite by proximity of extra-framework aluminum oxide and Brønsted acid sites" accepted by J. Catal. 2018.

ABSTRACT: The activity of strong Brønsted acid sites in H-MFI zeolites for pentane cracking and dehydrogenation is enhanced by the presence of extra-framework aluminum oxide in spatial proximity. The turnover frequencies of overall cracking and dehydrogenation on such sites are about 50 and 80 times higher than on isolated strong Brønsted acid sites. While pentane does not adsorb stronger, the site pair stabilizes cracking and dehydrogenation transition states mainly via increasing entropy. This is interpreted as a later transition state for the cracking and dehydrogenation. The results suggest that controlled steaming can be used to enhance catalytic activity of zeolite Brønsted acid sites.

3.1. Introduction

Strong Brønsted acid sites (SBAS) formed by charge-balancing tetrahedrally-coordinated aluminum atoms (Al^{3+}) in the zeolite (bridging OH in SiOHAl) are the active centers for the conversions of hydrocarbons in cracking, isomerization and alkylation reactions [1-4]. In monomolecular protolytic cracking of alkane, the proton in the SBAS can protonate alkane molecules to form penta-coordinated carbonium ion and then it cracks into a carbenium ion and a smaller alkane. The carbeium ion will form an alkene and free SBAS is formed again. For example, the proton attacks carbon in the propane molecule and protonates carbon-carbon and then carbon-hydrogen sigma bonds (three-center two electrons bond) are formed, which is called carbonium ion. And then the propane carbonium ion cracks into 33% CH_4 + C_2H_4 molecule and 67% C_3H_6 + H_2 molecule (Figure 3.1) [5].

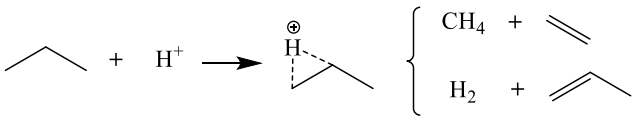

Figure 3.1. Penta-coordinated carbonium ion on solid acidic catalyst in propane cracking.

The energy profile for monomolecular pentane cracking in the H-MFI zeolite can be displayed in the Figure 3.2. Gaseous pentane in the ground state (C_5H_{12}(g)) is adsorbed on the Brønsted acid sites (BAS) of zeolite to form adsorbed ground state pentane(C_5H_{12}(z)), the adsorbed ground state pentane cross carbonium ion transition state ($CH_3\cdots H^+\cdots\cdots C_4H_9\cdots$Si-O-Al$^-$)‡ and the products (such as CH_4+C_4H_8) are formed.

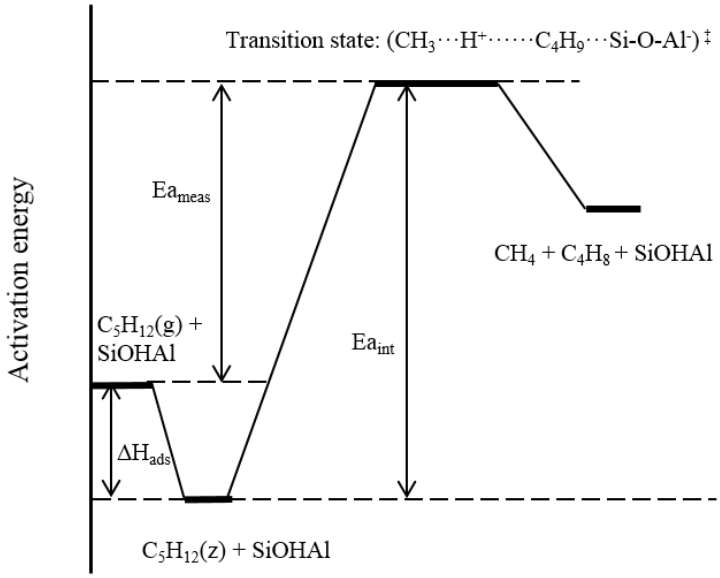

Figure 3.2. The diagram of activation energy for C_1+$C_4^=$ cracking pathway of pentane on the BAS of zeolite.

Bhan et al. [6] proposed that the increased activity in overall cracking and dehydrogenation of alkanes with carbon numbers was not due to the higher physisorbed alkanes concentration in the zeolite channels, but due to the intrinsic activation entropy as the intrinsic activation energy are constant with the carbon numbers. Gounder et al. [7] mentioned that the propane and butane cracking and dehydrogenation activity in the 8 MR side pocket was higher than that in the 12 MR main channel of H-Mordenite. As the similar intrinsic activation energy were assumed in the two types of MR, the higher intrinsic entropy in the confined 8 MR with respect to the 12 MR, leaded to the former with higher reaction rate. Bell et al. [8] found that the BAS in the channels intersection of H-MFI had higher activity than the BAS in the straight and sinusoidal channels in butane monomolecular cracking and dehydrogenation. The intrinsic activation energy of butane cracking and dehydrogenation in the straight and sinusoidal channels were higher than that on the channels intersection of H-MFI. However, the higher intrinsic activation entropy were observed in the channels intersection, which compensated the intrinsic activation energy and leaded to the higher activation activity in the channels intersection.

EFAl created at mild steaming conditions has been reported to have promotional effect on the alkane cracking activity [9-12]. These findings agree well with our previous findings that two types of SBAS coexist, i.e., SBAS in close proximity to EFAl (EFAl-SBAS) and isolated SBAS which has no EFAl in close proximity (I-SBAS) [11, 13]. It is hypothesized that stabilization

of a later transition state would entropically facilitate C-C and C-H bond cleavage [11]. It has been shown recently that the EFAl generated under short steaming time increases the turnover frequency (TOF) of monomolecular cracking and dehydrogenation of n-butane, while prolonged steaming time leads to octahedrally EFAl with similar TOF [13].

As these studies had a too limited span of intrinsic kinetic data on I-SBAS and EFAl-SBAS, a series of H-MFI zeolites with different percentage of these sites were synthesized and characterized. Catalytic cracking of pentane is used to analyze in detail the impact of different concentrations of these two sites.

3.2 Experimental

3.2.1 *IR spectroscopy of adsorption of pentane*

IR spectra of adsorption of pentane were carried on Bruker vertex 70. The sample wafers were activated in vacuum at 723 K for 1 h before adsorption of pentane. Pentane was dosed into the samples at 343 K until all the acid sites were adsorbed saturation from 0.002 to 0.85 mbar pressure. The coverage of BAS at certain pentane pressure was used to attain the adsorption isotherm of pentane on H-MFI, which is calculated by the decrease of the area of the bridge OH vibrational bands at 3610 cm^{-1} in the IR spectra. Equation (1) was used to calculate the adsorption constant of pentane on BAS by adsorption isotherm regression following the Langmuir adsorption model.

$$n = \frac{n_{\mathrm{m}} K^{\circ}_{\mathrm{ads}} p}{1 + K^{\circ}_{\mathrm{ads}} p} \tag{1}$$

Where p is partial pressure of pentane(normalized to 1013 mbar), n_{m} and n are maximum uptake of pentane and pentane uptake at each partial pressure on the BAS of H-MFI zeolite and K°_{ads} is the standard state adsorption equilibrium constant of pentane on H-MFI zeolite.

Equation (2) was employed to calculate the adsorption entropy of pentane on H-MFI zeolite.

$$\Delta S^{\circ}_{\mathrm{ads}} = \frac{\Delta H^{\circ}_{\mathrm{ads}}}{T} + R\ln(K^{\circ}_{\mathrm{ads}}) \tag{2}$$

in which, $\Delta H^{\circ}_{\mathrm{ads}}$ and $\Delta S^{\circ}_{\mathrm{ads}}$ are standard adsorption enthalpy and entropy of pentane on H-MFI zeolite , and T is the adsorption temperature and R is the universal gas constant.

3.2.2 *Adsorption heat of pentane*

A modified calorimeter SETARAM TG-DSC 111 connected to a high vacuum system was performed for the gravimetric and calorimetric measurements. 20 mg sieved samples (250-315 μm particle size) were activated in vacuum at 723 K for 1 h with 10 K min^{-1} heating rate. Pentane was dosed to the equipment at 343 K from 0.02 mbar to 2 mbar until sample mass, heat flow and pressure became constant. The released heat was attained by integration of the observed heat flux signal and the adsorbed pentane amount was derived from the mass difference between different pentane pressures. Therefore, the adsorption heat of pentane on the H-MFI zeolite was calculated by the quotient between the released heat and the adsorbed mass of pentane.

3.2.3 Kinetic measurements

Reaction of n-pentane was performed in a fixed bed reactor. A tubular quartz reactor with an inner diameter of 6 mm and a length of 280 mm was used. All catalysts were pressed, crushed and sieved to 250-315 μm particle fraction and loaded into the reactor. The catalysts were activated at 803 K for 2 h with a heating rate of 2 K min^{-1} in synthetic air with a flow rate of 30 ml min^{-1}. The reactor was then flushed for 30 min with N_2 (100 ml min^{-1}). Liquid pentane was transferred to the gas phase via an evaporator and transported to the reactor with N_2. The reaction conditions of low catalyst loading, low pentane partial pressure (21 mbar) and high temperatures were used, in order to ensure that all the samples follow a monomolecular cracking and dehydrogenation pathway [3, 14, 15]. Specifically, the reaction was carried out at temperatures between 753 and 793 K with 1 bar total pressure; the catalyst amount was varied to maintain conversions below 2%. The products were analyzed by an on-line gas chromatograph with a flame ionization detector. Initial rates were normalized to catalyst amount (Supplementary Figure 3.1) and turnover frequency (TOF) was normalized to SBAS concentration of formation of products, which were used to evaluate the catalyst activity.

3.3 Results

3.3.1 Adsorption properties of pentane on I-SBAS and EFAl-SBAS in H-MFI-15

As adsorption enthalpy and entropy hardly change with reaction temperatures [16], the thermodynamic properties of n-pentane adsorption were determined at 343 K [7, 11, 17]. The distribution of sites was hypothesized to be constant with varying temperatures.

The IR spectra of H-MFI-15(0%) and H-MFI-15(43%) during pentane adsorption are shown in supplementary Figure 3.2 and the IR difference spectra of H-MFI-15(0%) and H-MFI-15(43%) after pentane adsorption with respect to before pentane adsorption are displayed in Figure 3.3. On H-MFI-15(0%), the intensity of the BAS-OH band at 3610 cm^{-1} decreased with the increase of pentane pressure. Concurrently, a new broad band was observed at 3489 cm^{-1}, corresponding to the perturbed hydrogen bonded SiOHAl group by adsorbed pentane [18, 19]. These changes were also observed in H-MFI-15(43%). In addition, the intensity of EFAl-OH band at 3660 cm^{-1} decreased and a second perturbed OH band appeared at 3563 cm^{-1}. These two changes are attributed to the interaction between pentane and the hydroxyl group of EFAl. These results indicate that pentane adsorbed on EFAl-SBAS interacts with both EFAl-OH and BAS-OH. The red-shift (~97 cm^{-1}) of the perturbed EFAl-OH group was smaller than that (~121 cm^{-1}) of the perturbed BAS-OH band, indicating a lower acid strength of the EFAl-OH group compared to BAS.

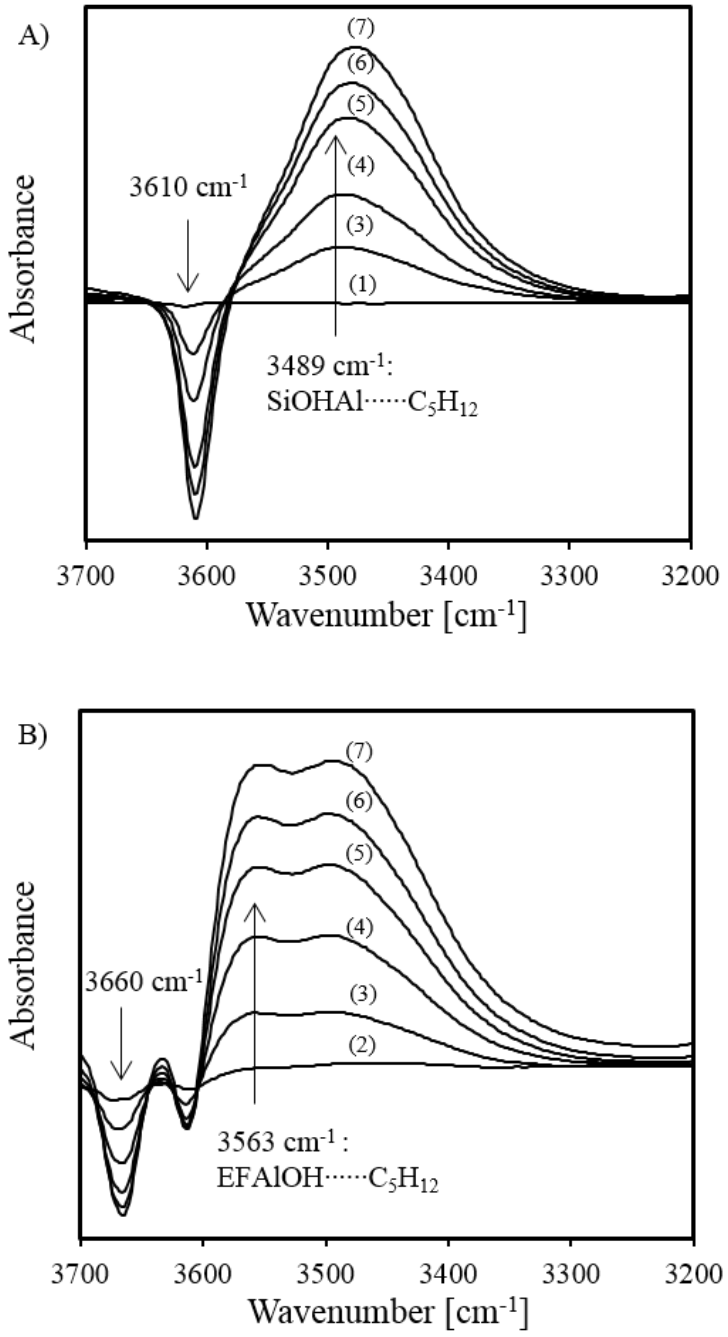

Figure 3.3. IR difference spectra of OH stretching vibration region of 3700 to 3200 cm^{-1} for A) H-MFI-15(0%) and B) H-MFI-15(43%) between the adsorption spectrum measured after pentane being adsorbed at different equilibrium pressures of 0.002 (1), 0.01 (2), 0.05 (3), 0.12 (4), 0.25 (5), 0.44 (6), and 0.85 (7) mbar and the spectrum for the 343 K treated sample. The lines indicate an increasing loss (negative) or gain (positive) in intensity of the IR bands with increasing pentane pressures from 0.002 to 0.85 mbar.

The adsorption isotherm of pentane on H-MFI-15(0%) and H-MFI-15(43%) was derived from the decrease of BAS-OH band (3610 cm^{-1}) in the IR spectra (Figure 3.4). Pentane was adsorbed

on BAS with 1:1 stoichiometry in H-MFI-15 up to 30% BAS-OH coverage (Supplementary Figure 3.3) [19]. Above 30% coverage more pentane was adsorbed per BAS, leading to a red-shift in the perturbed OH band (Figure 3.3 and supplementary Figure 3.4). This was both observed in H-MFI-15(0%) and H-MFI-15(43%). Therefore, adsorption isotherms were plotted in the coverage range of 0 – 30% (Figure 3.4). By regression of the isotherm with Langmuir adsorption equation (Equation 1), the adsorption constant of pentane on H-MFI-15(0%) and H-MFI-15(43%) are (6.5 ± 0.2) $\times 10^3$ and (6.6 ± 0.1) $\times 10^3$, respectively. These two close values indicate that the pentane adsorption constants on I-SBAS and EFAl-SBAS are both (6.5 ± 0.2) $\times 10^3$. This is also supported by the proportional decrease of band intensity of BAS-OH (3610 cm^{-1}) and EFAl-OH (3660 cm^{-1}) (Supplementary Figure 3.5).

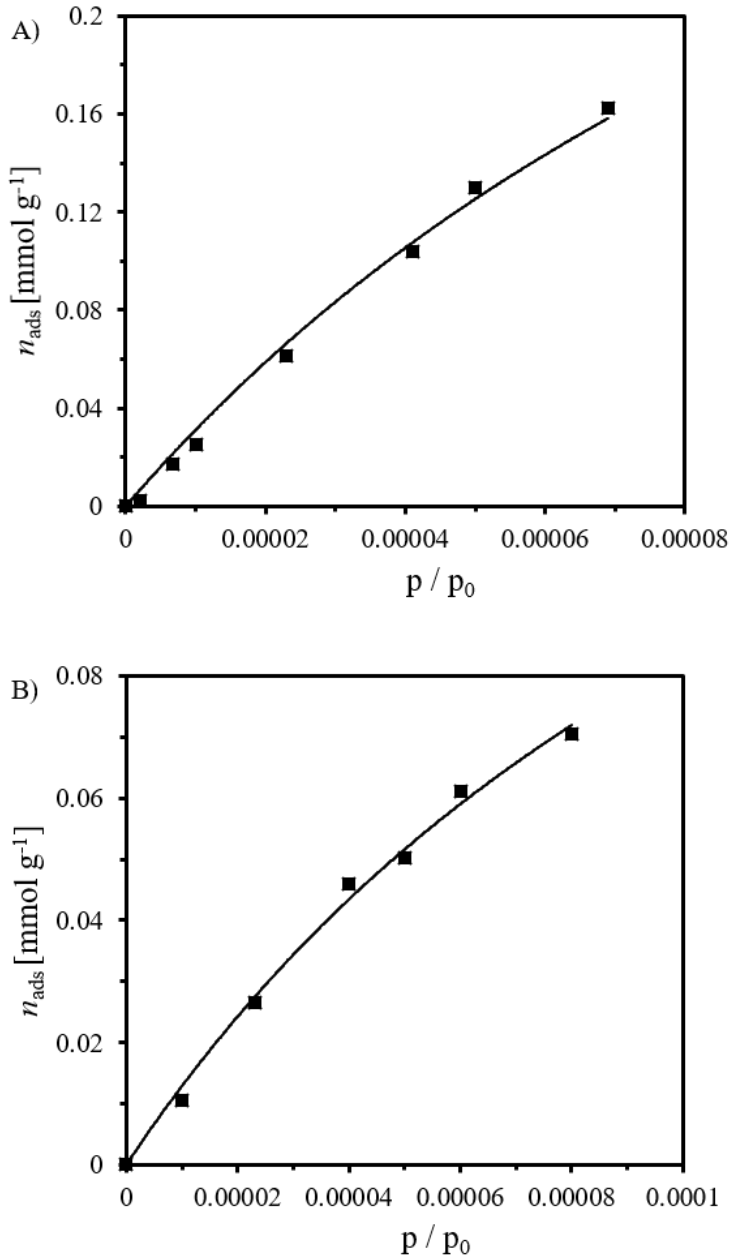

Figure 3.4. Adsorption isotherm of pentane measured from the decrease of the 3610 cm^{-1} OH band in the IR spectra of A) H-MFI-15(0%) and B) H-MFI-15(43%) samples during pentane adsorption up to 30% coverage at 343 K.

Figure 3.5 shows the calorimetrically measured adsorption heat of pentane on H-MFI-15(0%) and H-MFI-15(43%) as a function of pentane uptake. In the whole uptake range (0-0.78 mmol g^{-1}), the adsorption heat was identical for H-MFI-15(0%) and H-MFI-15(43%), being 64 ± 2 and 65 ± 2 kJ mol^{-1} respectively, in line with those reported in the literatures [11, 20-23]. Therefore, adsorption enthalpies of pentane on I-SBAS and EFAl-SBAS in H-MFI-15 samples are suggested to be same, -64 ± 2 kJ mol^{-1} (Table 3.1). With the obtained adsorption constants, the adsorption entropies on the two sites were -114 ± 6 J mol^{-1} K^{-1} (Table 3.1). Accounting the

error bar, it is concluded that the adsorption enthalpy and entropy of pentane on the I-SBAS and EFAl-SBAS sites are the same.

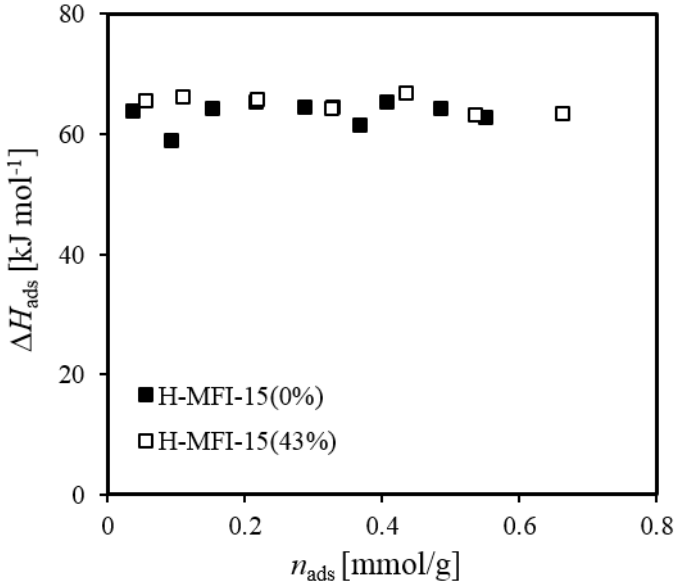

Figure 3.5. Adsorption heat as function of adsorbed pentane amount for H-MFI-15(0%) and H-MFI-15(43%).

Table 3.1. The adsorption constant, enthalpy and entropy of pentane on I-SBAS and EFAl-SBAS in H-MFI-15 samples.

Adsorption site	K°_{ads} (343 K)	ΔG°_{ads} (343K)	ΔH°_{ads}	ΔS°_{ads}
	× 10^3	[kJ mol^{-1}]	[kJ mol^{-1}]	[J mol^{-1}K^{-1}]
I-SBAS	6.5 ± 0.2	-25 ± 1	-64 ± 2	-114 ± 6
EFAl-SBAS	6.6 ± 0.1	-25 ± 1	-65 ± 2	-116 ± 4

3.3.2 Reaction of pentane on I- and EFAl-SBAS in H-MFI-15

Scheme 3.1 shows the four reaction pathways for the protolytic cracking of pentane to methane + butene (C_1+$C_4^=$), ethane + propene (C_2+$C_3^=$), propane + ethene (C_3+$C_2^=$) and pentene + H_2 (dehydrogenation), respectively.

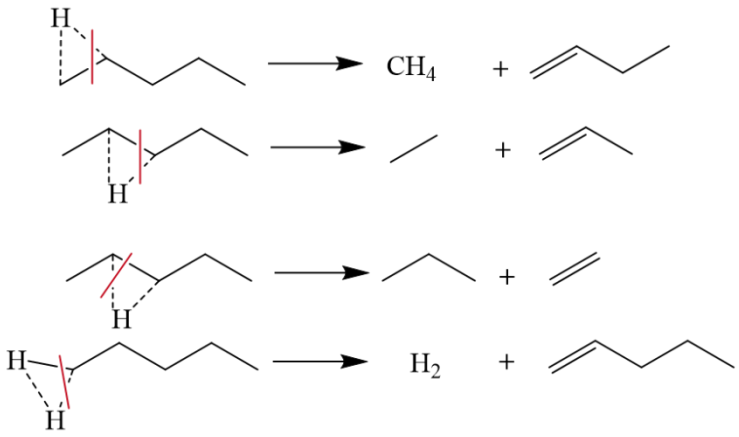

Scheme 3.1. Cracking and dehydrogenation pathways of protolytic cracking of n-pentane. Red line indicates location of the bond scission. Dotted line represents the SBAS proton coordinated with C or H in pentane as penta-coordinated carbonium ion in transition state.

Figure 3.6 shows the TOF for the overall cracking and dehydrogenation pathways at 793 K as a function of EFAl-SBAS percentage in the H-MFI-15 samples (Supplementary Table 3.1, the dependence of the weight normalized rate on the concentration of I-SBAS is depicted in Figure 3.7). The TOF increased linearly with the percentage of EFAl-SBAS. This is justified by equations (3-5). The H-MFI-15 weight normalized rate is contributed by the rate both on I-SBAS and EFAl-SBAS (Equation (3) and (4)).

$$Rate = TOF_{\text{I-SBAS}} \cdot [\text{I-SBAS}] + TOF_{\text{EFAl-SBAS}} \cdot [\text{EFAl-SBAS}] \quad (3)$$

$$TOF = \frac{Rate}{[\text{SBAS}]} = TOF_{\text{I-SBAS}} \cdot \frac{[\text{I-SBAS}]}{[\text{SBAS}]} + TOF_{\text{EFAl-SBAS}} \cdot \frac{[\text{EFAl-SBAS}]}{[\text{SBAS}]} \quad (4)$$

In which, [I-SBAS] and [EFAl-SBAS] are the concentration of I-SBAS and EFAl-SBAS in the H-MFI-15 samples.

By noting that the quotient of [EFAl-SBAS]/[SBAS] is actually the fraction of EFAl-SBAS ($X_{\text{EFAl-SBAS}}$), and that of [I-SBAS]/[SBAS] is 1- $X_{\text{EFAl-SBAS}}$, equation 4 becomes equation 5.

$$TOF = TOF_{\text{I-SBAS}} + (TOF_{\text{EFAl-SBAS}} - TOF_{\text{I-SBAS}}) \cdot X_{\text{EFAl-SBAS}} \quad (5)$$

Equation 5 shows that the apparent TOF has a linear correlation with the fraction of EFAl-SBAS. The linear increasing trend was also observed in each individual cracking pathway (Figure 3.8), showing that the EFAl-SBAS has a higher activity than I-SBAS.

This linear correlation between pentane conversion TOF at 763 K and the fraction of EFAl-SBAS was also found in H-MFI-40(0%) and steamed samples from H-MFI-40(0%), H-MFI-15(0%), and H-MFI-15 static calcination sample [11] (Figure 3.9 and supplementary Table 3.2). It means that the EFAl-SBAS in the parent H-MFI zeolite is same as that created from steaming treatment. It also encourages us to predict that the same EFAl-SBAS site can be created by different Si/Al ratio H-MFI zeolite and different dealumination methods.

By extrapolating to 100% EFAl-SBAS in Figure 3.6 and 3.8, the TOF of EFAl-SBAS in each reaction pathway was obtained. For example, the TOF of $C_1+C_4^=$ on EFAl-SBAS is $(26.3 \pm 1.5) \times 10^{-3}$ s^{-1}. Other TOFs are compiled in Table 3.2. It is clearly seen that the activity of EFAl-SBAS is about 50-times higher than that of I-SBAS at 793 K for the cracking pathways and 84 times higher for the dehydrogenation pathway.

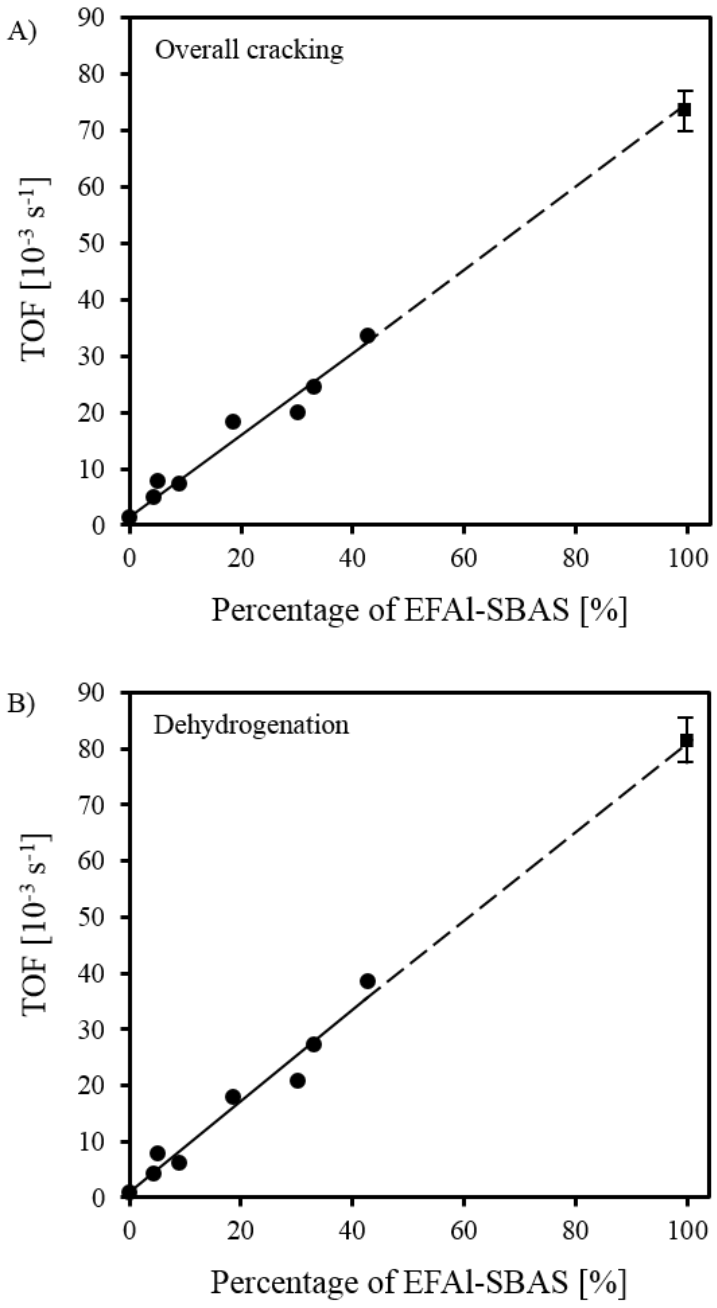

Figure 3.6. TOF of overall cracking A) and dehydrogenation B) of pentane as a function of EFAl-SBAS percentage on the H-MFI-15 samples (pentane 21 mbar, 793 K). Experimentally measured TOF (●); extrapolated TOF to 100% EFAl-SBAS (■).

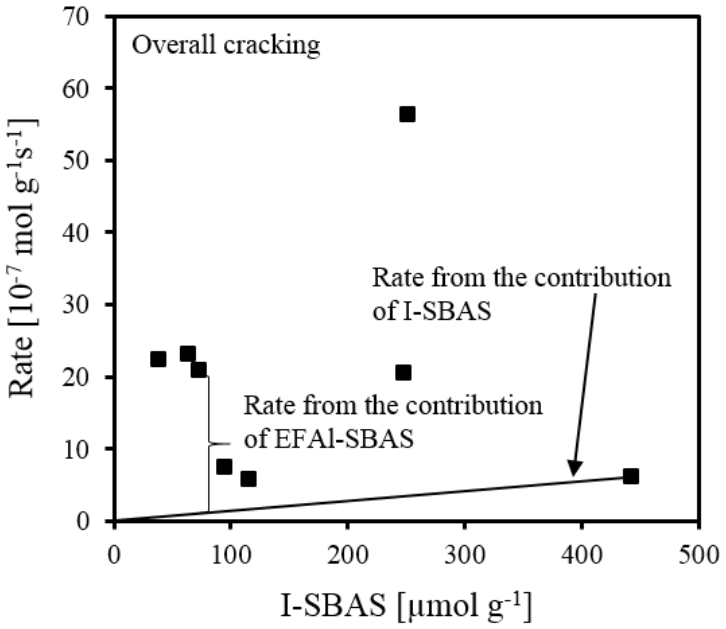

Figure 3.7. Cracking rate of pentane as function of concentration of I-SBAS in H-MFI-15 samples. The linear line indicates the theoretical rate contributed by I-SBAS. It is crossing the H-MFI-15(0%), but below all the others. The gap between the line and the real rate (■) is the part contributed by EFAl-SBAS.

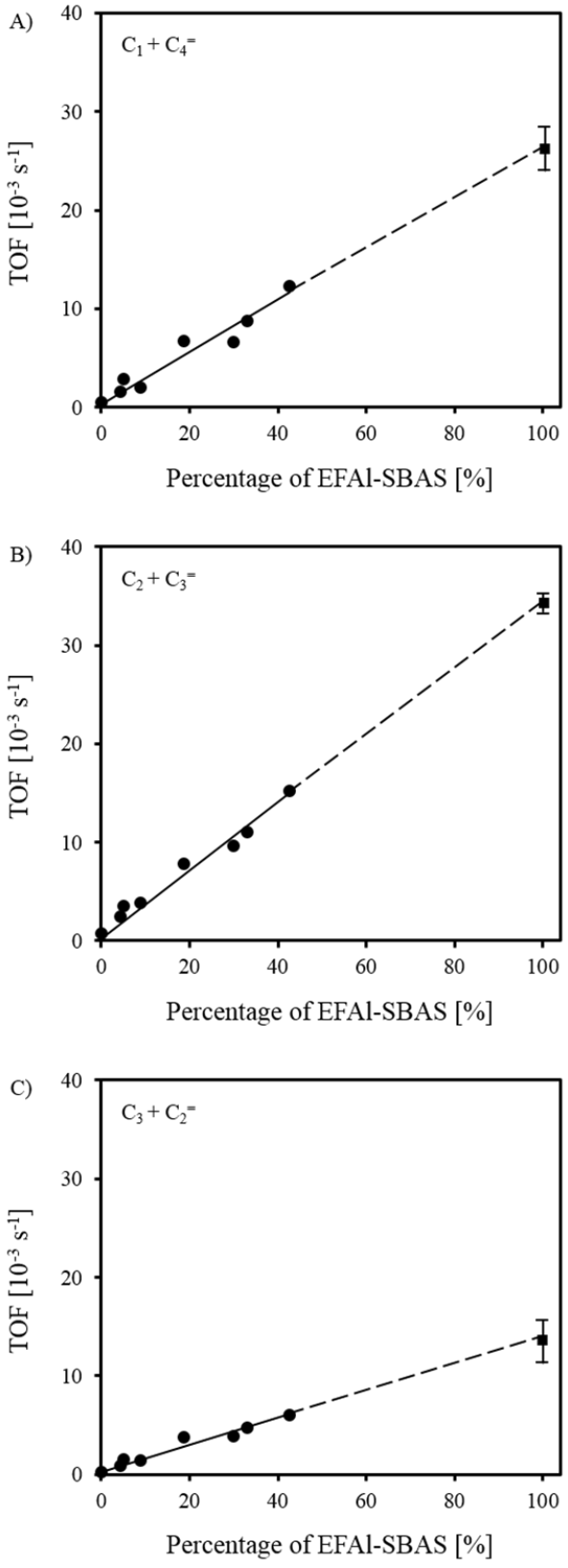

Figure 3.8. TOF of $C_1+C_4^=$ cracking pathway A), $C_2+C_3^=$ cracking pathway B), and $C_3+C_2^=$ cracking pathway C) of pentane as a function of EFAl-SBAS percentage in the H-MFI-15 sample (pentane 21 mbar, 793 K). Experimentally measured TOF (●); extrapolated TOF to 100% EFAl-SBAS (■).

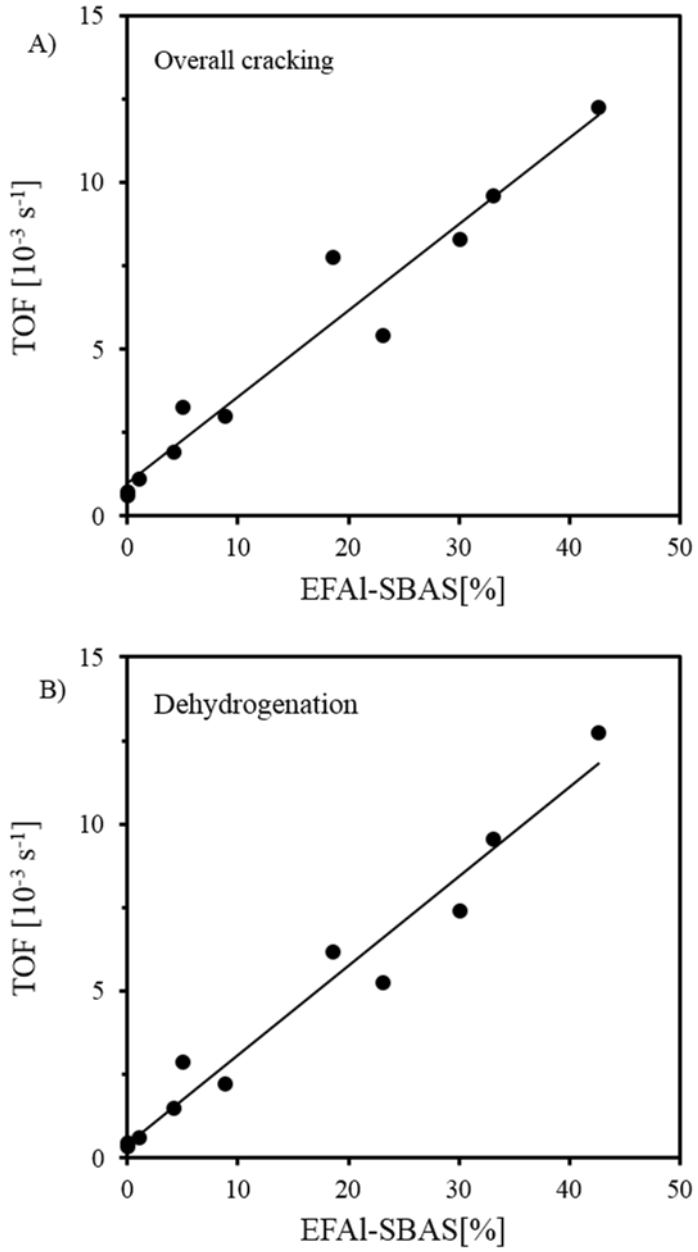

Figure 3.9. TOF of overall cracking A) and dehydrogenation B) of pentane as a function of EFAl-SBAS percentage on the H-MFI samples (pentane 21 mbar, 763 K).

Table 3.2. TOF of pentane cracking and dehydrogenation on I-SBAS and EFAl-SBAS in H-MFI-15 samples (793 K).

Active site	TOF, [10^{-3} s^{-1}]					
	$C_1+C_4^=$	$C_2+C_3^=$	$C_3+C_2^=$	overall[a]	dehyd.[b]	crack./dehyd.[c]
I-SBAS	0.46 ± 0.01[d]	0.70 ± 0.01	0.26 ± 0.01	1.42 ± 0.02	0.97 ± 0.03	1.46 ± 0.05
EFAl-SBAS	26.3 ± 1.5	33.5 ± 1.0	13.9 ± 0.7	74 ± 3	82 ± 4	0.90 ± 0.06
EFAl-SBAS / I-SBAS[e]	58 ± 4	48 ± 2	54 ± 3	52 ± 2	84 ± 5	

[a]overall cracking. [b]dehydrogenation. [c]TOF ratio of overall cracking to dehydrogenation. [d]uncertainties are taken as 95% confidence interval. [e]TOF ratio of EFAl-SBAS to I-SBAS.

The TOF for all the cracking and dehydrogenation pathways in the H-MFI-15 samples have linear correlation with the percentage of EFAl-SBAS at all partial pressures of pentane (0.025 - 25 mbar) and 793 K. Take the $C_1+C_4^=$ cracking pathway at 0.025 mbar pentane partial pressure for example, as shown in supplementary Figure 3.6. By extrapolating the linear curve to 100% EFAl-SBAS, the TOF of EFAl-SBAS in each reaction pathway is obtained.

The reaction rate showed a first order dependence for all pathways (Supplementary Figure 3.7, supplementary Figure 3.8 and supplementary Table 3.3) on both I-SBAS and EFAl-SBAS sites at 793 K, indicating a low coverage of pentane on SBAS under reaction conditions. The TOF of I-SBAS and EFAl-SBAS at different temperatures (793 - 753 K) were determined (Supplementary Table 3.4) and the apparent activation energy and entropy were calculated accordingly (Supplementary Table 3.5). Since pentane has a reaction order of 1, the apparent activation energy and entropy represents the barrier from gas pentane to the transition state on SBAS. Taking account of the pentane adsorption heat and entropy, the intrinsic barrier, i.e., the barrier from adsorbed pentane to transition state, was obtained and summarized in Table 3.3 and supplementary Figure 3.9.

3.3.3. Elementary steps for pentane cracking on zeolite.

Step 1. Pentane adsorption on BAS of zeolite.

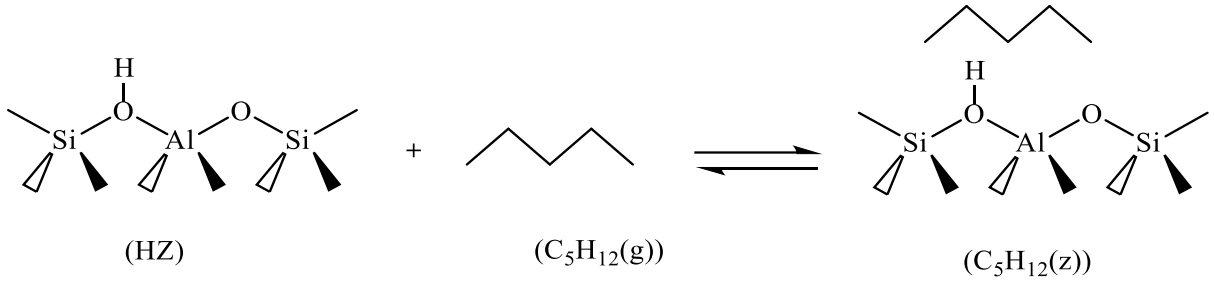

(HZ) (C_5H_{12}(g)) (C_5H_{12}(z))

Step 2. Protolytic cracking of adsorbed pentane in the zeolite based on transition state.

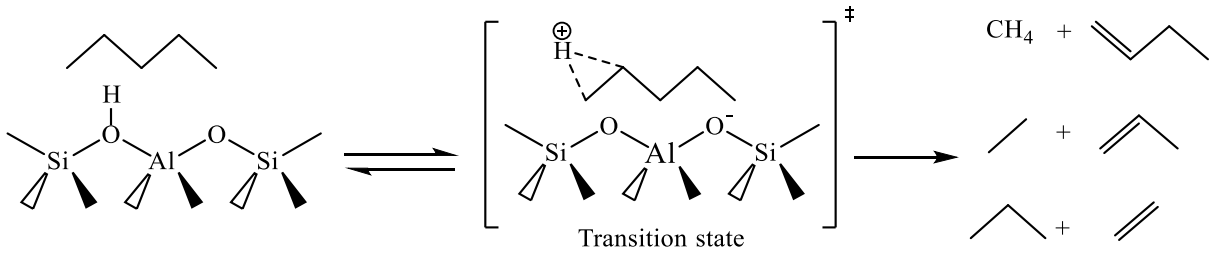

($\left[C_4H_9^+ \cdots\cdots Z^- \right]^{\ddagger}$)

Scheme 3.2. Elementary steps for pentane cracking on the H-MFI zeolite channel. Where, HZ is the H-MFI zeolite, C_5H_{12}(z) is adsorbed pentane on BAS.

Scheme 3.2 illustrates the proposed reaction pathways for pentane monomolecular cracking. Gaseous pentane (C_5H_{12}(g)) is adsorbed on the BAS ((C_5H_{12}(z)) via quasi-equilibrium step (Step 1, Scheme 3.2). Pentane is adsorbed on the BAS usually at very low coverage for the monomolecular cracking, so the adsorbed pentane in the zeolite channel is proportional to the gaseous pentane pressures and adsorption equilibrium constant.

$$C_{C_5H_{12}} = K_{ads}\, P_{C_5H_{12}} \qquad (6)$$

Where $C_{C_5H_{12}}$ is the adsorbed pentane on the BAS in the channel of zeolite, K_{ads} is the adsorption constant of pentane on the BAS and $P_{C_5H_{12}}$ is the gaseous pentane pressure.

A penta-coordinated carbonium ion transition state is existed between adsorbed pentane C_5H_{12}(z) and products (Step 2, Scheme 3.2) through quasi-equilibrium step. According to the

transition state theory (TST), the total measured reaction rate is derived from the transition state rate constant and the concentration of the activated complexes in the transition state.

$$r_{meas} = k^{\ddagger} C_{[C_5H_{13}^{+} \cdots\cdots Z^{-}]^{\ddagger}} \quad (7)$$

In which, $C_{[C_5H_{13}^{+} \cdots\cdots Z^{-}]^{\ddagger}}$ is the concentration of the activated complexes in the transition state and $k^{\ddagger}$ is transition state rate constant.

$k^{\ddagger}$ can be derived from

$$k^{\ddagger} = \nu\kappa \quad (8)$$

In which, ν is the frequency of the vibrational mode in the transition state crossing the activation barrier to the products, κ is the transmission coefficient of the transition sate crossing the activation barrier to the product and it is usually considered as 1.

The $C_{[C_5H_{13}^{+} \cdots\cdots Z^{-}]^{\ddagger}}$ can be attained from following equation:

$$K^{\ddagger} = \frac{C_{\left[C_5H_{13}^{+} \cdots\cdots Z^{-}\right]^{\ddagger}}}{C_{C_5H_{12}} C_{HZ}} \quad (9)$$

Where, C_{HZ} is the concentration of unoccupied BAS in the zeolite channel.

Combining (7), (8) and (9), the overall measured rate can be expressed as following:

$$r_{meas} = \nu K^{\ddagger} C_{C_5H_{12}} C_{HZ} \quad (10)$$

The $K^{\ddagger}$ is also derived by thermodynamic expression:

$$K^{\ddagger} = \frac{k_B T}{h\nu} e^{\frac{-\Delta G^{\ddagger}}{RT}} \quad (11)$$

So, the overall measured rate can be expressed as following:

$$r_{meas} = \frac{k_B T}{h} e^{\frac{-\Delta G^{\ddagger}}{RT}} C_{C_5H_{12}} C_{HZ} \quad (12)$$

As the monomolecular cracking of alkane is carried out at very low conversion, most of the BAS is not covered, so C_{HZ} is closed to 1.

So, the overall measured reaction rate can be rewritten as following:

$$r_{meas} = k_{int} C_{C_5H_{12}} \quad (13)$$

So, overall reaction rate is attained by the following equation:

$$r_{meas} = k_{int} K_{ads} P_{C_5H_{12}} = k_{meas} P_{C_5H_{12}} \quad (14)$$

$$k_{meas} = k_{int} K_{ads} \quad (15)$$

According to Arrhenius equation,

$$k_{meas} = A_{meas} e^{\frac{-Ea_{meas}}{RT}} \quad (16)$$

$$k_{int} = A_{int} e^{\frac{-Ea_{int}}{RT}} \quad (17)$$

$$K_{ads} = e^{\frac{-(\Delta H_{ads} - T\Delta S_{ads})}{RT}} \quad (18)$$

Where A_{meas} and A_{int} are the measured and intrinsic pre-exponential factor, Ea_{meas} and Ea_{int} are the measured and intrinsic activation energy, ΔH_{ads} and ΔS_{ads} are the adsorption enthalpy and entropy.

Combing equation (15)-(18), the intrinsic activation energy and pre-exponential factor can be derived as following:

$$Ea_{int} = Ea_{meas} - \Delta H_{ads} \quad (19)$$

$$\ln(A_{int}) = \ln(A_{meas}) - \frac{\Delta S_{ads}}{R} \quad (20)$$

Combing with $\Delta S_{int} = \Delta S_{meas} - \Delta S_{ads}$ (21)

The measured activation entropy can be refined as

$$\Delta S_{meas} = R(\ln(A_{meas}) - \ln(\frac{k_B T}{h})) \quad (22)$$

For dehydrogenation of pentane, the intrinsic activation energy ($E_a^{\ddagger}$,int) of EFAl-SBAS and I-SBAS (239 ± 6 and 238 ± 3 kJ mol^{-1}, respectively) are similar. Thus, the higher dehydrogenation rate of the EFAl-SBAS with respect to the I-SBAS is attributed to a larger entropy gain in the transition state (70 ± 8 J mol^{-1}K^{-1} on EFAl-SBAS vs. 35 ± 6 J mol^{-1}K^{-1} on I-SBAS). For the cracking pathway, the overall cracking $E_a^{\ddagger}$,int on EFAl-SBAS (219 ± 5 kJ mol^{-1}) is higher than on I-SBAS (203 ± 2 kJ mol^{-1}), suggesting an enthalpic destabilization of the cracking transition state on the EFAl-SBAS with respect to I-SBAS. The higher intrinsic activation entropy ($\Delta S^{\ddagger}$,int) for overall cracking with EFAl-SBAS (56 ± 8 J mol^{-1}K^{-1}) compared to I-SBAS (3 ± 6 J mol^{-1}K^{-1}) overcompensates the enthalpic destabilization of the transition state on EFAl-SBAS. Therefore, both the higher rates in cracking and dehydrogenation on EFAl-SBAS are caused by significantly higher transition entropies.

The compensation effect between the apparent activation energy and pre-exponential factor, or between activation enthalpy and entropy, were observed in alkanes with increased carbon numbers over H-MFI zeolite [24], a series of zeolites with different zeolite structures [25, 26] or zeolites exchanged with different metals [27]. Such compensation also exists in different reaction pathways (cracking and dehydrogenation) of alkane on both I-SBAS and EFAl-SBAS sites (Figure 3.10). Despite an increase of the $E_a^{\ddagger}$,int in all the pentane reaction pathways on the EFAl-SBAS site, with respect to the I-SBAS, overcompensation between $E_a^{\ddagger}$,int and $\Delta S^{\ddagger}$,int leads to a lower free energy on the EFAl-SBAS, resulting in prominent improvement of the TOF in the EFAl-SBAS. A comparable lower free energy (21-25 kJ mol^{-1}) of the EFAl-SBAS site is found in all the pentane cracking pathways.

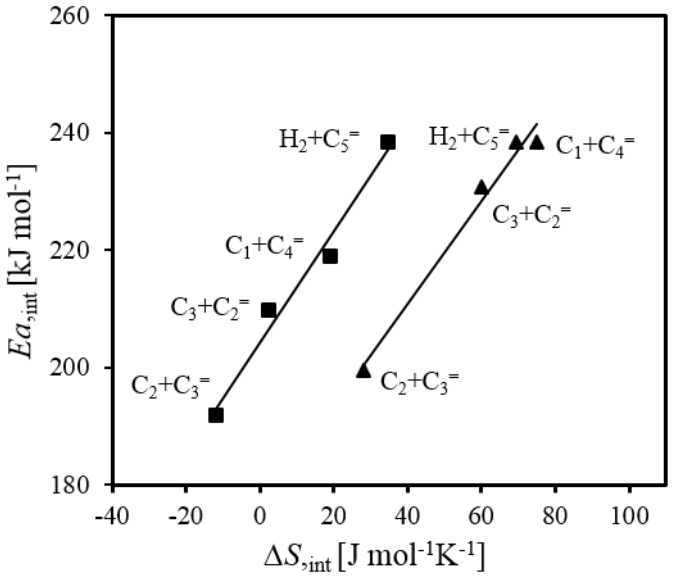

Figure 3.10 Compensation effect between intrinsic activation and entropy in pentane different reaction pathways (cracking and dehydrogenation) on I-SBAS (■) and EFAl-SBAS (▲) of H-MFI-15.

Table 3.3. The intrinsic activation energy, entropy and Gibbs free energy of cracking and dehydrogenation for I-SBAS and EFAl-SBAS in H-MFI-15 samples (T = 793 K)*

Active site	$E_a^{\ddagger}$,int (kJ mol^{-1})					$\Delta S^{\ddagger}$,int (J mol^{-1}K^{-1})					$\Delta G^{\ddagger}$,int (kJ mol^{-1})				
	$C_1 + C_4^=$	$C_2 + C_3^=$	$C_3 + C_2^=$	overall[a]	dehyd.[b]	$C_1 + C_4^=$	$C_2 + C_3^=$	$C_3 + C_2^=$	Overall	dehyd.	$C_1 + C_4^=$	$C_2 + C_3^=$	$C_3 + C_2^=$	overall	dehyd.
I-SBAS	219 ± 2[c]	192 ± 2	210 ± 3	203 ± 2	238 ± 3	19 ± 6	-11 ± 6	3 ± 7	3 ± 6	35 ± 6	197 ± 1	195 ± 1	201 ± 1	194 ± 1	204 ± 1
EFAl-SBAS	239 ± 6	200± 4	232 ± 6	219 ± 5	239 ± 6	79 ± 8	32 ± 7	65 ± 8	56 ± 8	70 ± 8	170 ± 1	168 ± 1	174 ± 1	168 ± 1	174 ± 1
Difference value[d]	20 ± 6	8 ± 5	22 ± 6	16 ± 6	1 ± 6	60 ± 10	43 ± 9	62 ±	53 ± 10	35 ± 10	-27 ± 1	-27 ± 1	-27 ± 1	-26 ± 1	-30 ± 1

11

[a]overall cracking. [b]dehydrogenation. [c]uncertainties are taken as 95% confidence interval. [d]difference value between EFAl-SBAS and I-SBAS.

*See the following data set for 763-793K in supplementary Table 3.4, for which $E_a^{\ddagger}$, $\Delta S^{\ddagger}$ and $\Delta G^{\ddagger}$

The promotional effect of EFAl on SBAS varies in different cracking pathways. Similar TOF ratios between EFAl-SBAS and I-SBAS were observed for $C_1+C_4^=$ and $C_3+C_2^=$ cracking pathways (58 ± 4 and 54 ± 3, respectively), while the TOF ratio for $C_2+C_3^=$ cracking pathway was lower (48 ± 2). Such difference is also reflected by the activation enthalpy and entropy. While the $C_1+C_4^=$ and $C_3+C_2^=$ cracking pathways had similar $E_a^{\ddagger}{}_{,int}$ and $\Delta S^{\ddagger}{}_{,int}$, the $C_2+C_3^=$ cracking pathway showed a substantial lower $E_a^{\ddagger}{}_{,int}$ and $\Delta S^{\ddagger}{}_{,int}$ (Table 3.3). This is hypothesized to be caused by the fact that the $C_1+C_4^=$ and $C_3+C_2^=$ cracking pathways pass through a C2-carbenium ion like transition state (C···C$^+$-C-C-C & C-C$^+$···C-C-C), while $C_2+C_3^=$ cracking pathway passes a C3-carbenium ion like transition state (C-C···C$^+$-C-C), as shown in Figure 3.11. With the C$^+$ anchored strongly on the negatively charged framework O$^-$, the C2-carbenium ion like transition state requires a larger space for the configurational degrees of freedom than the C3-carbenium ion like transition state. In addition, the C2-carbenium ion like transition state has a less symmetric structure than the C3-carbenium ion like transition state. Both result in lower entropy for the C3-carbenium ion like transition state.

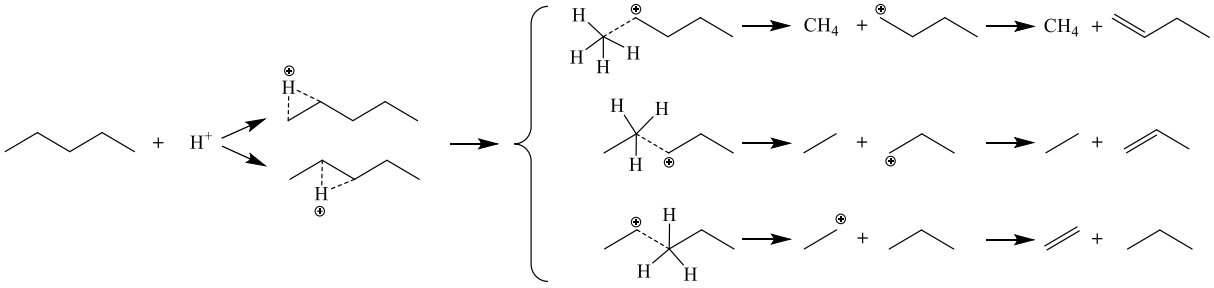

Figure 3.11. Proposed transition state of $C_1+C_4^=$, $C_2+C_3^=$ and $C_3+C_2^=$ pathways on I-SBAS and EFAl-SBAS in pentane cracking. Dotted line represents location of the bond scission.

3.3.3 Impact of EFAl on the activity of SBAS in pentane cracking.

In contrast to reports attributing the higher catalytic activity to a higher Brønsted acid strength [28-31], we have shown the increase in the conversion of alkanes, upon the presence of EFAl, is caused mostly in entropic gains in the transition state of monomolecular dehydrogenation and cracking transitions [11]. It should be noted that the adsorbed states have hardly been influenced by EFAl.

It is reported that the cracking and dehydrogenation activity of zeolitic BAS is location dependent [7, 8]. Jenda and Bell [8] showed that BAS in the channel intersections of H-MFI type zeolite have better catalytic activity than in straight and sinousoidal channels in butane cracking and dehydrogenation. Gounder and Iglesia [7] concluded that the different confining environments for BAS at different locations in H-MOR and H-MFI lead to the differences in the catalytic activities for the cracking and dehydrogenation of butane and propane. Since the EFAl-SBAS in this work are created by steaming, their high cracking and dehydrogenation TOF could also be the result of a selective removal of less active BAS (framework Al) and the BAS with high activity remains after steaming. However, this should only have a minor contribution to the TOF increase, because a mild steaming of H-MFI-15(0%) for 1 h (to H-MFI-15(5%)) increased the weight-normalized cracking and dehydrogenation rate from 0.63 μmol $s^{-1}g^{-1}$ to 2.1 μmol $s^{-1}g^{-1}$ (Supplementary Table 3.6**)**. Since selective removal of BAS would in any case decrease the weight-normalized rate of H-MFI, such a 3-fold increase should be dominantly contributed by the creation of EFAl-SBAS sites. The good linear correlation between EFAl-SBAS percentage in H-MFI and the pentane cracking and dehydrogenation TOF, also indicates that regardless of the location of the EFAl-SBAS in the micropores of H-MFI, the promotion of the rate is identical, pointing to a minor effect of the location of the SiOHAl group in the zeolite.

3.4 Conclusions

The close proximity of EFAl-SBAS were concluded unequivocally from the IR spectra of adsorbed pyridine and adsorbed pentane. The new site pair had the same binding strength with pentane as isolated SBAS.

The SBAS normalized rates of protolytic pentane conversion along all reaction pathways increased linearly with the percentage of EFAl-SBAS in H-MFI. The rates of overall cracking and dehydrogenation (793K) on EFAl-SBAS were 52 and 84-times higher than that on I-SBAS, respectively. The higher rates for pentane cracking and dehydrogenation on EFAl-SBAS are attributed to the stabilization of the transition states via a higher activation entropy. For all reaction pathways the higher activity is related to a later transition state. Identical increments from I-SBAS to EFAl-SBAS are observed in the transition state activation energy and entropy for the $C_1+C_4^=$ and $C_3+C_2^=$ cracking pathways. The formation of the C2-carbenium ion like transition state in these two pathways requires larger space for its configurational stabilization and is more sensitive to the spatial constraints provided by the EFAl-SBAS. This enhancement

of constraint is independent of the location of the site pair in the MFI pore structure. We currently probe to what extent it depends on the chemical nature of the constraining oxide nanocluster.

3.5 Contributions

The work in this chapter was under the supervision of Prof. Dr. Johannes A. Lercher, Dr. Yue Liu and Dr. Ricardo Bermejo-Deval. Yang Zhang contributed to the design of the experiments and operating setups and data analysis. Edith Berger and Teresa Schachtl contributed to the vacuum TGA measurements. Ruixue Zhao, Dr.Maricruz Sanchez-Sanchez and Prof. Dr. Gary L. Haller contributed for fruitful discussions.

3.6 References

[1] S.M. Babitz, B.A. Williams, J.T. Miller, R.Q. Snurr, W.O. Haag, H.H. Kung, Monomolecular cracking of n-hexane on Y, MOR, and ZSM-5 zeolites, *Applied Catalysis A:general*, 179 (**1999**) 71-86.

[2] L.H. Ong, M. Dömök, R. Olindo, A.C. van Veen, J.A. Lercher, Dealumination of HZSM-5 via steam-treatment, *MICROPOR MESOPOR MAT*, 164 (**2012**) 9-20.

[3] Y.V. Kissin, CHEMICAL MECHANISMS OF CATALYTIC CRACKING OVER SOLID ACIDIC CATALYSTS: ALKANES AND ALKENES, *Catalysis Reviews*, 43 (**2001**) 85-146.

[4] W.O. Haag, R.M. Lago, P.B. Weisz, The active site of acidic aluminosilicate catalysts, *Nature*, 309 (**1984**) 589.

[5] B.S. Kwak, W.M.H. Sachtler, W.O. Haag, Catalytic Conversion of Propane to Aromatics: Effects of Adding Ga and/or Pt to HZSM-5, *Journal of Catalysis*, 149 (**1994**) 465-473.

[6] A. Bhan, R. Gounder, J. Macht, E. Iglesia, Entropy considerations in monomolecular cracking of alkanes on acidic zeolites, *Journal of Catalysis*, 253 (**2008**) 221-224.

[7] R. Gounder, E. Iglesia, Catalytic Consequences of Spatial Constraints and Acid Site Location for Monomolecular Alkane Activation on Zeolites, *Journal of the American Chemical Society*, 131 (**2009**) 1958-1971.

[8] A. Janda, A.T. Bell, Effects of Si/Al Ratio on the Distribution of Framework Al and on the Rates of Alkane Monomolecular Cracking and Dehydrogenation in H-MFI, *Journal of the American Chemical Society*, 135 (**2013**) 19193-19207.

[9] T. Masuda, Y. Fujikata, S.R. Mukai, K. Hashimoto, Changes in catalytic activity of MFI-type zeolites caused by dealumination in a steam atmosphere, *Applied Catalysis A:general*, 172 (**1998**) 73-83.

[10] D.P. Ivanov, L.V. Pirutko, G.I. Panov, Effect of steaming on the catalytic performance of ZSM-5 zeolite in the selective oxidation of phenol by nitrous oxide, *Journal of Catalysis*, 311 (**2014**) 424-432.

[11] S. Schallmoser, T. Ikuno, M.F. Wagenhofer, R. Kolvenbach, G.L. Haller, M. Sanchez-Sanchez, J.A. Lercher, Impact of the local environment of Brønsted acid sites in ZSM-5 on the catalytic activity in n-pentane cracking, *Journal of Catalysis*, 316 (**2014**) 93-102.

[12] H. Krannila, W.O. Haag, B.C. Gates, Monomolecular and bimolecular mechanisms of paraffin cracking: n-butane cracking catalyzed by HZSM-5, *Journal of Catalysis*, 135 (**1992**) 115-124.

[13] N. Xue, A. Vjunov, S. Schallmoser, J.L. Fulton, M. Sanchez-Sanchez, J.Z. Hu, D. Mei, J.A. Lercher, Hydrolysis of zeolite framework aluminum and its impact on acid catalyzed alkane reactions, *Journal of Catalysis*, 365 (**2018**) 359-366.

[14] G.C. Bond, M.A. Keane, H. Kral, J.A. Lercher, Compensation Phenomena in Heterogeneous Catalysis: General Principles and a Possible Explanation, *Catalysis Reviews*, 42 (**2000**) 323-383.

[15] W.O. Haag, R.M. Lago, P.B. Weisz, Transport and reactivity of hydrocarbon molecules in a shape-selective zeolite, *Faraday Discussions of the Chemical Society*, 72 (**1981**) 317-330.

[16] B.A. De Moor, M.-F. Reyniers, O.C. Gobin, J.A. Lercher, G.B. Marin, Adsorption of C2−C8 n-Alkanes in Zeolites, *The Journal of Physical Chemistry C*, 115 (**2011**) 1204-1219.

[17] N. Bhadusha, T. Ananthabaskaran, Kinetic, Thermodynamic and Equilibrium Studies on Uptake of Rhodamine B onto ZnCl2 Activated Low Cost Carbon, *E-Journal of Chemistry*, 9 (**2012**)137-144.

[18] J.A. van Bokhoven, M. Tromp, D.C. Koningsberger, J.T. Miller, J.A.Z. Pieterse, J.A. Lercher, B.A. Williams, H.H. Kung, An Explanation for the Enhanced Activity for Light Alkane Conversion in Mildly Steam Dealuminated Mordenite: The Dominant Role of Adsorption, *Journal of Catalysis*, 202 (**2001**) 129-140.

[19] F. Eder, M. Stockenhuber, J.A. Lercher, Brønsted Acid Site and Pore Controlled Siting of Alkane Sorption in Acidic Molecular Sieves, *The Journal of Physical Chemistry B*, 101 (**1997**) 5414-5419.

[20] H. Li, S.A. Kadam, A. Vimont, R.F. Wormsbecher, A. Travert, Monomolecular Cracking Rates of Light Alkanes over Zeolites Determined by IR Operando Spectroscopy, *ACS Catalysis*, 6 (**2016**) 4536-4548.

[21] R. Kolvenbach, L.F. Gonzalez Peña, A. Jentys, J.A. Lercher, Diffusion of Mixtures of Light Alkanes and Benzene in Nano-Sized H-ZSM5, *The Journal of Physical Chemistry C*, 118 (**2014**) 8424-8434.

[22] J.F. Denayer, W. Souverijns, P.A. Jacobs, J.A. Martens, G.V. Baron, High-Temperature Low-Pressure Adsorption of Branched C5−C8 Alkanes on Zeolite Beta, ZSM-5, ZSM-22, Zeolite Y, and Mordenite, *The Journal of Physical Chemistry B*, 102 (**1998**) 4588-4597.

[23] R. Kolvenbach, L.F. Gonzalez-Peňa, A. Jentys, J.A. Lercher, Molecular Understanding of Sorption in Mesoscale Organized Zeolites with MFI Structure, *Catalysis Letters*, 143 (**2013**) 1116-1122.

[24] J.A. van Bokhoven, B.A. Williams, W. Ji, D.C. Koningsberger, H.H. Kung, J.T. Miller, Observation of a compensation relation for monomolecular alkane cracking by zeolites: the dominant role of reactant sorption, *Journal of Catalysis*, 224 (**2004**) 50-59.

[25] N. Katada, S. Sota, N. Morishita, K. Okumura, M. Niwa, Relationship between activation energy and pre-exponential factor normalized by the number of Bronsted acid sites in cracking of short chain alkanes on zeolites, *Catalysis Science & Technology*, 5 (**2015**) 1864-1869.

[26] A. Janda, B. Vlaisavljevich, L.-C. Lin, B. Smit, A.T. Bell, Effects of Zeolite Structural Confinement on Adsorption Thermodynamics and Reaction Kinetics for Monomolecular Cracking and Dehydrogenation of n-Butane, *Journal of the American Chemical Society*, 138 (**2016**) 4739-4756.

[27] A. Corma, F. Llopis, J.B. Monton, S. Weller, On the Compensation Effect in Acid-Base Catalyzed Reactions on Zeolites, *Journal of Catalysis*, 142 (**1993**) 97-109.

[28] S. Li, A. Zheng, Y. Su, H. Zhang, L. Chen, J. Yang, C. Ye, F. Deng, Brønsted/Lewis Acid Synergy in Dealuminated HY Zeolite: A Combined Solid-State NMR and Theoretical Calculation Study, *Journal of the American Chemical Society*, 129 (**2007**) 11161-11171.

[29] S. Li, S.-J. Huang, W. Shen, H. Zhang, H. Fang, A. Zheng, S.-B. Liu, F. Deng, Probing the Spatial Proximities among Acid Sites in Dealuminated H-Y Zeolite by Solid-State NMR Spectroscopy, *The Journal of Physical Chemistry C*, 112 (**2008**) 14486-14494.

[30] E.A. Pidko, S.M.T. Almutairi, B. Mezari, P.C.M.M. Magusin, E.J.M. Hensen, Chemical Vapor Deposition of Trimethylaluminum on Dealuminated Faujasite Zeolite, *ACS Catalysis*, 3 (**2013**) 1504-1517.

[31] S.M.T. Almutairi, B. Mezari, G.A. Filonenko, P.C.M.M. Magusin, M.S. Rigutto, E.A. Pidko, E.J.M. Hensen, Influence of Extraframework Aluminum on the Brønsted Acidity and Catalytic Reactivity of Faujasite Zeolite, *ChemCatChem*, 5 (**2013**) 452-466.

Supporting information

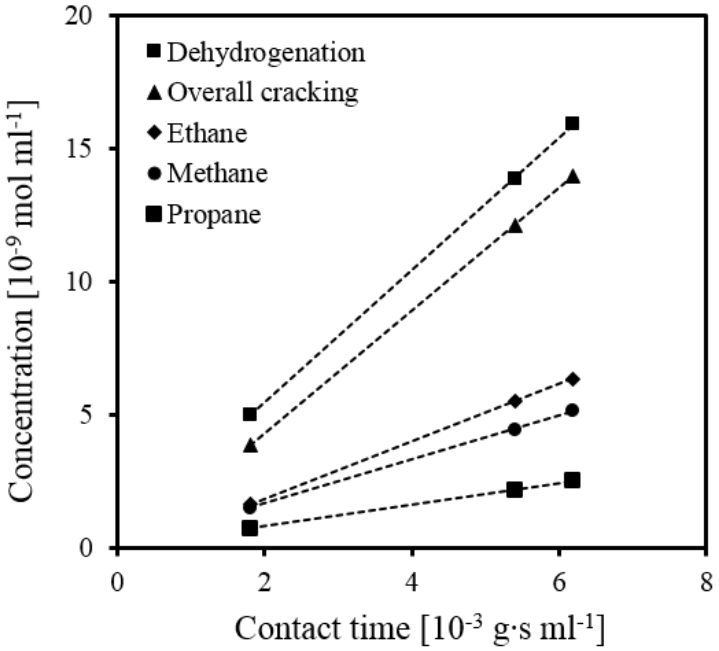

Supplementary Figure 3.1. Concentration of products in different reaction pathways at different contact time (1-2% pentane conversion) in H-MFI-15(43%) sample at 793K.

The products concentration of pentane cracking and dehydrogenation increased with the contact time. The slop value of the line is the initial rate, which is attained after extrapolation the line to 0 contact time. Initial rate was used to calculate the activation energy and entropy, which were in consistent with values in the literatures [1, 2].

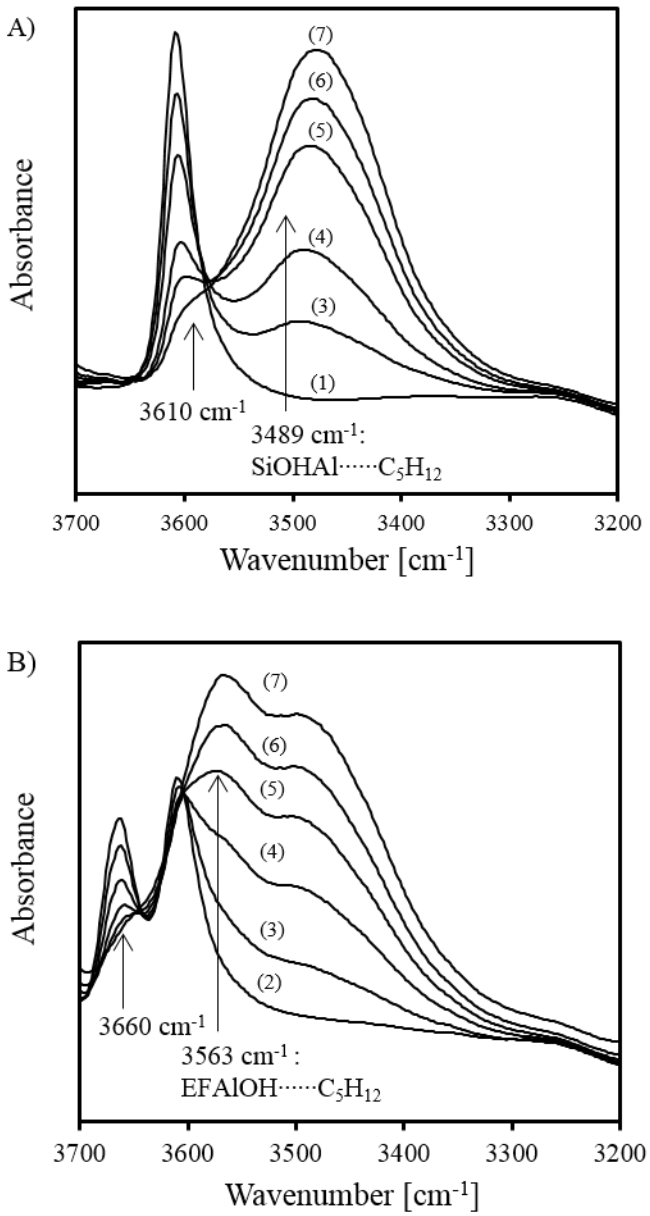

Supplementary Figure 3.2. IR spectra of OH stretching vibration region of 3700 to 3200 cm^{-1} for A) H-MFI-15(0%) and B) H-MFI-15(43%) after pentane being adsorbed at different equilibrium pressures of 0.002 (1), 0.01 (2), 0.05 (3), 0.12 (4), 0.25 (5), 0.44 (6), and 0.85 (7) mbar. The lines indicate an increasing loss or gain in intensity of the IR bands with increasing pentane pressures from 0.002 to 0.85 mbar.

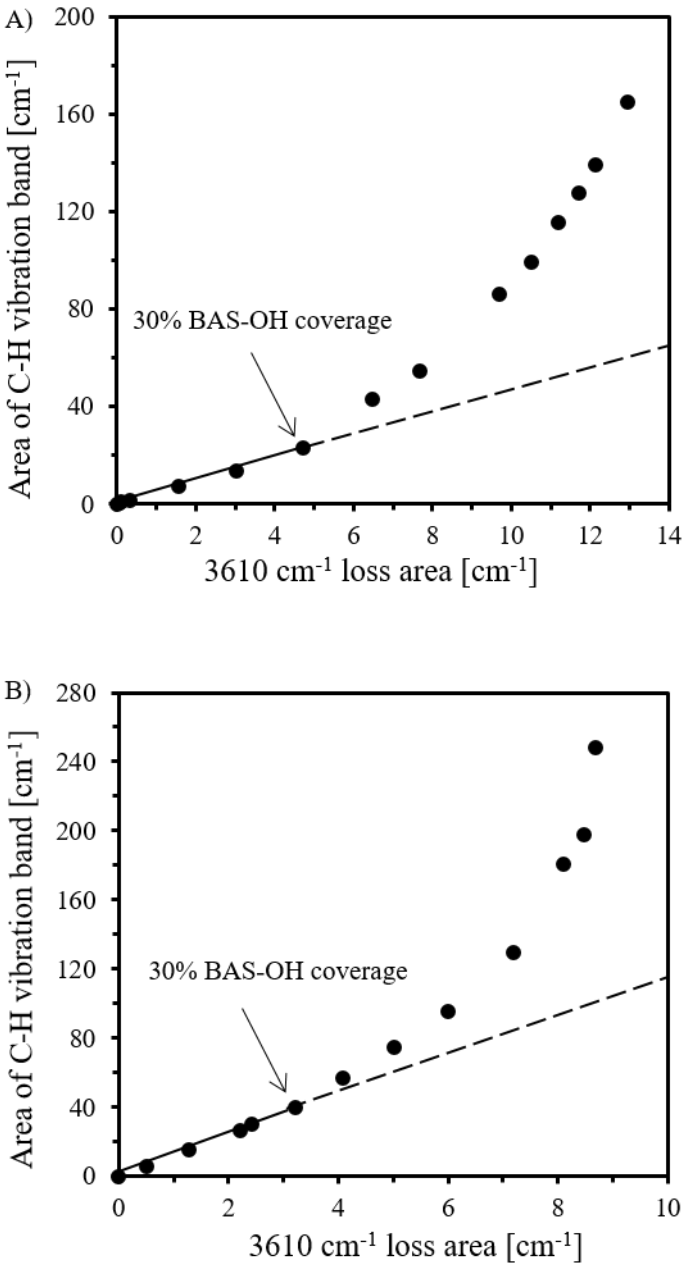

Supplementary Figure 3.3. The change of pentane uptake with the coverage of BAS-OH in H-MFI-15(0%) A) and H-MFI-15(43%) B) in IR spectra after pentane being adsorbed from 0.002 to 0.85 mbar equilibrium pressures. Pentane uptake is represented by the sum of area of C-H stretching vibration between 2677 and 3097 cm^{-1} and C-H deformation vibration at 1470 and 1380 cm^{-1}; coverage of BAS-OH is represented by the area loss of the band centered at 3610 cm^{-1}.

Pentane was adsorbed on BAS with 1:1 stoichiometry in H-MFI-15 up to 30% BAS-OH coverage and above 30% coverage more pentane was adsorbed per BAS.

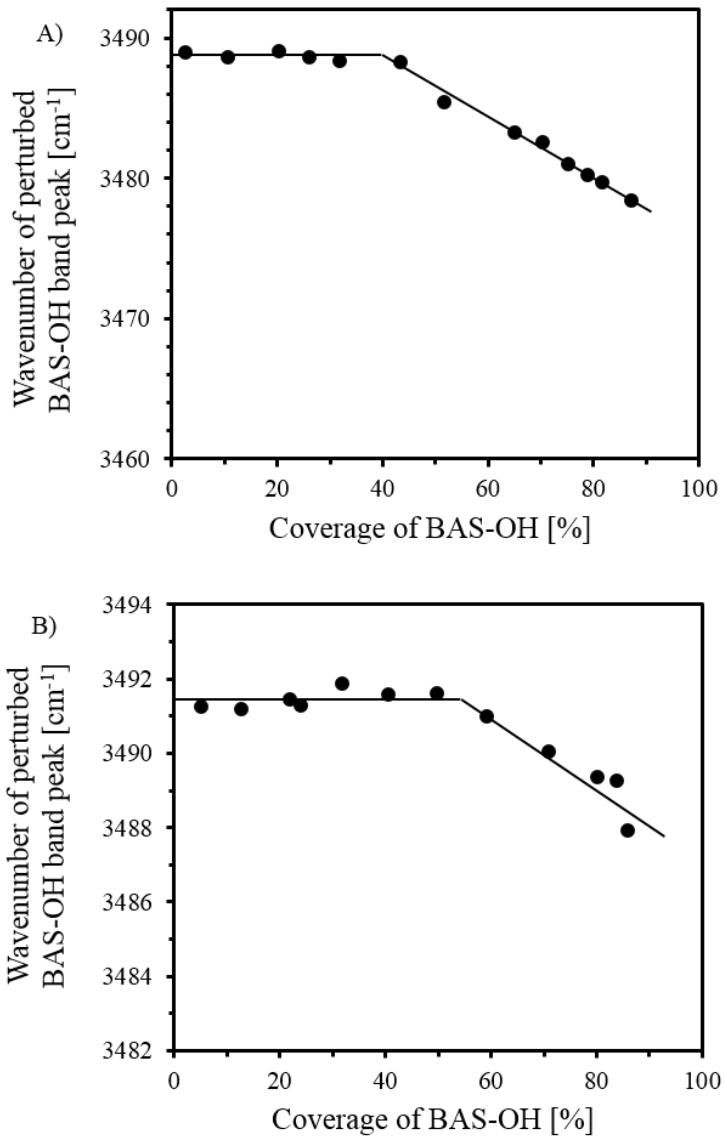

Supplementary Figure 3.4. The change of wavenumber of perturbed BAS-OH peak with the coverage of BAS-OH in H-MFI-15(0%) A) and H-MFI-15(43%) B) in IR spectra after pentane being adsorbed from 0.002 to 0.85 mbar equilibrium pressure.

On H-MFI-15(0%), the wavenumber of perturbed BAS-OH peak was about 3489 cm^{-1} before 30% BAS-OH coverage, and after 30% BAS-OH coverage, the perturbed OH band wavenumber was red-shift. On H-MFI-15(43%), the wavenumber of perturbed BAS-OH peak was about between 3491 and 3492 cm^{-1} before 30% BAS-OH coverage, and after 30% BAS-OH coverage, the perturbed OH band wavenumber was red-shift.

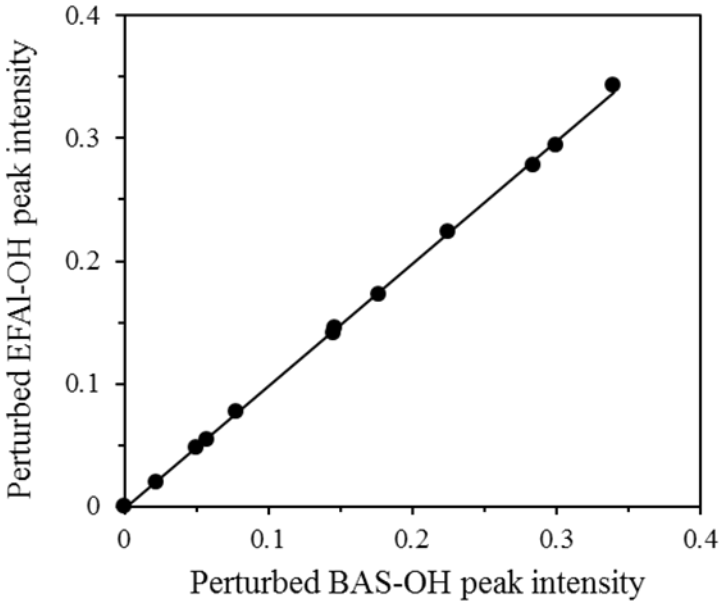

Supplementary Figure 3.5. The correlation of the peak intensity between perturbed BAS-OH and perturbed EFAl-OH of H-MFI-15(43%) in IR spectra after pentane being adsorbed from 0.02 to 0.87 mbar equilibrium pressures.

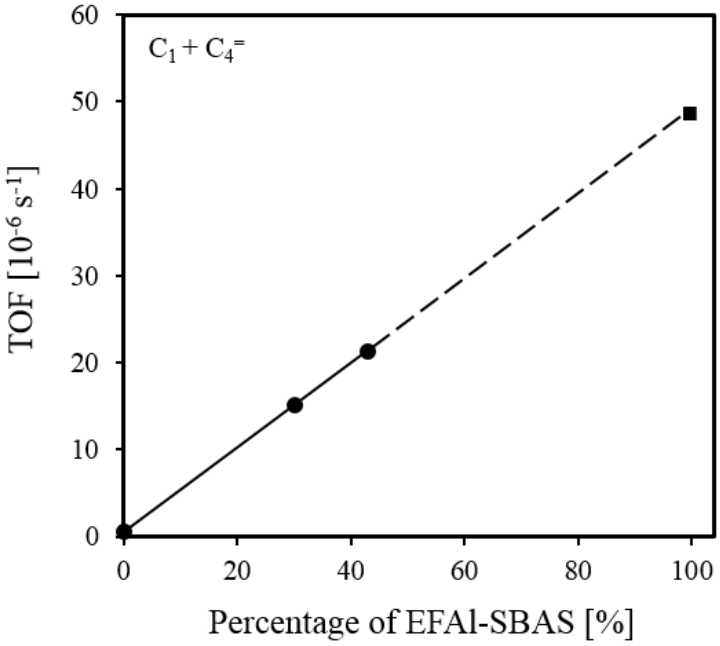

Supplementary Figure 3.6. Pentane cracking rate (per SBAS) of C_1+$C_4^=$ pathway as function of EFAl-SBAS percentage in the H-MFI-15 samples at 793 K reaction temperature and 0.025 mbar pentane partial pressure. (The round points are the measured TOF of the samples with different percentage of EFAl-SBAS and the square point is the TOF of EFAl-SBAS by extrapolation of the regressed line to 100% EFAl-SBAS).

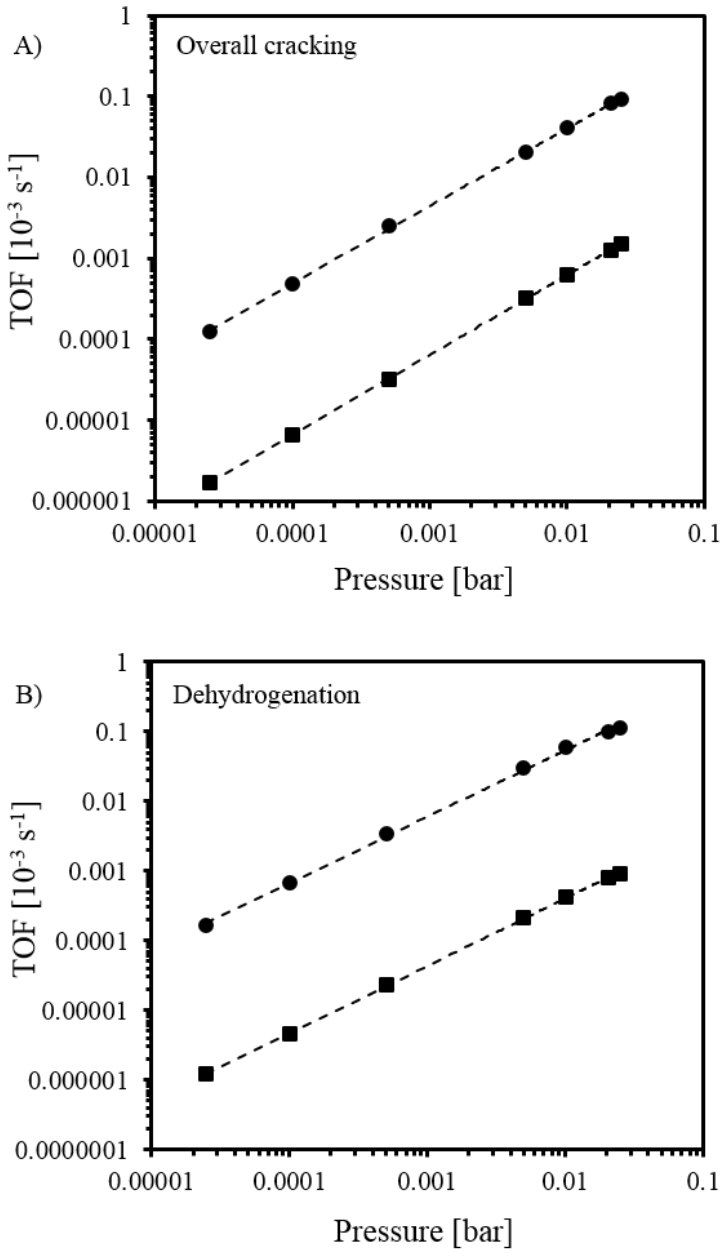

Supplementary Figure 3.7. First-order reaction of overall cracking A) and dehydrogenation B) on I-SBAS (■) and EFAl-SBAS (●) of H-MFI.

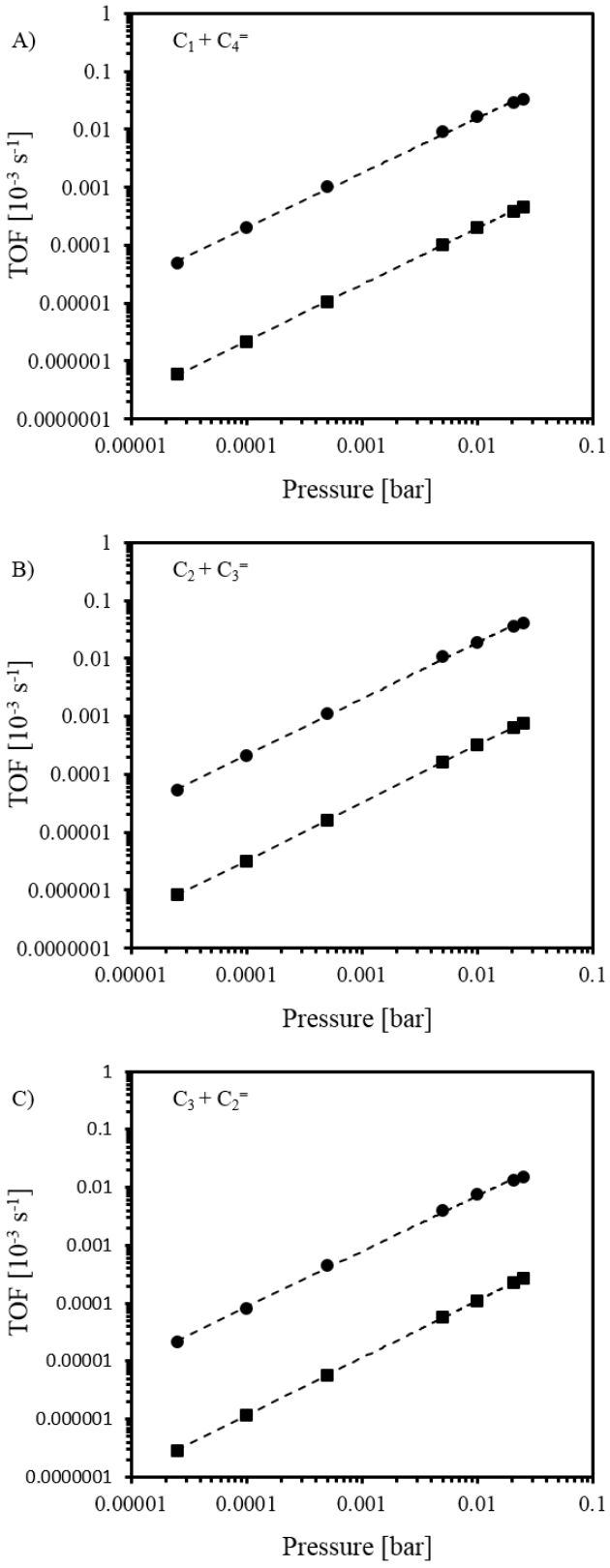

Supplementary Figure 3.8. First-order reaction of C_1+$C_4^=$ cracking pathway A), C_2+$C_3^=$ cracking pathway B), and C_3+$C_2^=$ cracking pathway C) on I-SBAS (■) and EFAl-SBAS (●) of H-MFI. First order reaction is found in all the cracking pathways on both I-SBAS and EFAl-SBAS sites at 793 K, which is summarized in supplementary Table 3.3.

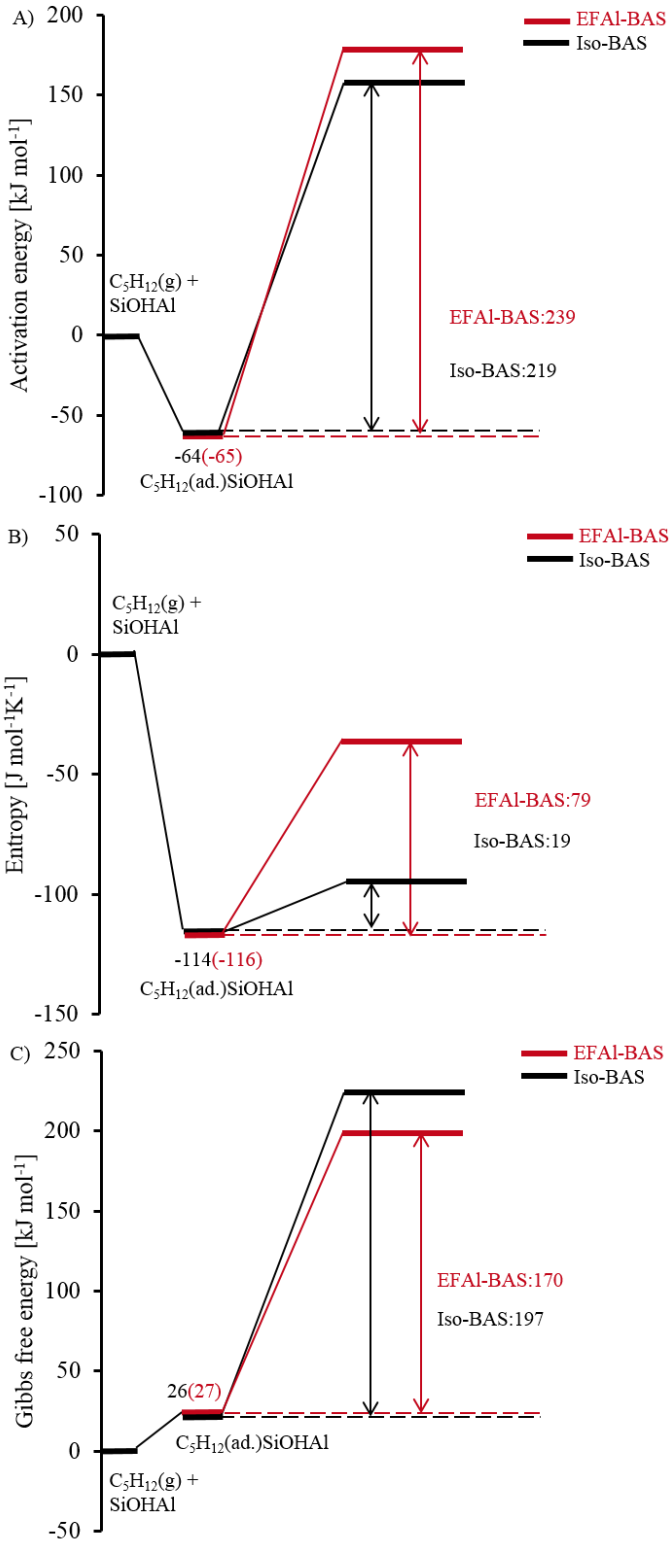

Supplementary Figure 3.9. The diagram of energy A), entropy B) and Gibbs free energy C) for $C_1+C_4^=$ cracking pathway of pentane on the EFAl-SBAS (red line) and Iso-SBAS (black line). The active site in zeolite is labeled as SiOHAl. All species, except for those denoted with (g), are in the zeolite pore. The temperature for Gibbs free energy is 793 K.

Supplementary Table 3.1. Turnover frequency (TOF) of pentane cracking and dehydrogenation in H-MFI-15 samples with different percentage of EFAl-SBAS (T = 793 K).

Sample	TOF [10^{-3} s^{-1}]					
	$C_1+C_4^=$	$C_2+C_3^=$	$C_3+C_2^=$	overall[a]	dehyd.[b]	C/D[c]
H-MFI-15(0%)	0.5±0.01	0.7±0.01	0.3±0.01	1.4±0.02	1.0±0.03	1.5
H-MFI-15(4%)	1.5±0.1	2.5±0.07	0.9±0.04	4.9±0.2	4.3±0.21	1.1
H-MFI-15(5%)	2.9±0.03	3.5±0.02	1.5±0.01	7.9±0.06	8.0±0.11	1.0
H-MFI-15(9%)	2.0±0.12	3.9±0.07	1.4±0.02	7.3±0.21	6.3±0.41	1.2
H-MFI-15(19%)	6.7±0.02	7.8±0.03	3.8±0.07	18.3±0.08	18.1±0.34	1.0
H-MFI-15(30%)	6.6±0.12	9.7±0.22	3.8±0.08	20.1±0.36	20.8±0.41	1.0
H-MFI-15(33%)	8.8±0.05	11.0±0.32	4.7±0.33	24.5±0.67	27.3±0.3	0.9
H-MFI-15(43%)	12.3±0.05	15.2±0.29	6.0±0.05	33.6±0.26	38.5±0.44	0.9

[a]overall cracking. [b]dehydrogenation. [c]overall cracking TOF / dehydrogenation TOF.

Supplementary Table 3.2. Turnover frequency (TOF) of pentane cracking and dehydrogenation in H-MFI samples with different percentage of EFAl-SBAS (T = 763 K).

Sample	TOF [10^{-3} s^{-1}]	
	overall[a]	dehyd.[b]
H-MFI-15(0%)	0.6±0.01	0.3±0.01
H-MFI-40(0%)	0.7±0.03	0.5±0.03
H-MFI-40(1%)[c]	1.1±0.02	0.6±0.01
H-MFI-15(4%)	1.9±0.12	1.5±0.05
H-MFI-15(5%)[d]	3.3±0.05	2.9±0.04
H-MFI-15(9%)	3.0±0.03	2.2±0.03
H-MFI-15(19%)	7.8±0.19	6.2±0.06
H-MFI-15(23%)[e]	5.4	5.3
H-MFI-15(30%)	8.3±0.36	7.4±0.08
H-MFI-15(33%)	9.6±0.42	9.5±0.02
H-MFI-15(43%)	12.3±0.29	12.7±0.11

[a]overall cracking. [b]dehydrogenation. [c] H-MFI-40(1%) derived from steaming of H-MFI-40(0%) at 100 kPa and 723 K for 1 h. [d] H-MFI-15(5%) derived from steaming of H-MFI-15(0%) at 100 kPa and 723 K for 1 h. [e] H-MFI-15(23%) derived from the literature [1] by static calcination (no flow of gas, ambient air present) of H-MFI-15.

Supplementary Table 3.3. Reaction order of reaction pathways for I-SBAS and EFAl-SBAS in H-MFI-15 samples; uncertainties are taken as 95% confidence interval.

Active sites	Reaction order				
	$C_1+C_4^=$	$C_2+C_3^=$	$C_3+C_2^=$	overall[a]	dehyd.[b]
I-SBAS	0.97±0.1	0.99±0.1	0.99±0.1	0.99±0.1	0.97±0.1
EFAl-SBAS	0.95±0.01	0.97±0.01	0.97±0.01	0.96±0.01	0.95±0.01

[a] overall cracking.[b]dehydrogenation.

Supplementary Table 3.4. TOF of pentane cracking and dehydrogenation on I-SBAS and EFAl-SBAS in H-MFI-15 samples (793-753 K).

Temperature	TOF, $_{I\text{-}SBAS}$ [10^{-3} s^{-1}]					TOF, $_{EFAl\text{-}SBAS}$ [10^{-3} s^{-1}]				
[K]	$C_1+C_4^=$	$C_2+C_3^=$	$C_3+C_2^=$	overall[a]	dehyd.[b]	$C_1+C_4^=$	$C_2+C_3^=$	$C_3+C_2^=$	overall	dehyd.
793	0.46 ± 0.01[c]	0.70 ± 0.01	0.26 ± 0.01	1.42 ± 0.02	0.97 ± 0.03	26.3 ± 1.5	33.5 ± 1.0	13.9 ± 0.7	74 ± 3	82 ± 4
783	0.34 ± 0.01	0.55 ± 0.01	0.19 ± 0.01	1.07± 0.01	0.69 ± 0.02	17.8 ± 1.0	24.8 ± 0.8	9.5 ± 0.6	52 ± 2	56 ± 2
773	0.25 ± 0.01	0.42 ± 0.01	0.14 ± 0.01	0.81 ± 0.02	0.48 ± 0.02	12.4 ± 0.7	18.7 ± 0.8	6.7 ± 0.4	38 ± 2	37 ± 2
763	0.18 ± 0.01	0.33 ± 0.01	0.11± 0.01	0.62 ± 0.01	0.34± 0.01	8.9 ± 0.5	14.6 ± 0.7	5.0 ± 0.3	28 ± 1	28 ± 1
753	0.13 ± 0.01	0.25 ± 0.01	0.08± 0.01	0.46 ± 0.01	0.24± 0.01	6.4 ± 1.3	11.2 ± 0.6	3.6 ± 0.3	21 ± 1	20± 1

[a]overall cracking. [b]dehydrogenation. [c]Uncertainties are taken as 95% confidence interval.

Supplementary Table 3.5. The apparent activation energy, entropy and Gibbs free energy of cracking and dehydrogenation for I-SBAS and EFAl-SBAS in H-MFI-15 samples (T = 793 K).

Active site	$E_a^{\ddagger}$,app (kJ mol^{-1})					$\Delta S^{\ddagger}$,app (J mol^{-1}K^{-1})				
	$C_1 + C_4^=$	$C_2 + C_3^=$	$C_3 + C_2^=$	overall[a]	dehyd.[b]	$C_1 + C_4^=$	$C_2 + C_3^=$	$C_3 + C_2^=$	overall	dehyd.
I-SBAS	155 ± 1	128 ± 1	146 ± 2	139 ± 1	174 ± 2	-95 ± 2	-126 ± 1	-112 ± 3	-111 ± 1	-79 ± 2
EFAl-SBAS	174 ± 6	135 ± 4	167 ± 5	154 ± 5	174 ± 5	-37 ± 7	-84 ± 5	-52 ± 7	-60 ± 6	-42 ± 7

[a]overall cracking. [b]dehydrogenation.

Supplementary Table 3.6. Rate of pentane cracking and dehydrogenation in H-MFI-15(0%) and H-MFI-15(5%) (T = 793 K)

Sample	Rate [10^{-6} mol s^{-1} g^{-1}]					
	$C_1+C_4^=$	$C_2+C_3^=$	$C_3+C_2^=$	overall[a]	dehyd.[b]	C/D[c]
H-MFI-15 (0%)	0.20±0.01	0.31±0.01	0.12±0.01	0.63±0.01	0.43±0.01	1.5
H-MFI-15(5%)	0.75±0.01	0.92±0.01	0.39±0.01	2.10±0.02	2.08±0.03	1.0

[a]overall cracking. [b]dehydrogenation. [c]overall cracking rate / dehydrogenation rate.

References

[1] S. Schallmoser, T. Ikuno, M.F. Wagenhofer, R. Kolvenbach, G.L. Haller, M. Sanchez-Sanchez, J.A. Lercher, Impact of the local environment of Brønsted acid sites in ZSM-5 on the catalytic activity in n-pentane cracking, *Journal of Catalysis*, 316 (**2014**) 93-102.

[2] R. Gounder, E. Iglesia, Catalytic Consequences of Spatial Constraints and Acid Site Location for Monomolecular Alkane Activation on Zeolites, *Journal of the American Chemical Society*, 131 (**2009**) 1958-1971.

Chapter 4

Improvement of ethene dimerization on H-MFI zeolite by proximity of extra-framework aluminum oxide and Brønsted acid sites

This chapter is based on:

Yang Zhang, Yue Liu*, Ricardo Bermejo-Deval*, and Johannes A. Lercher*, "Improvement of ethene dimerization on H-MFI zeolite by proximity of extra-framework aluminum oxide and Brønsted acid sites", in preparation, 2018.

ABSTRACT: The activity of ethene dimerization on a strong Brønsted acid site in H-MFI zeolites is improved by the presence of extra-framework aluminum oxide in spatial proximity. The TOF of ethene dimerization for this strong Brønsted acid site is 3 times higher than isolated strong Brønsted acid site. First order reaction for ethene conversion is observed on the two types of strong Brønsted acid sites and formation of ethoxide by adsorption of gaseous ethene is suggested as the rate determining step. The strong Brønsted acid site with extra-framework aluminum oxide in spatial proximity decreases activation enthalpy and activation entropy in the ethoxide formation step, which leads to a later transition state for ethoxide formation on strong Brønsted acid site with extra-framework aluminum oxide with respect to the isolated strong Brønsted acid site. EFAl in the H-MFI can stabilize the catalyst and prevent the deactivation of the active sites. This study suggests that activity of C-C bond formation and selectivity of the products can be tuned by the local environment of the active site within a zeolite micropores.

4.1. Introduction

Catalytic dimerization and oligomerization of light alkenes on zeolites has become a very important pathway to produce gasoline range hydrocarbons with high octane number [1-4]. It has been extensively studied that the reaction activities of dimerization of alkenes on different zeolites are greatly influenced by the size, shape of channels and cavities surrounding the solid Brønsted acid site (BAS) of zeolites [5-7].

Alkene can be adsorbed on the BAS of zeolite by physisorption and chemisorption [8-15]. The adsorption process of 2-pentene on the BAS is illustrated in Figure 4.1 [9]. Firstly, 2-pentene is physisorbed in the zeolite channel via van der Waals force. And then 2-pentene is adsorbed on BAS by hydrogen bonding between carbon-carbon double bond and the BAS. Consecutively, the hydrogen bonded pentene is protonated and chemisorbed on the BAS to form carbenium ion or alkoxide.

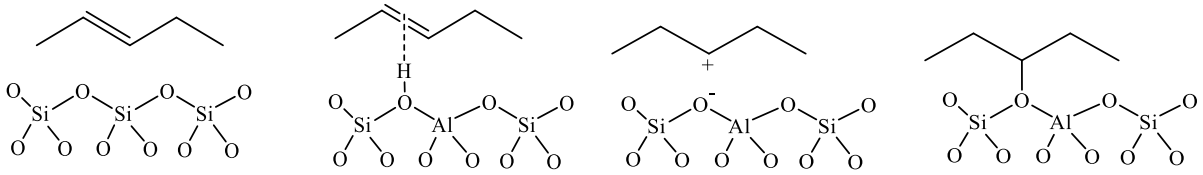

Figure 4.1. Adsorbed 2-pentene species on the BAS of zeolite.

The adsorption of alkanes on BAS of zeolites has been studied largely [16-22]. However, adsorption of alkenes on BAS of zeolites can occur together with fast reactions, such as isomerization, dimerization and oligomerization, even at low temperatures, leading to it difficult to attain adsorption enthalpy and entropy of alkene by experiment methods [8, 9]. Therefore, the theory methods have been greatly used to calculate the adsorption enthalpy and entropy of alkenes on the zeolites [8, 23]. Physisorption heat of alkene is increased with the decreased zeolite pore size on H-FAU, H-BEA, H-MOR and H-ZSM-5. While, the zeolites with higher van der Waals stabilization in the pores usually have higher chemisorption heat for the formation of alkoxide [8].

However, the theoretical calculated physisorption and chemisorption energy vary with the selected zeolite model and calculations methods [24, 25]. In addition, the steric effect of the pore wall to the active site and also the special geometric properties of the zeolite are usually neglected in the theory calculation. Some researchers tried to measure the adsorption energy of alkenes in zeolites by experiments [9, 14]. Van Hooff et al. [14] proposed energy of the hydrogen-bonded ethene molecule on the BAS of H-MFI zeolite to be 38 kJ mol^{-1}. While, Giuseppe et al. [11] splitted this energy to energy contributed from van der Waals interaction (22 kJ mol^{-1}) and pure hydrogen-bonding interaction (16 kJ mol^{-1}). Stefan et al. [9] measured physisorption and chemisorption energy of 2-pentene on H-MFI zeolite via IR and calorimetric methods. Silicalite-1 has similar structure as the H-MFI, but without BAS. Thus, the differential heat of adsorption of 2-pentene on silicalite-1 (−56 kJ mol^{-1}) can be employed to measure the physisorption heat of 2-pentene on the pore walls of H-MFI. The channel size of H-FER (0.54 × 0.42 nm) is smaller than that of H-MFI (0.56 × 0.53 nm), hindering the formation of alkoxide and dimerization products. In addition, the acid strength of H-FER is similar with that of H-MFI. Therefore, the adsorption enthalpy of 2-pentene on H-FER (−56 kJ mol^{-1}) can be used to calculate the enthalpy from hydrogen bonding of 2-pentene on H-MFI. The heat of adsorption of 2-pentene was measured to be −285 kJ mol^{-1}, combining with the known energy of dimerization of 2-pentene (−88 kJ mol^{-1}), dispersion forces (−120 kJ mol^{-1}), hydrogen bonding (-36 kJ mol^{-1}) of the C10 dimer, the energy from the hydrogen bonding to the alkoxide (-41 kJ mol^{-1}) of 2-pentene on H-MFI zeolite can be attained.

Two reaction mechanism of alkene dimerization on BAS of zeolite is proposed: Stepwise and concerted reaction mechanism.

Stepwise reaction mechanism:

Two steps are observed in the stepwise reaction mechanism: The first step is that one gaseous alkene is coordinated with the BAS via π bonding. After it crosses carbenium ion like transition state, an alkoxide is formed. In the second step, the second gaseous ethene is physisorbed in the zeolite channel and reacts with the already formed alkoxide. The new C-C bond is formed at the second transition state. At least two kinds of products are possibly formed: the first possibility is that the dimerized carbenium ion like transition state is deprotonated immediately to form a neutral alkene product and the second possibility is formation of alkoxide by coordination of the charged carbon atom to a zeolite oxygen [26].

Concerted reaction mechanism:

However, the alkoxide is not observed in some alkene dimerization studies. Theory study attributed it to be the concerted reaction mechanism: One gaseous alkene is physisorbed on the BAS to form π complex. After that, instead of formation of an alkoxide, second gaseous alkene is physisorbed next to the first π bonded alkene. In the transition state, one of the carbon atoms of the π bonded alkene is attacked by proton of BAS in the zeolite and the other carbon of the π bonded alkene is attacked by the π-electrons of the second physisorbed alkene simultaneously. Therefore, a new C-C bond is formed [26-28].

Stepwise reaction mechanism is evidenced by the formation of the alkoxide [7, 11, 29]. Iglesia et al. [7] found that after propene adsorption on the H-MFI and H-TON (10 kPa and 503 K), the hydrogen bonded propene was not observed in the IR. However, the new bands at 1365-1370 cm^{-1}, which are attributed to the structural vibration of the C-O in secondary and primary propoxide species at the T-12 location in MFI and T-3 location in TON, were observed. In addition, new bands at the region in between 1500−1450 cm^{-1}, attributed to the $–C_nH_{2n+1}$. Both phenomena can evidence that the propoxide intermediate was produced on H-MFI and H-TON after propene was adsorbed on the BAS. Giuseppe et al. [11] studied ethene adsorption on H-ZSM-5 through IR. At very short dosing time (below 10 s), hydrogen bonded ethene on BAS was observed on the 3620 cm^{-1} and the ethoxide became dominant between 10-30 s and the trimer and oligomers were formed after 30 s.

However, in some other studies the alkoxide was not directly observed [10]. Domen et al. [10] studied adsorption and reactions of 2-methyl-propene on Mordenite via IR. The dimerization product of 2, 4, 4-trimethyl-2-pentoxy species was observed by IR, however, the reaction intermediate of 2-methyl-2-propoxy was not observed. Trombetta et al. [30] studied the 1-butene or trans-2-butene oligomerization and no alkoxide was observed. The unobserved alkoxide intermediate can be explained by the concerted reaction mechanism.

Another significant issue is that deactivation of zeolites often occured during the hydrocarbon transformation [31-35]. Alkane and alkene cracking and dehydrogenation activities were quite stable in zeolites, while, faster deactivation of the active sites of the zeolites were observed during alkene oligomerization, hindering its application in the alkene dimerization [31, 36, 37].

Lin et al. [31] reported that the conversion of ethene dimerization on H-MFI zeolite decreased from 60 to 20 % after 60 h reaction and the deactivation was largely from the carbon deposition on the active site. The zeolite could be regenerated in the O_2 gas flow. Mlinar et al. [36] showed that the activity of propene dimerization on the H-MFI zeolite decreased to 85% of the initial activity even though only 10% propene conversion was used. In addition, EFAl has been reported to be adverse influence on the stability of the zeolites in the hydrocarbon conversion [37, 38]. Wang et al. [37] showed that deactivation of H-MFI zeolite increased concurrent with EFAl content in the zeolite in the hexane cracking. Sami et al. [38] mentioned that all the H-MFI and steamed H-MFI zeolites deactivated in the initial period of methanol conversion. The severe dealuminated zeolite deactivated more rapidly and severely than the parent H-MFI zeolite and even completely deactivated in the methanol conversion. The EFAl was considered to block access of the reactant to the active site of zeolite [4].

The promoted effect of EFAl on BAS in the catalytic cracking of alkanes have been largely studied. However, the influence of EFAl in the elementary steps of alkene adsorption and reaction on BAS as well as in the BAS stability is not understood. The knowledge about the energy barrier on these steps on I-SBAS and EFAl-SBAS is lacking. Therefore, in this study, two H-MFI-15 samples with different percentage of EFAl-SBAS and I-SBAS were used in the reaction of ethene dimerization. Infrared spectra and kinetic measurement will be explored to measure the nature and energy barrier of the states on the two sites.

4.2. Experimental

4.2.1. *IR spectroscopy of adsorbed ethene*

IR spectra with ethene as probe molecule on zeolite were carried at same ethene and N_2 flow rate as the kinetic measurement. The catalysts were pressed into self-supporting wafers and activated in N_2 flow (100 ml min^{-1}) at 723 K for 1 h prior to ethene adsorption. After the samples were cooled to 513 K, ethene was dosed onto the activated samples with the N_2 flow. All the spectra were collected at 513 K.

4.2.2. Catalyst test

Dimerization of ethene was performed in a quartz tube plug flow reactor with an inner diameter of 6 mm at atmospheric pressure. The samples were pressed and sieved into 210-315 μm particles before loaded into the reactor. The catalysts were activated in 100 ml min^{-1} synthetic air flow at 803 K for 3 h, followed by flushing with 100 ml min^{-1} N_2 flow for 4 h at target reaction temperature. Low reaction temperatures (between 493 and 523 K) and low ethene partial pressures (20-50 mbar) were employed to reduce β cracking of ethene. Ethene was fed by passing through N_2 in the total flow 100 ml min^{-1} and ethene partial pressure was achieved by changing the ratio of ethene and N_2 in the mixture. Low ethene conversion (below 1.3%) was maintained to prevent formation of larger alkenes, which usually deactivates the catalyst. The reactor effluents were identified by a gas chromatograph and a flame ionization detector for online analysis. Rate normalized to catalyst weight and turnover frequency (TOF) normalized to SBAS concentration of formation of products were applied to evaluate the catalyst performance.

4.3. Results and discussions

4.3.1. Adsorption properties of ethene on BAS of H-MFI

The percentage and concentration of EFAl-SBAS and I-SBAS sites on the H-MFI-15(0%) and H-MFI-15(43%) samples are quantified using the method reported in the chapter 2, which are summarized in Table 4.1.

Table 4.1. Physiochemical properties of H-MFI-15(0%) and H-MFI-15(43%).

Sample	Acid site concentration [μmol g^{-1}]					EFAl-SBAS/SBAS	V_{micro}[a]
	BAS[b]	SBAS[b]	LAS[b]	EFAl-SBAS	I-SBAS	[100%]	[cm^3 g^{-1}]
H-MFI-15(0%)[c]	511	442	27	0	442	0	0.16
H-MFI-15(43%)[d]	209	67	193	29	38	43	0.14

[a]The micropore volume of samples were measured by N_2 adsorption. [b]Determined by IR spectroscopy of adsorbed pyridine; after equilibration 423 K, desorption at 423 K for BAS and LAS and desorption at 723 K for SBAS. [c]H-MFI-15(0%) was attained by AHFS treatment from the parent H-MFI-15 zeolite. [d]H-MFI-15(43%) are attained by steaming of the parent H-MFI-15 zeolite.

Figure 4.2 illustrates IR spectra of OH stretching vibration region of 3850 to 1350 cm^{-1} for H-MFI-15(0%) and H-MFI-15(43%) via adsorption of ethene at the same conditions as the kinetic measurement (50 mbar and 513 K). On the H-MFI-15(0%), 11.4 and 16.2% of BAS (BAS-OH at 3610 cm^{-1}) was covered after 1 and 3 min ethene adsorption. The BAS cannot be fully (Figure

4.2 A). A broad perturbed BAS band (3610 cm^{-1}) at 3220 cm^{-1} was not observed, indicating that no hydrogen precursor of BAS (CH_2=CH_2···OHSiAl) was formed [11]. Several new peaks attributed to CH_3 and CH_2 groups were observed at 3044-2725 and 1566-1351 cm^{-1} Figure 4.3), suggesting that all the adsorbed ethene were protonated by the BAS to form chemisorbed alkoxide (-O-C_nH_{2n+1}) [7, 11]. The same phenomena were also detected on the H-MFI-15(43%) (Figure 4.2 B) and only 34 and 43% BAS was covered by ethene after 1 and 3 min adsorption. In addition, the peak of EFAl hydroxyl group (EFAl-OH) at 3660 cm^{-1} decreased and its perturbation band by the ethene at 3369 cm^{-1} were not observed [11], therefore, the decrease of the EFAl-OH was the result of chemisorption of ethene on the EFAl-OH groups. These results make us to assume that ethene chemisorbed on the EFAl-SBAS interacted with EFAl-OH and BAS-OH simultaneously on the H-MFI-15(43%) sample.

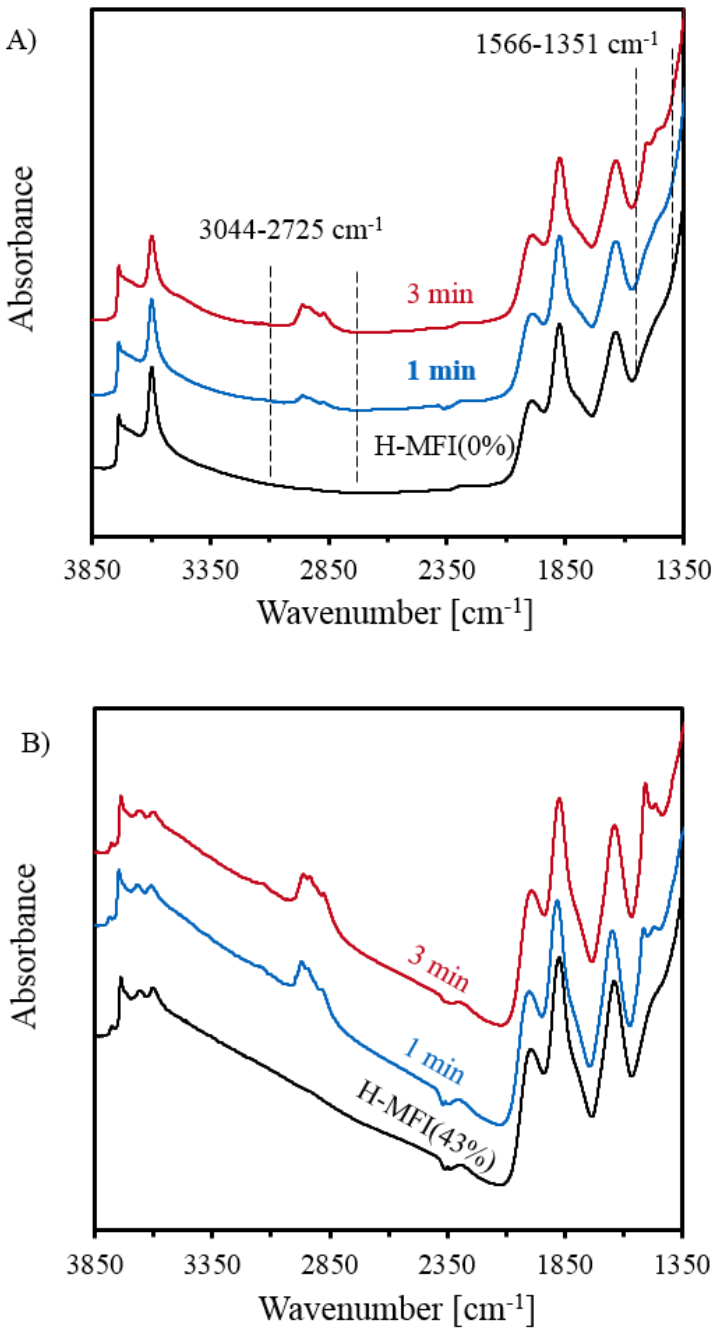

Figure 4.2. IR spectra of OH stretching vibration region of 3850 to 1350 cm^{-1} for H-MFI-15(0%) A) and H-MFI-15(43%) B) after ethene being adsorbed for 1 (blue line) and 3 (red line) min at 50 mbar and 513 K.

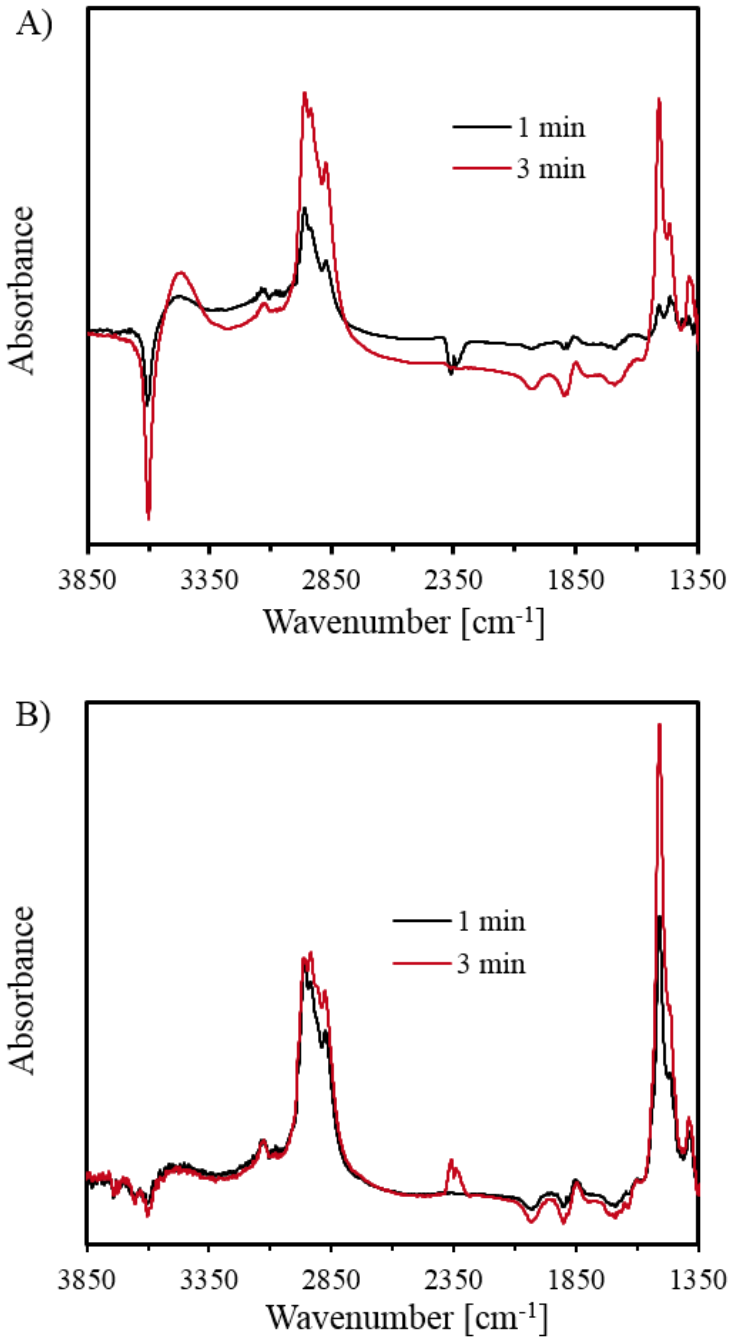

Figure 4.3. IR difference spectra of OH stretching vibration region of 3850 to 1350 cm^{-1} for H-MFI-15(0%) A) and H-MFI-15(43%) B) between the adsorption spectrum measured after ethene being adsorbed for 1 (black line) and 3 (red line) min at 50 mbar and the spectrum before adsorption of ethene at 513 K.

4.3.2. Catalytic performance of ethene dimerization on I-SBAS and EFAl-SBAS

Ethene dimerization reaction was used to evaluate the catalytic performance of H-MFI-15 samples with 0 and 43% EFAl-SBAS. The products with carbon numbers from 3 to 6 were detected even at low ethene conversion of 0.1%, indicating that the secondary reactions for ethene dimerization were unavoidable, taking place even at low ethene conversions. Larger alkene molecules were not observed at ethene conversions below 1.3%. As no heptene and octene were detected in the products, formation of pentene from the β scission of decene was impractical and it was only as the result of dimerization of ethene and propene. Pathways for ethene reaction at low conversion on a zeolite are proposed in scheme 4.1: primary reaction for dimerization of two ethene molecules (C_4H_8 pathway) and three secondary reactions for coordinative reaction of ethene and buthene (C_6H_{12} pathway), β scission of hexene (C_3H_6 pathway) and coordinative reaction of ethene and propene (C_5H_{10} pathway).

$$2C_2H_4 \rightarrow C_4H_8 \quad (1)$$

$$C_2H_4 + C_4H_8 \rightarrow C_6H_{12} \quad (2)$$

$$C_6H_{12} \rightarrow 2C_3H_6 \quad (3)$$

$$C_2H_4 + C_3H_6 \rightarrow C_5H_{10} \quad (4)$$

Scheme 4.1: Proposed reaction pathways for ethene dimerization on a zeolite.

Ethene reaction conversion increased initially and then kept constant on both H-MFI-15(0%) and H-MFI-15(43%) (Supplementary Figure 4.1). The conversion did not vary with prolonged time on stream and the data in this steady state was employed for the kinetic analysis. As ethene was converted in three pathways: C_4H_8 (1), C_6H_{12} (2) and C_5H_{10} (4) pathways, so ethene conversion rate is the sum of the three pathways as shown in Equation (1) and ethene conversion rate in different pathways can be attained by using Equation (2).

$$Rate_{\mathrm{t}} = Rate_{(1)} + Rate_{(2)} + Rate_{(4)} \quad (1)$$

$$Rate_{(\mathrm{x})} = \frac{n_{(\mathrm{x})}}{n_{\mathrm{total}}} \times Rate_{\mathrm{total}} \quad (2)$$

in which, the $Rate_t$ and $Rate_{(x)}$ are the ethene total conversion rate and conversion rate in different pathways, n_t and $n_{(x)}$ are ethene total converted molar concentration and converted molar concentration in different pathways.

The ture molar concentration of C_6H_{12} was calculated from the sum of observed molar concentration of C_6H_{12} and the molar concentration of C_6H_{12} converted to C_3H_6 via β scission

$$C_{C_6H_{12},ture} = C_{C_6H_{12},observed} + C_{C_6H_{12},converted} \quad (3)$$

The ture molar concentration of C_4H_8 was calculated from the sum of observed molar concentration of C_4H_8 and molar concentration of C_4H_8 converted to C_6H_{12} by secondary reaction with C_2H_4.

$$C_{C_4H_8,ture} = C_{C_4H_8,observed} + C_{C_4H_8,converted} \quad (4)$$

The molar concentration of C_2H_4 consumed in C_4H_8, C_6H_{12} and C_5H_{10} pathways was derived from the ture molar concentration of C_4H_8, C_6H_{12} and C_5H_{10}, respectively.

Table 4.2. Ethene conversion TOF in different pathways on H-MFI-15 (0%) and H-MFI-15(43%) at 40 mbar ethene partial pressure and 493 K.

Sample	Ethene conversion TOF in different pathways [10^{-3} s^{-1}]			
	Total	C_4H_8	C_5H_{10}	C_6H_{12}
H-MFI-15 (0%)	0.690 ± 0.006	0.524 ± 0.004	0.0532 ± 0.0012	0.113 ± 0.001
H-MFI-15(43%)	1.13 ± 0.04	0.878 ± 0.028	0.0476 ± 0.0065	0.204 ± 0.013

Table 4.2 shows TOF of ethene conversion in different pathways on H-MFI-15(0%) and H-MFI-15(43%) at 40 mbar ethene partial pressure and 493 K. The ethene conversion TOF on H-MFI-15(43%) is approximately two times higher than that on H-MFI-15(0%), indicating that the EFAl-SBAS has a higher activity of ethene conversion than I-SBAS. The increased trend is also observed in C_4H_8 and C_6H_{12} pathways, except C_5H_{10} pathway, in which the H-MFI-15(43%) has smaller rate.

The ethene conversion TOF of H-MFI-15(0%) with only I-SBAS, is considered as the TOF of I-SBAS ($(0.690 \pm 0.006) \times 10^{-3}\ s^{-1}$). The weight normalized ethene conversion rate on H-MFI-15(43%) is contributed by the rate on both I-SBAS and EFAl-SBAS. Using the readily obtained I-SBAS TOF and the concentrations of I-SBAS and EFAl-SBAS in H-MFI-15(43%), the TOF of EFAl-SBAS in H-MFI-15(43%) was obtained as $(1.71 \pm 0.01) \times 10^{-3}\ s^{-1}$ by Equation (5) at

493 K. The TOF of EFAl-SBAS is approximately three times higher than that of I-SBAS at 493 K(Table 4.3).

$$Rate_{\text{H-MFI-15(43\%)}} = TOF_{\text{I-SBAS}} \times C_{\text{I-SBAS}} + TOF_{\text{EFAl-SBAS}} \times C_{\text{EFAl-SBAS}} \quad (5)$$

Here, $Rate_{\text{H-MFI-15(43\%)}}$ is the weight normalized ethene conversion rate on H-MFI-15(43%), $C_{\text{EFAl-SBAS}}$ and $C_{\text{I-SBAS}}$ are the concentration of EFAl-SBAS and I-SBAS on H-MFI-15(43%), respectively.

Table 4.3. The TOF, apparent activation energy, entropy and Gibbs free energy of ethene conversion for I-SBAS and EFAl-SBAS (493 K and 40 mbar).

Active site	TOF, $[10^{-3}\ s^{-1}]$	$E_a^{\ddagger}{}_{,app}$ [kJ mol^{-1}]	$\Delta S^{\ddagger}{}_{,app}$ [J mol^{-1}K^{-1}]	$\Delta G^{\ddagger}{}_{,app}$ [kJ mol^{-1}]
I-SBAS	0.690 ± 0.006[a]	70 ± 1	-150 ± 1	142 ± 1
EFAl-SBAS	1.71± 0.10	48 ± 1	-187 ± 1	139 ± 1

[a]uncertainties are taken as 95% confidence interval.

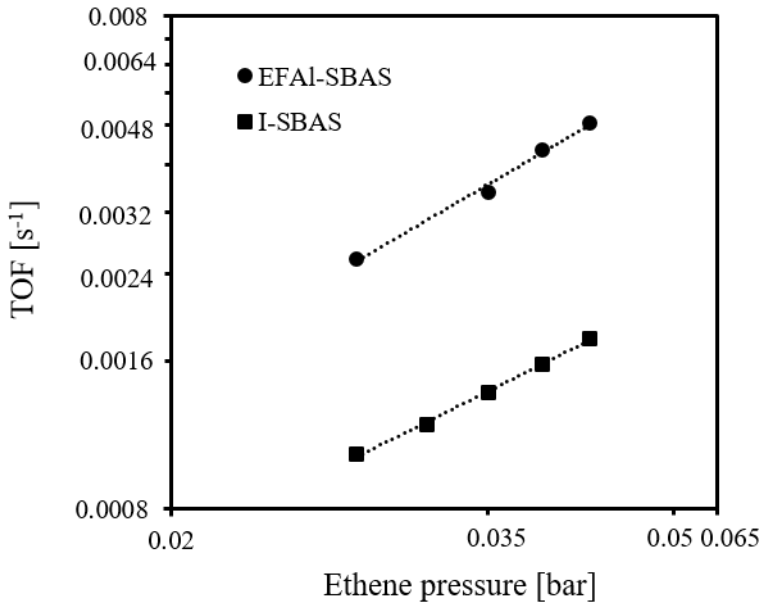

Figure 4.4. First-order reaction of ethene conversion on I-SBAS (■) and EFAl-SBAS (●) of H-MFI-15 (30-50 mbar).

Ethene conversion TOF has a good correlation with the ethene partial pressures (20-50 mbar, 513 K) on both H-MFI-15(0%) and H-MFI-15(43%) (Supplementary Figure 4.2). Similar correlation are also found on both I-SBAS and EFAl-SBAS (Figure 4.4), indicating that the first order reaction of ethene conversion occurs on both sites.

4.3.3. Elementary steps for ethene conversion on H-MFI.

Step 1. Ethene adsorption on BAS

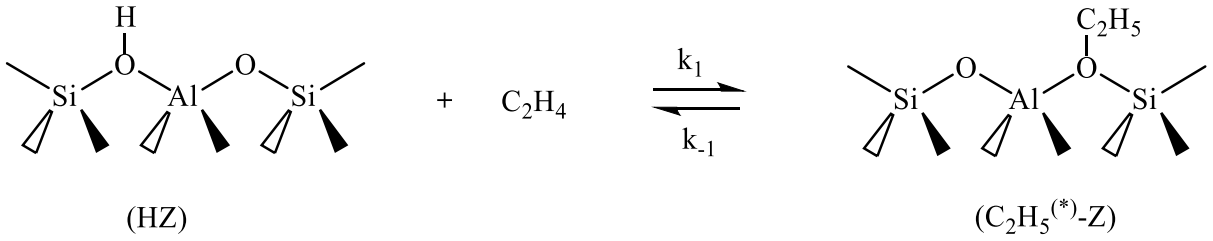

(HZ) ($C_2H_5^{(*)}$-Z)

Step 2. C-C bond formation

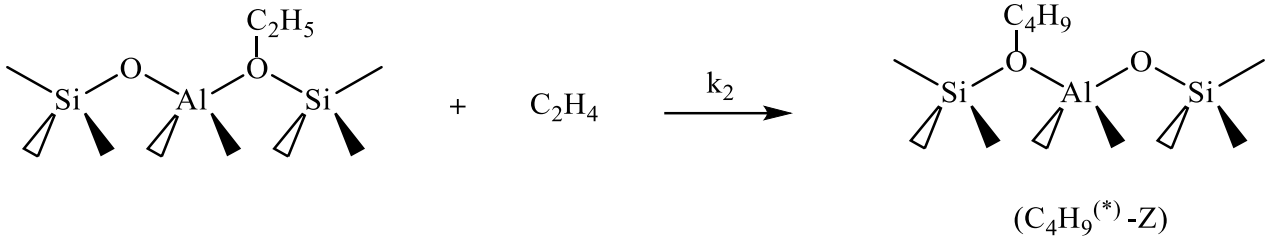

($C_4H_9^{(*)}$-Z)

Step 3. Buthene desorption from BAS

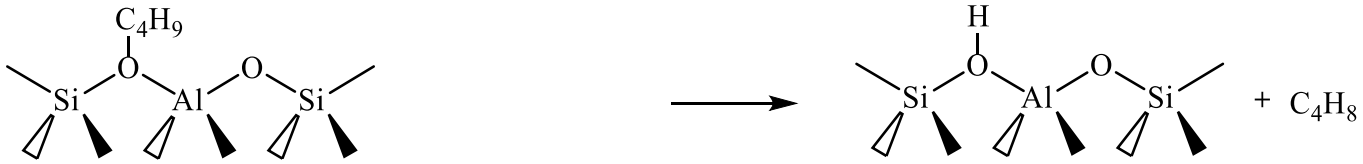

Scheme 4.1. Proposed elementary steps for ethene conversion on BAS of zeolite. In which, k_1, k_{-1} and k_2 are the adsorption, desorption and reaction rate constant of ethene on the BAS respectively.

Scheme 4.1 shows proposed elementary steps for ethene conversion on BAS of H-MFI. Proton of BAS approaches one of carbon in the ethene and second carbon of the ethene draws near to second oxygen in the zeolite [27]. Eventually, ethene is adsorbed on the BAS in the zeolite via quasi-equilibrium with formed chemisorbed ethoxide, which is covalently bonded between ethene and the BAS (Step 1, Scheme 4.1). A hydrogen boned ethene is not illustrated as fast and complete transformation of the ethene to alkoxide has been already evidenced by the IR of adsorption of ethene in the section 4.3.1

The overall reaction rate is the rate of formation of the butoxide (C_4H_9(*)-z) and it can be written as following. The detail deduction can be seen in the Supplementary Note 1.

$$Rate_{\text{meas}} = k_2 C_{HZ} P_{C_2H_4} \times \frac{k_1 P_{C_2H_4}}{[k_1 P_{C_2H_4} + k_{-1} + k_2 P_{C_2H_4}]} \quad (6)$$

As the BAS was not fully covered, the reaction of ethoxide and gaseous ethene cannot be the rate determining step (Supplementary Note 1). The formation of ethoxide by the adsorption of gaseous ethene on the BAS in the zeolite (Step 1, Scheme 4.1) is suggested as the rate determining step, so $k_1 P_{C_2H_4}$, $k_{-1} \ll k_2 P_{C_2H_4}$. Most of the BAS is unoccupied, so the C_{HZ} is close to unit. The reaction rate can be rewritten as:

$$Rate_{\text{meas}} = k_1 P_{C_2H_4} \quad (7)$$

Therefore, the step of the formation of ethoxide by adsorption of ethene on BAS is evidenced to be the rate determining step.

The TOF of ethene conversion on I-SBAS and EFAl-SBAS sites at different temperatures (Supplementary Table 4.1) were used to calculate apparent activation energy ($E_a^{\ddagger}_{,\text{app}}$) and apparent activation entropy ($\Delta S^{\ddagger}_{,\text{app}}$) (Table 4.3). As the step of the formation of ethoxide is the rate determining step, so the $E_a^{\ddagger}_{,\text{app}}$ and $\Delta S^{\ddagger}_{,\text{app}}$ represent the barrier from gaseous ethene to the transition state for formation of ethoxide. The $\Delta S^{\ddagger}_{,\text{app}}$ on I-SBAS (-187± 1 J $mol^{-1}K^{-1}$) is lower than that on EFAl-SBAS(-150 ± 1 J $mol^{-1}K^{-1}$), indicating that entropic destabilization of the transition state for the formation of ethoxide is existed on EFAl-SBAS and that the transition state for the formation of ethoxide on EFAl-SBAS is later than that on I-SBAS.

The $E_a^{\ddagger}{}_{,app}$ on I-SBAS is 70 kJ mol^{-1}, which is in the range reported by the theory estimation [26]. The $E_a^{\ddagger}{}_{,app}$ on EFAl-SBAS is lower than that on I-SBAS, suggesting that an enthalpic stabilization of the transition state for the formation of ethoxide on the EFAl-SBAS with respect to I-SBAS, which overcompensates the entropic destabilization of the transition state on EFAl-SBAS, leading to higher ethene dimerization rate on EFAl-SBAS than on I-SBAS.

4.3.4. Impact of EFAl on the deactivation of catalyst.

The BAS did not deactivate on both H-MFI-15(0%) and H-MFI-15(43%) at low ethene conversion (Supplementary Figure 4.1). However, deactivation of the two samples was observed at high conversion in Figure 4.5. To compare the deactivation of I-SBAS and EFAl-SBAS, similar initial conversion (approximately 8%) was assured by varying the catalyst weight on H-MFI-15(0%) and H-MFI-15(30%). Two sections were observed for the deactivation of the catalysts. The conversion decreased quickly at section 1 (4 h) on both H-MFI-15(0%) and H-MFI-15(30%), thereafter (at section 2), it decreased slowly with time on stream (TOS) and dropped to 2.5% after 49 h TOS on H-MFI-15(0%), while, the conversion keeps constant at 2.8% with the TOS on H-MFI-15(30%). It indicates that EFAl can prevent the deactivation of the H-MFI zeolites at high ethene conversion and longer reaction period.

Coke formed in the alkene conversion usually induces the blockage of the pore or the active sites of the catalyst [39, 40]. As the ethene conversion decrease linearly with TOS in the section 1 on H-MFI-15(0%) and H-MFI-15(30%), therefore, the blockage of the pore by coke on H-H-MFI-15(0%) and MFI-15(30%) is excluded.

At high conversions, the products above C_6 were detected on both H-MFI-15(0%) and H-MFI-15(30%). At the section 1 of deactivation, the selectivity of C_3H_6 increased and the selectivities of C_4H_8, C_5H_{10} and C_6H_{12} and the products above C_6 decreased with the TOS on H-MFI-15(0%) (Figure 4.6). Similar trends are also observed on H-MFI-15(30%), except the selectivity of the products above C_6 is constant. At section 2 of deactivation, the selectivity of C_3H_6 is higher on H-MFI-15(30%) with respect to on H-MFI-15(0%). However, the selectivities of C_4H_8, C_5H_{10} and C_6H_{12} on H-MFI-15(30%) are lower than that on H-MFI-15(0%). It reflects that formation of C_3H_6 through β scission of hexene was preferred on H-MFI-15(30%), as the diffusion of

larger oligomers (C_4-C_6) to outside of the pore was hindered on the spatial confined EFAl-SBAS, until smaller alkene was formed via β scission of these oligomers.

The selectivities of C_4H_8, C_5H_{10} and C_6H_{12} and the products above C_6 decreased continuously with the TOS on H-MFI-15(0%) at section 2 of deactivation and the changing trend of these higher oligomers is consistent with that of ethene conversion on H-MFI-15(0%), therefore it concludes that the deactivation of the catalysts are caused by the formation of these higher unsaturated oligomers, which is same with the deactivation of ethene on the NiO-$A1_2O_3$/SiO_2 catalysts [39, 41]. However, the selectivities of these products are stable on the H-MFI-15(30%) at the section 2 of deactivation and the reason may be that the EFAl can clean these oligomers adsorbed on the BAS and the BAS becomes free again.

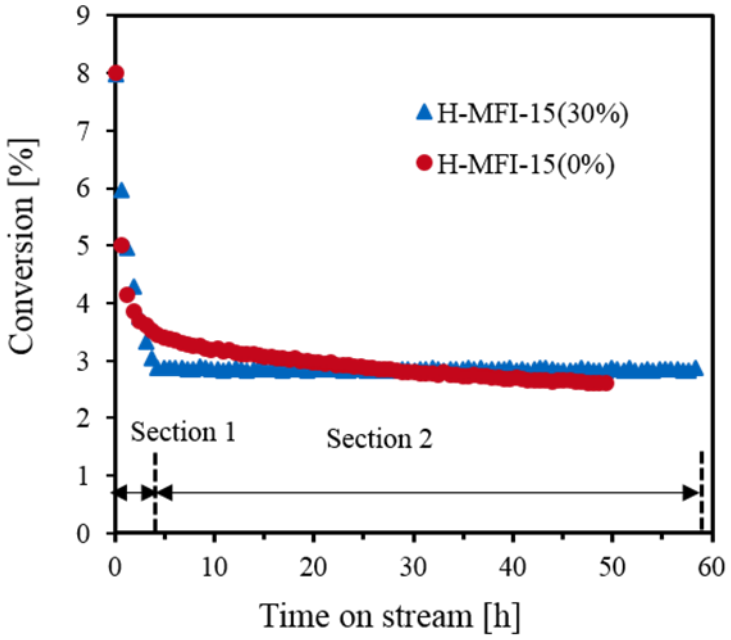

Figure 4.5. Evolution of ethene conversion with time on stream on 0.10 g H-MFI-15(0%) and 0.19 g H-MFI 15(30%) at 523 K and 50 mbar ethene partial pressure.

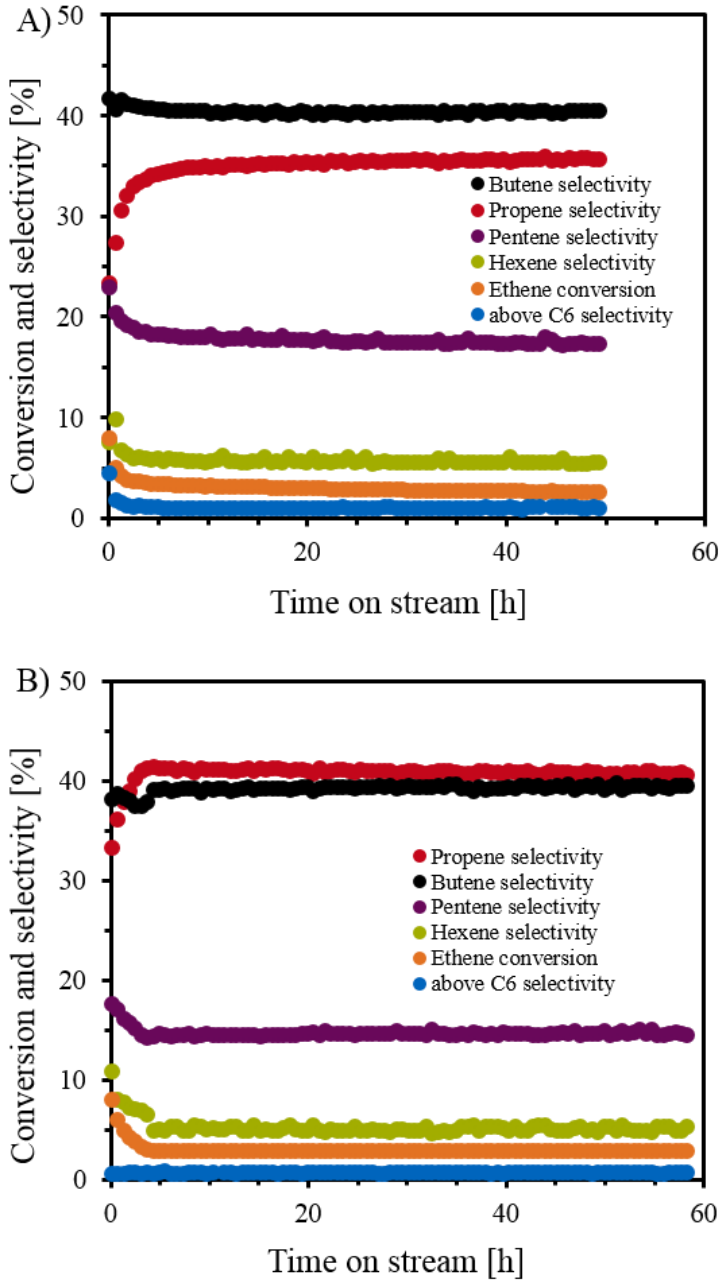

Figure 4.6. Evolution of product with time on stream on H-MFI-15(0%) A) and H-MFI-15(30%) B) at 523 K and 50 mbar ethene partial pressure.

4.4. Conclusions

Chemisorbed alkoxide (-O-C_nH_{2n+1}) was formed by protonation of ethene on BAS at low coverages at 50 mbar and 513 K by using in situ IR measurement of adsorption of ethene. The SBAS normalized ethene dimerization rate on EFAl-SBAS is 3 times higher than that on I-SBAS in H-MFI-15 samples. Ethene conversion follows first order reaction on both I-SBAS and EFAl-SBAS and the formation of ethoxide step is rate determining step.

The transition state for ethoxide formation on EFAl-SBAS is later with respect to I-SBAS. The higher rates for ethene dimerization on EFAl-SBAS are attributed to the stabilization of the

transition state for ethoxide formation via a lower activation energy. EFAl in the H-MFI can stabilize the catalyst and prevent the deactivaiton of the active site.

4.5 Contributions

The work in this chapter was under the supervision of Prof. Dr. Johannes A. Lercher, Dr. Yue Liu and Dr. Ricardo Bermejo-Deval. Yang Zhang contributed to the design of the experiments and operating setups and data analysis.

4.6. References

[1] C.T. O'Connor, M. Kojima, Alkene oligomerization, *Catalysis Today*, 6 (**1990**) 329-349.

[2] S.A. Tabak, F.J. Krambeck, W.E. Garwood, Conversion of propylene and butylene over ZSM-5 catalyst, *AIChE Journal*, 32 (**1986**) 1526-1531.

[3] R.J. Quann, L.A. Green, S.A. Tabak, F.J. Krambeck, Chemistry of olefin oligomerization over ZSM-5 catalyst, *Industrial & Engineering Chemistry Research*, 27 (**1988**) 565-570.

[4] M. Guisnet, P. Magnoux, Deactivation by coking of zeolite catalysts. Prevention of deactivation. Optimal conditions for regeneration, *Catalysis Today*, 36 (**1997**) 477-483.

[5] F. Geobaldo, G. Spoto, S. Bordiga, C. Lamberti, A. Zecchina, Propene oligomerization on H-mordenite: Hydrogen-bonding interaction, chain initiation, propagation and hydrogen transfer studied by temperature-programmed FTIR and UV-VIS spectroscopies, *Journal of the Chemical Society, Faraday Transactions*, 93 (**1997**) 1243-1249.

[6] M.L. Sarazen, E. Doskocil, E. Iglesia, Effects of Void Environment and Acid Strength on Alkene Oligomerization Selectivity, *ACS Catalysis*, 6 (**2016**) 7059-7070.

[7] M.L. Sarazen, E. Doskocil, E. Iglesia, Catalysis on solid acids: Mechanism and catalyst descriptors in oligomerization reactions of light alkenes, *Journal of Catalysis*, 344 (**2016**) 553-569.

[8] C.M. Nguyen, B.A. De Moor, M.-F. Reyniers, G.B. Marin, Physisorption and Chemisorption of Linear Alkenes in Zeolites: A Combined QM-Pot(MP2//B3LYP:GULP)–Statistical Thermodynamics Study, *The Journal of Physical Chemistry C*, 115 (**2011**) 23831-23847.

[9] S. Schallmoser, G.L. Haller, M. Sanchez-Sanchez, J.A. Lercher, Role of Spatial Constraints of Brønsted Acid Sites for Adsorption and Surface Reactions of Linear Pentenes, *Journal of the American Chemical Society*, 139 (**2017**) 8646-8652.

[10] H. Ishikawa, E. Yoda, J.N. Kondo, F. Wakabayashi, K. Domen, Stable Dimerized Alkoxy Species of 2-Methylpropene on Mordenite Zeolite Studied by FT-IR, *The Journal of Physical Chemistry B*, 103 (**1999**) 5681-5686.

[11] G. Spoto, S. Bordiga, G. Ricchiardi, D. Scarano, A. Zecchina, E. Borello, IR study of ethene and propene oligomerization on H-ZSM-5: hydrogen-bonded precursor formation, initiation and propagation mechanisms and structure of the entrapped oligomers, *Journal of the Chemical Society, Faraday Transactions*, 90 (**1994**) 2827-2835.

[12] F.R. Siperstein, A.L. Myers, Mixed-gas adsorption, AIChE Journal, 47 (2001) 1141-1159.

[13] E.G. Derouane, J.P. Gilson, J.B. Nagy, Adsorption and conversion of ethylene on H-ZSM-5 zeolite studied by 13C NMR spectroscopy, *Journal of Molecular Catalysis*, 10 (**1981**) 331-340.

[14] J.P. van den Berg, J.P. Wolthuizen, A.D.H. Clague, G.R. Hays, R. Huis, J.H.C. van Hooff, Low-temperature oligomerization of small olefins on zeolite H-ZSM-5. An investigation with high-resolution solid-state 13C-NMR, *Journal of Catalysis*, 80 (**1983**) 130-138.

[15] J.N. Kondo, S. Liqun, F. Wakabayashi, K. Domen, IR study of adsorption and reaction of 1-butene on H-ZSM-5, *Catalysis Letters*, 47 (**1997**) 129-133.

[16] E. Yoda, J.N. Kondo, K. Domen, Detailed Process of Adsorption of Alkanes and Alkenes on Zeolites, *The Journal of Physical Chemistry B*, 109 (**2005**) 1464-1472.

[17] B.A. De Moor, M.-F. Reyniers, O.C. Gobin, J.A. Lercher, G.B. Marin, Adsorption of C2−C8 n-Alkanes in Zeolites, *The Journal of Physical Chemistry C*, 115 (**2011**) 1204-1219.

[18] H. Li, S.A. Kadam, A. Vimont, R.F. Wormsbecher, A. Travert, Monomolecular Cracking Rates of Light Alkanes over Zeolites Determined by IR Operando Spectroscopy, *ACS Catalysis*, 6 (**2016**) 4536-4548.

[19] Y.-H. Yeh, R.J. Gorte, S. Rangarajan, M. Mavrikakis, Adsorption of Small Alkanes on ZSM-5 Zeolites: Influence of Brønsted Sites, *The Journal of Physical Chemistry C*, 120 (**2016**) 12132-12138.

[20] J.A. van Bokhoven, M. Tromp, D.C. Koningsberger, J.T. Miller, J.A.Z. Pieterse, J.A. Lercher, B.A. Williams, H.H. Kung, An Explanation for the Enhanced Activity for Light Alkane Conversion in Mildly Steam Dealuminated Mordenite: The Dominant Role of Adsorption, *Journal of Catalysis*, 202 (**2001**) 129-140.

[21] W.J.M. van Well, X. Cottin, J.W. de Haan, B. Smit, G. Nivarthy, J.A. Lercher, J.H.C. van Hooff, R.A. van Santen, Chain Length Effects of Linear Alkanes in Zeolite Ferrierite. 1. Sorption and 13C NMR Experiments, *The Journal of Physical Chemistry B*, 102 (**1998**) 3945-3951.

[22] J.A. van Bokhoven, B.A. Williams, W. Ji, D.C. Koningsberger, H.H. Kung, J.T. Miller, Observation of a compensation relation for monomolecular alkane cracking by zeolites: the dominant role of reactant sorption, *Journal of Catalysis*, 224 (**2004**) 50-59.

[23] V. Nieminen, M. Sierka, D.Y. Murzin, J. Sauer, Stabilities of C3–C5 alkoxide species inside H-FER zeolite: a hybrid QM/MM study, *Journal of Catalysis*, 231 (**2005**) 393-404.

[24] B. Boekfa, P. Pantu, M. Probst, J. Limtrakul, Adsorption and Tautomerization Reaction of Acetone on Acidic Zeolites: The Confinement Effect in Different Types of Zeolites, *The Journal of Physical Chemistry C*, 114 (**2010**) 15061-15067.

[25] D. Gleeson, Application of QM simulations and multivariate analysis in the study of alkene reactivity in the zeolite H-ZSM5, *Journal of Chemometrics*, 22 (**2008**) 372-377.

[26] Y. Chu, B. Han, A. Zheng, F. Deng, Influence of Acid Strength and Confinement Effect on the Ethylene Dimerization Reaction over Solid Acid Catalysts: A Theoretical Calculation Study, *The Journal of Physical Chemistry C*, 116 (**2012**) 12687-12695.

[27] S. Svelle, S. Kolboe, O. Swang, Theoretical Investigation of the Dimerization of Linear Alkenes Catalyzed by Acidic Zeolites, *The Journal of Physical Chemistry B*, 108 (**2004**) 2953-2962.

[28] S. Namuangruk, P. Pantu, J. Limtrakul, Investigation of Ethylene Dimerization over Faujasite Zeolite by the ONIOM Method, *ChemPhysChem*, 6 (**2005**) 1333-1339.

[29] M.L. Sarazen, E. Iglesia, Stability of bound species during alkene reactions on solid acids, *Proceedings of the National Academy of Sciences*, (**2017**).

[30] M. Trombetta, G. Busca, S. Rossini, V. Piccoli, U. Cornaro, FT-IR Studies on Light Olefin Skeletal Isomerization Catalysis: II. The Interaction of C4 Olefins and Alcohols with HZSM5 Zeolite, *Journal of Catalysis*, 168 (**1997**) 349-363.

[31] B. Lin, Q. Zhang, Y. Wang, Catalytic Conversion of Ethylene to Propylene and Butenes over H−ZSM-5, *Industrial & Engineering Chemistry Research*, 48 (**2009**) 10788-10795.

[32] P. Wang, J. Zhang, G. Wang, C. Li, C. Yang, Nature of active sites and deactivation mechanism for n-butane isomerization over alumina-promoted sulfated zirconia, *Journal of Catalysis*, 338 (**2016**) 124-134.

[33] J.W. Beeckman, G.F. Froment, Catalyst Deactivation by Active Site Coverage and Pore Blockage, *Industrial & Engineering Chemistry Fundamentals*, 18 (**1979**) 245-256.

[34] V.I. Zaikovskii, A.V. Vosmerikov, V.F. Anufrienko, L.L. Korobitsyna, E.G. Kodenev, G.V. Echevskii, N.T. Vasenin, S.P. Zhuravkov, E.V. Matus, Z.R. Ismagilov, V.N. Parmon, Properties and deactivation of the active sites of an MoZSM-5 catalyst for methane

dehydroaromatization: Electron microscopic and EPR studies, *Kinetics and Catalysis*, 47 (**2006**) 389-394.

[35] D. Rojo-Gama, M. Nielsen, D.S. Wragg, M. Dyballa, J. Holzinger, H. Falsig, L.F. Lundegaard, P. Beato, R.Y. Brogaard, K.P. Lillerud, U. Olsbye, S. Svelle, A Straightforward Descriptor for the Deactivation of Zeolite Catalyst H-ZSM-5, *ACS Catalysis*, 7 (**2017**) 8235-8246.

[36] A.N. Mlinar, P.M. Zimmerman, F.E. Celik, M. Head-Gordon, A.T. Bell, Effects of Brønsted-acid site proximity on the oligomerization of propene in H-MFI, *Journal of Catalysis*, 288 (**2012**) 65-73.

[37] Q.L. Wang, G. Giannetto, M. Guisnet, Dealumination of zeolites III. Effect of extra-framework aluminum species on the activity, selectivity, and stability of Y zeolites in n-heptane cracking, *Journal of Catalysis*, 130 (**1991**) 471-482.

[38] S.M.T. Almutairi, B. Mezari, E.A. Pidko, P.C.M.M. Magusin, E.J.M. Hensen, Influence of steaming on the acidity and the methanol conversion reaction of HZSM-5 zeolite, *Journal of Catalysis*, 307 (**2013**) 194-203.

[39] D. Kiessling, G.F. Froment, Sorption of ethene and propene on amorphous nickel oxide-alumina/silica catalysts under oligomerization conditions, *Applied Catalysis*, 71 (**1991**) 123-138.

[40] S. Müller, Y. Liu, M. Vishnuvarthan, X. Sun, A.C. van Veen, G.L. Haller, M. Sanchez-Sanchez, J.A. Lercher, Coke formation and deactivation pathways on H-ZSM-5 in the conversion of methanol to olefins, *Journal of Catalysis*, 325 (**2015**) 48-59.

[41] G. Wendt, E. Fritsch, D. Deininger, R. Schöllner, Studies on nickel oxide mixed catalysts, V. Propene dimerization on Nio−Al2O3/SiO2 catalysts, *Reaction Kinetics and Catalysis Letters*, 16 (**1981**) 137-141.

Supporting information

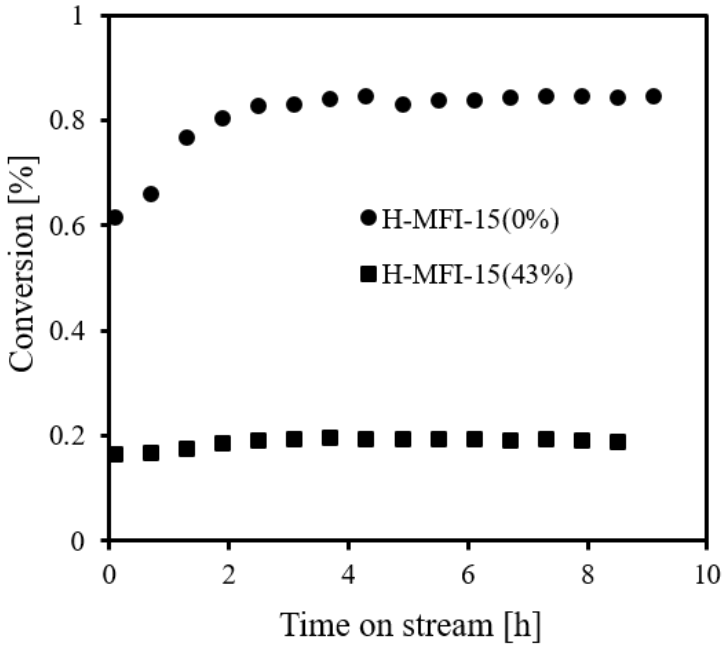

Supplementary Figure 4.1. Conversion of ethene dimerization on H-MFI-15(0%)(●) and H-MFI-15(43%) (■) (513 K and 40 mbar ethene partial pressure).

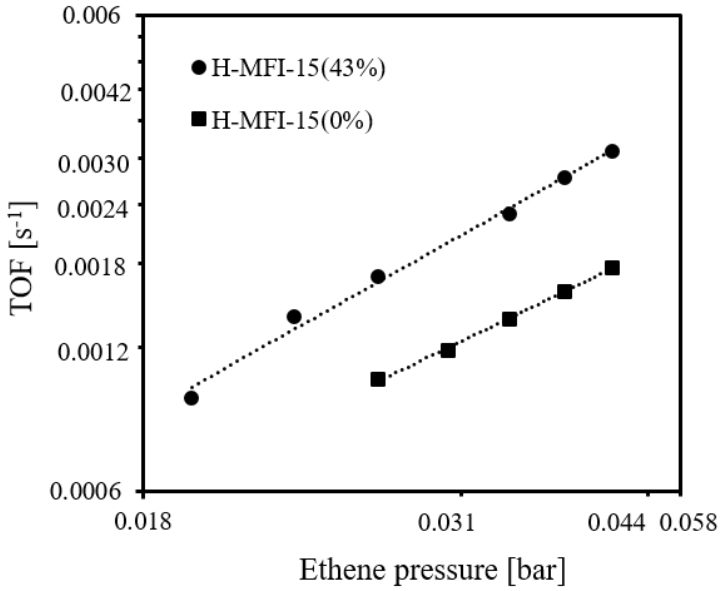

Supplementary Figure 4.2. First-order reaction of ethene conversion TOF on H-MFI-15(0%) (■) and H-MFI-15(43%) (●)(513 K and 20-50 mbar ethene partial pressure).

Supplementary Note 4.1. Reaction rate derivation for ethene conversion.

Proposed elementary steps for ethene conversion on BAS of H-MFI is shown in Scheme 4.1. The concentration of BAS occupied by ethoxide can be written as:

$$C_{C_2H_5{}^{(*)}-\mathrm{Z}} = C_{\mathrm{HZ}}\theta_{C_2H_5{}^{(*)}-\mathrm{Z}} \quad (1)$$

In which, $C_{C_2H_5(*)\text{-z}}$ is the concentration of BAS occupied by ethoxide, C_{HZ} is the concentration of BAS, $\theta_{C_2H_5(*)\text{-z}}$ is the fraction of BAS occupied by ethoxide.

Butoxide is formed through the reaction between C_2H_5OSiAl and another ethene molecule in the channel of zeolite (Step 2, Scheme 4.1). Steady state approximation is applied to the $C_2H_5(*)$-z:

$$\frac{dC_{C_2H_5{}^{(*)}-Z}}{dt} = r_1 - r_{-1} - r_2 = k_1 C_{HZ}^{'} P_{C_2H_4} - k_{-1} C_{C_2H_5{}^{(*)}-Z} - k_2 C_{C_2H_5{}^{(*)}-Z} P_{C_2H_4} = 0 \quad (2)$$

And $C_{HZ}^{'} = C_{HZ} \times (1 - \theta_{C_2H_5{}^{(*)}-Z})$ (3)

Where $P_{C_2H_4}$ is the pressure of gaseous ethene and $C_{\mathrm{HZ}}^{'}$ is the concentration of unoccupied BAS.

The coverage of BAS can be attained as following:

$$\theta_{C_2H_5{}^{(*)}-Z} = \frac{k_1 P_{C_2H_4}}{[k_1 P_{C_2H_4} + k_{-1} + k_2 P_{C_2H_4}]} \quad (4)$$

The overall reaction rate is the rate of formation of the butoxide ($C_4H_9(*)$-z) and it can be written as following.

$$Rate_{\mathrm{meas}} = r_2 = k_2 C_{C_2H_5{}^{(*)}-Z} P_{C_2H_4} = k_2 C_{HZ} P_{C_2H_4} \times \frac{k_1 P_{C_2H_4}}{[k_1 P_{C_2H_4} + k_{-1} + k_2 P_{C_2H_4}]} \quad (5)$$

If reaction of ethoxide and ethene is suggested as the rate determining step (Step 2, Scheme 4.1), so $k_2 P_{C_2H_4} \ll k_1 P_{C_2H_4}$, k_{-1}. Most of the BAS is unoccupied, so the C_{HZ} is close to unit. The reaction rate can be rewritten as:

$$Rate_{\mathrm{meas}} = k_2 P_{C_2H_4} \times \frac{k_1 P_{C_2H_4}}{[k_1 P_{C_2H_4} + k_{-1}]} = k_2 P_{C_2H_4} \times \frac{K P_{C_2H_4}}{[K P_{C_2H_4} + 1]} = k_2 P_{C_2H_4} \theta_{C_2H_5{}^{(*)}-Z} \quad (6)$$

Where $K = k_1 / k_{-1}$.

As the BAS is not fully covered, the reaction order is not 1. As the measured reaction order of ethene conversion on BAS of H-MFI is 1, so reaction of ethoxide and ethene cannot be the rate determining step.

If adsorption of gaseous ethene on the BAS in the zeolite (Step 1, Scheme 4.1) is suggested as the rate determining step, $k_1 P_{C_2H_4}$, $k_{-1} \ll k_2 P_{C_2H_4}$. Most of the BAS is unoccupied, so the C_{HZ} is close to unit. The reaction rate can be rewritten as:

$$Rate_{\text{meas}} = k_1 P_{C_2H_4} \quad (7)$$

Supplementary Table 4.1. TOF of ethene conversion on I-SBAS and EFAl-SBAS(493-523 K).

Temperature [K]	$TOF_{Iso\text{-}SBAS}$ [10^{-3} s^{-1}]	$TOF_{EFAl\text{-}SBAS}$ [10^{-3} s^{-1}]
493	0.690±0.006	1.71±0.10
503	1.047±0.007	2.20±0.09
513	1.437±0.017	2.51±0.04
523	1.825±0.005	3.43±0.17

[a]Uncertainties are taken as 95% confidence interval.

Chapter 5

5. Summary and conclusions

The aim of this thesis is to investigate the influence of the local environment of Brønsted acid sites by the extra-framework aluminum oxide in close proximity on the hydrocarbon transformation activities. In addition, the effect of Brønsted acid sites with the extra-framework aluminum oxide in close proximity on the alkene-derived intermediates or carbenium ion like transition state, which are often involved in the hydrocarbon transform reactions (such as C-C formation and cleavage), are also explored. Pentane cracking and ethene dimerization are chose as model reactions. This research may provide some clues to design new catalysts via modifying the structure of Brønsted acid sites and applied in the hydrocarbon transformation reactions.

The EFAl content in H-MFI zeolites can be tuned by steaming and AHFS treatment. Steaming temperatures, duration and partial pressures are changed to attain the zeolites with different percentage of EFAl-SBAS and mild steaming condition is beneficial to produce high percentage of this pair site. Some techniques, such as NMR, XANES, EXAFS and IR can evidence that the Al is removed from the framework and EFAl is formed. The EFAl at 3660 cm^{-1} is evidenced to be in close proximity to the SBAS by perturbation of EFAl-OH group by the adjacent BAS after adsorption of pyridine in the IR spectra. Based on this perturbation, the percentage and concentration of EFAl-SBAS in all the SBAS can be determined.

The EFAl-OH group is also perturbed by BAS upon adsorption of pentane in the IR spectra, which has lower acid strength than the BAS. Even so, the EFAl-SBAS has same binding strength with pentane with respect to isolated SBAS, which is evidenced by the similar adsorption equilibrium adsorption constant, adsorption enthalpy and entropy on the two sites. Pentane reaction TOF has a good linear correlation with the percentage of EFAl-SBAS in all the reaction pathways: cracking and dehydrogenation. Pentane overall cracking and dehydrogenation TOF on EFAl-SBAS are 50 and 80 times higher than that on I-SBAS respectively. The parent zeolite has the same EFAl-SBAS as the EFAl-SBAS created by

steaming treatment and this site can also be created by H-MFI zeolite with different Si/Al ratio. The other dealumination methods can also produce the EFAl-SBAS, such as static calcination.

A first order reaction is observed in all the reaction pathways, which follows the carbonium ion reaction mechanism. The intrinsic activation energy for the dehydrogenation pathway is same on both EFAl-SBAS and I-SBAS and the intrinsic activation entropy is higher on EFAl-SBAS with respect to the I-SBAS. In contract, the intrinsic activation energy for all the cracking pathways on EFAl-SBAS are higher than on the I-SBAS and intrinsic entropy for the cracking pathways are higher on EFAl-SBAS with respect to I-SBAS. It means that even though the enthalpy transition state is destabilized on the EFAl-SBAS with respect to I-SBAS in all the cracking pathways, the entropy transition state is more stabilized on the EFAl-SBAS, which compensates the enthalpic destabilization and improve the cracking TOF. All the reaction pathways are speculated to be later transition state. $C_1+C_4^=$ and $C_3+C_2^=$ cracking pathways pass through a C2-carbenium ion like transition state and $C_2+C_3^=$ cracking pathway passes a C3-carbenium ion like transition state. Comparing with the BAS structure in H-MFI zeolite, the location of EFAl-SBAS is less effect on the pentane conversion rate.

The EFAl-SBAS is also applied in the alkene dimerization, which has similar carbenium ion transition state as the cracking of alkane. The BAS can not be fully covered by adsorbed ethene in the IR using the same conditions as the kinetic measurement in the sample with and without EFAl-SBAS sites. The ethene molecule is protonated on the BAS to form chemisorbed alkoxide and hydrogen bonded alkene is not found in the IR. First order reaction are observed on both I-SBAS and EFAl-SBAS and the formation of ethoxide step from adsorption of gaseous ethene is suggested to be the rate determining step, combining with the not fully covered BAS after ethene adsorption. Comparing with the cracking, the EFAl-SBAS has reverse effect in the enthalpic and entropic transiton state: the EFAl-SBAS stabilize the enthalpy and destabilize the entropy of the transition state of formation of ethoxide with respect to the I-SBAS, which leads to the ethene dimerization TOF is 3 times higher on EFAl-SBAS than on I-SBAS. The transition state of formation of ethoxide is later on EFAl-SBAS with respect to on the I-SBAS for ethene dimerization.

In low ethene conversion, the ethene dimerization goes through an induction period and then steady state on both I-SBAS and EFAl-SBAS in H-MFI. However, this induction period

disappeared at the high ethene conversion, instead, the ethene dimerization activity decreased sharply after 4 h. Thereafter, the activity continued decreased on the sample with only I-SBAS and kept constant on the sample with EFAl-SBAS. Higher oligomers created in the ethene secondary reaction may block the BAS, which leads to the deactivation of the BAS and EFAl may clean the higher oligomers attached on the BAS and prevent the deactivation of the H-MFI zeolite.

List of publications

Journals

1. **Yang Zhang**, Ruixue Zhao, Maricruz Sanchez-Sanchez, Gary L. Haller, Jianzhi Hu, Ricardo Bermejo-Deval*, Yue Liu* and Johannes A. Lercher*, "Promotion of protolytic pentane conversion on H-MFI zeolite by proximity of extra-framework aluminum oxide and Brønsted acid sites" accepted by J. Catal. 2018.

2. **Yang Zhang**, Yue Liu*, Ricardo Bermejo-Deval*, and Johannes A. Lercher*, "Influence of extraframework aluminum and strong Brønsted sites interaction in H-MFI zeolite on ethene dimerization activity", in preparation, 2018.

3. **Yang Zhang**, Gang Li*, Hong Lu, Qiang Lv and Zhiguo Sun, Synthesis, Characterization and Photocatalytic Properties of MIL-53(Fe)-Graphene Oxide Composites, *RSC Adv.*, **2014**, 4, 7594-7600.

4. Dong-Chao Wang, Hong-Ying Niu, Gui-Rong Qu*, Lei Liang, Xue-Jia Wei, **Yang Zhang**, Hai-Ming Guo, Nickel-Catalyzed Negishi Cross-Couplings of 6-Chloropurines with Organozinc Halides at Room Temperature, *Org. Biomol. Chem.*, **2011**, 9, 7663-7666.

5. 8. Hai-Ming Guo, Wei-Hao Rao, Hong-Ying Niu, Li-Li Jiang, Lei Liang, **Yang Zhang**, Gui-Rong Qu*, Chelation-Assisted Palladium-Catalyzed High Regioselective Heck Diarylation Reaction of 9-Allyl-9H-Purine: Synthesis of 9-(3,3-Diaryl-allyl)-9H-Purines, *RSC Adv.*, **2011**, 1, 961-963.

6. Jian-Ping Li*, Li-Ping Zhang, Zai-kun Xue, **Yang Zhang**, Synthesis of Symmetrical Dithiocarbohydrazide by Microwave Irradiation under Solvent-free Condition, *Chinese Journal of Synthetic Chemistry*, **2011**, 19, 264-266.

Oral presentation

Yang Zhang, Ruixue Zhao, Yue Liu, Ricardo Bermejo-Deval, Maricruz Sanchez-Sanchez and Johannes A. Lercher, Influence of Lewis acid site and Brønsted acid site interaction of Zeolite on alkane cracking activity, 8th International Symposium on Acid-Base Catalysis, May 7-10 th, 2017, Rio de Janeiro, Brazil.

Poster

Yang Zhang, Ruixue Zhao, Yue Liu, Maricruz Sanchez-Sanchez, Ricardo Bermejo-Deval and Johannes A. Lercher, Extra-framework aluminum in proximity to Brønsted acid sites in H-ZSM-5 increases the rates in pentane cracking and dehydrogenation, poster, 13th European Congress on Catalysis, August 27-31th, 2017, Florence, Italy.